Fall 2013

Synthesis and characterization of perm-selective SERS-active silica-coated gold nanospheres for the direct detection of small molecules

Marie Carmelle Serviane Pierre-Bolivar
University of Iowa

SYNTHESIS AND CHARACTERIZATION OF PERM-SELECTIVE SERS-ACTIVE SILICA-COATED GOLD NANOSPHERES FOR THE DIRECT DETECTION OF SMALL MOLECULES

by

Marie Carmelle Serviane Pierre-Bolivar

A thesis submitted in partial fulfillment
of the requirements for the Doctor of
Philosophy degree in Chemistry
in the Graduate College of
The University of Iowa

December 2013

Thesis Supervisor: Associate Professor Amanda J. Haes

Graduate College
The University of Iowa
Iowa City, Iowa

CERTIFICATE OF APPROVAL

_____

PH. D. THESIS

_____

This is to certify that the Ph.D. thesis of

Marie Carmelle Serviane Pierre-Bolivar

has been approved by the Examining Committee
for the thesis requirement for the Doctor of Philosophy
degree in Chemistry at the December 2013 graduation.

Thesis Committee: _____
Amanda J. Haes, Thesis Supervisor

_____
Sarah C. Larsen

_____
Julie L. P. Jessop

_____
Christopher M. Cheatum

_____
Vicki H. Grassian

To my loving husband Gray G. Bolivar
And
My Family

ACKNOWLEDGEMENTS

Foremost, I would like to express my gratitude to my advisor Dr. Amanda J. Haes for accepting me into her research group and for introducing me to the world of nanotechnology and nanoscience, a field that I had never even heard of until I came to the University of Iowa. I am thankful to Dr. Haes for providing me with the amazing opportunity to complete my Ph.D. dissertation work on investigating the surface chemistry on gold nanospheres for SERS assays. My thesis work would not have been possible without her support and guidance. Because of her patience, enthusiasm, and immense knowledge in this specialized research field, I have always felt ready to go the extra mile to avail myself of her expertise.

I would also like to thank all of Dr. Haes' group members, both former and present. Special gratitude goes to Dr. Maryuri Roca for helping me understand how graduate school research works during my first year in Dr. Haes' group. I am grateful to Anna Volkert and Binaya Shrestha for their support. I would like them to remember that we chose to pursue a Doctoral degree because we know where we want to be, and although it is a difficult path, we will succeed if we stay focused and motivated.

I would like to let all the faculty members on my academic committee know how grateful I am to them for being a part of my academic career. Especial thanks go to Dr. Sarah Larsen, who has been with me from the beginning of my research.

Many thanks go to all of my wonderful friends that I have made at the University of Iowa and in Iowa. Special thanks to Imali Mudunkotuwa, Tatiana Mishanina, and Anna Volkert for being there to listen, in good times and in bad.

Next, I would like to thank my parents. Thank you to my Dad, Luckner Pierre, and my Mom Roselaure Elcide-Ferrier for bringing me into this world. Thank you to my Mom Yoldie Pierre for teaching me all I know, which makes me who I am. Thanks to my siblings Barchmard, Arcline, Roselie, Ardley, Djenane, Cleeve, Lise, Julio, Mathanaelle, Gamael, and Rose-Andre. I am especially grateful to Roselie and Djene, my favorite sisters, who have always been on the other end of the phone when I call.

Last, but not least, I would like to present my sincere gratitude to my wonderful and loving husband, Gray G. Bolivar, without whom this work would not be possible and who has always been waiting for me at home after a bad day in the lab.

Thanks to all who has been part of my long journey.

MCSP-B
Iowa City, IA
December 2013

ABSTRACT

Noble metal nanomaterials have numerous uses in plasmonic and surface enhanced Raman scattering (SERS) detection applications; however, upon the addition of analytes, nanomaterials often undergo uncontrolled aggregation which leads to inconsistent signal intensities. To overcome this limitation, the effect of gold nanosphere concentration, column purification, and surface chemistry functionalization using internally etched silica stabilization methods was investigated on SERS assays for small molecule detection. Nanostructure composition, size, shape, stability, surface chemistry, optical properties, and SERS-activity were monitored using localized surface plasmon resonance (LSPR or extinction) spectroscopy, transmission electron microscopy (TEM), and Raman spectroscopy. First, the behavior of citrate-stabilized gold nanospheres was monitored as a function of molecular surface coverage. Both extinction and SERS spectral intensities increased linearly below monolayer functionalization. Above this value, however, uncontrolled nanoparticle aggregation occurred and large but irreproducible SERS signal intensities were monitored. Next, gold nanoparticles were encapsulated with varying silica shell thicknesses and purified using traditional centrifugation steps and/or column chromatography. Relative to the traditionally purified (i.e. centrifuged) samples, the SERS responses from small molecules using the column purified nanoparticle samples followed a well-known SERS distance-dependence model. Thus, surface chemistry cannot form more than a 2 nm thick layer on gold nanospheres if SERS applications were targeted. To overcome these challenges, gold nanospheres encapsulated with a thick silica shell were made SERS-active by etching the internal silica layer near the metal surface. During the synthesis of these internally etched silica-coated gold nanospheres,

the LSPR wavelength shift, a parameter related to the effective local refractive index near the gold core, was monitored instead of etching time, in order to produce nanostructures with more uniform internal silica etching from sample to sample. The SERS-activity of a target molecule using these nanostructures was measured as a function of LSPR wavelength shift. SERS signal intensity increased, which suggested that more analyte molecules were able to bind to the gold surface because of the larger pore size in the silica layer near the metal core. Further exploration of these findings should increase the integration of solution-phase nanoparticles in more predictable functions in future applications, resulting in more quantitative and reproducible molecular detection in complex sample matrices, including biological and environmental samples.

TABLE OF CONTENTS

APPENDIX

LIST OF TABLES

LIST OF FIGURES

LIST OF ABBREVIATIONS

Au: Gold

Ag: Silver

Pt: platinum

Cu: Copper

Na: Sodium

Li: Lithium

$Au@SiO_2$: Silica-coated gold

IE $Au@SiO_2$: Internally etched silica-coated gold

APTMS: (3-aminopropyl)trimethoxysilane

APTES: (3-aminopropyl)triethoxysilane

TEOS: Tetraethyl orthosilicate

NH_4OH: Ammonium hydroxide

HCl: Hydrochloric acid

HNO_3: Nitric acid

NaCl: Sodium chloride

$HAuCl_4 \cdot 3H_2O$: Gold (III) chloride trihydrate

2-NT: 2-Naphthalenethiol

4-ABT: 4-Aminobenzenethiol

CBTP: Citrate bis-tris propane

nM: Nanomolar

mL: Milliliter

cm: Centimeter

cm^{-1}: Wavenumber or inverse centimeter

nm: Nanometer

sr: Steradians

pM: Picomolar

μM: micromolar

M: Molar

eV: Electron volt

mW: Milliwatt

msec: Millisecond

min: Minute

μS: Microsemen

Ω: Ohms

s: Second

^{o}F: Degree Fahrenheit

AU: Arbitrary unit

ADU: Arbitrary density unit

UV-vis: Ultraviolet-visible

LSPR: Localized surface plasmon resonance

SERS: Surface-enhanced Raman scattering

TEM: Transmission electron microscopy

A: Area

T: Silica shell thickness

C: Concentrations

ε: Extinction coefficient

SA: Surface area

n: Refractive index

m: Refractive index sensitivity

d: Mean diameter or adsorbed thickness

l_d: Characteristic electromagnetic field decay length

EM: Electromagnetic

CHEM: Chemical

t_{int}: Integration time

λ: Wavelength

λ_{ex}: Excitation wavelength

ν_{vib}: Vibrational frequency

λ_{max} & $\Delta\lambda_{max}$: Extinction maximum wavelength and Extinction maximum wavelength shift

2D & 3D: Two and three-dimensions

vs.: Versus

CHAPTER I

SYNTHESIS, CHARACTERIZATION, AND DIRECT MOLECULAR DETECTION USING DIELECTRIC STABILIZED SERS SUBSTRATES

1.1 Introduction

Nanostructures are materials whose structural elements have one dimension in the 1 to 100 nm range[5-10] and have unique optical properties arising from their nanoscale dimensions.[7, 9] Over the years, researchers from various fields have been focused on improving the synthesis and fabrication methods of these nanostructures[11-16] because nanostructures' unique size dependent properties are not observed in bulk materials.[17-24] These properties depend on nanostructure composition, shape, size, local dielectric environment, and surface chemistry.[25-28] Control over these parameters, especially nanomaterial surface chemistry, is critical for successful and reproducible molecular detection applications because modifying the surface of the nanomaterials will improve their catalytic[29] and optical[30] properties, as well as their structural stability[31] in various bulk environments.[32]

An important class of nanomaterials exhibits size-dependent plasmonic properties. Plasmonic nanomaterials are composed of noble metals (i.e., gold, silver, copper, etc.),[3, 33, 34] exhibit optical properties which arise from their localized surface plasmon resonance (LSPR), [35, 36] and can be used in a wide range of applications including surface-enhanced Raman scattering (SERS).[37-39] These noble metal nanostructures exhibit unique size-dependent optical properties that allow their use as functional materials in applications including plasmonic devices,[40-44]

optical filters,[40, 45] chemical and biological sensors,[46-55] and surface-enhanced spectroscopy.[56-64]

1.2 Localized Surface Plasmon Resonance (LSPR) and SERS

LSPR spectroscopy is a phenomenon that occurs when electromagnetic radiation interacts with a noble metal nanoparticle that is smaller than the wavelength of light.[25, 27, 28, 65, 66] The light is selectively absorbed and/or scattered by the metal nanostructure, which causes the free conduction electrons on the surface of the nanoparticle to oscillate collectively.[25, 37, 65-68] Two implications of LSPR are (1) a strong extinction band and (2) surface-enhanced spectroscopy, including SERS.

When radiation passes through a medium, the molecules present in the sample interact with the incident beam, and scattering occurs. Most of the scattered photons have the same frequency and the same wavelength as the incident photons, which is known as elastic or Rayleigh scattering.[69] In 1928, Raman and Krishnan reported that some scattered photon energy is different from that of the incident light.[69-72] This scattered photon energy is known as inelastic or Raman scattering.[73] The Raman scattering photons can either gain or lose energy.[74] Stokes scattering results from an excitation from the ground state to a virtual energy state, followed by a relaxation into an excited vibrational state. However, if the analyte species present in the sample become stimulated at an excited vibrational state and then relax to the ground state, then the scattered photons will have a greater frequency and appear at a higher energy. This type of scattering is known as anti-Stokes.[73] Figure 1.1 illustrates an energy-level diagram for both Rayleigh and Raman scattering, where the

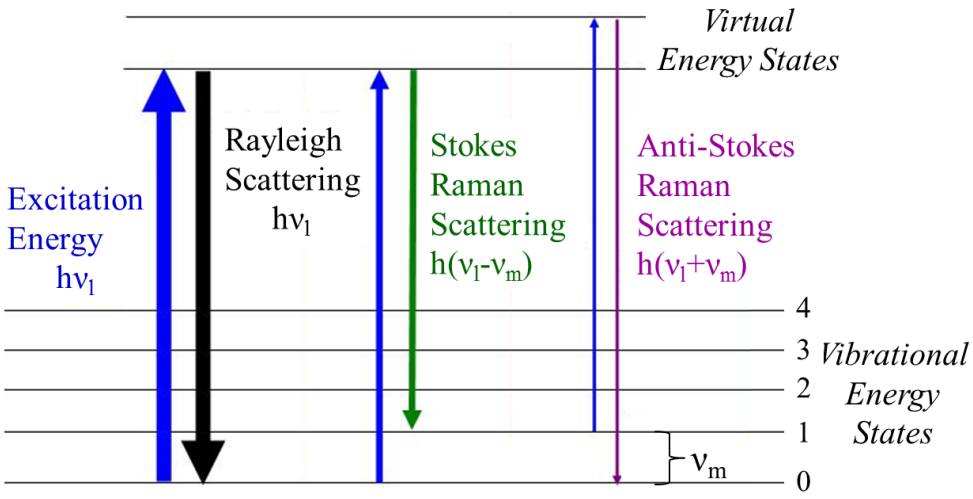

Figure 1.1 Energy-level diagram for Rayleigh (elastic) and Raman (inelastic) scattering at the frequency of the light source (ν_l). Rayleigh scattering has the same energy as the excitation energy. Raman scattering can either manifest as Stokes or anti-Stokes, which appear at a lower and higher frequency in relation to Rayleigh scattering, respectively. The molecular vibration of the analyzed sample is of frequency ν_m.

thicker the line, the stronger signal of the transition.[75-80]

Raman scattering has numerous advantages in comparison to other analytical techniques, including fluorescence spectroscopy.[81-88] For instance, the width of the Raman bands are usually 10-100 times narrower than most fluorescence bands.[83] Thus, with Raman spectroscopy, it is possible to identify molecules with very small structural variations.[84] Significantly, Raman spectroscopy is a label-free, nondestructive method with simple sample preparation. Data collection is rapid, and chemical reactions can be monitored in real time. Nevertheless, normal Raman scattering provides very weak signals of high analyte concentrations (M), a result of very small Raman cross-sections (~$l0^{-29}$ - $l0^{-31}$ cm^2 sr^{-1}).[84, 89, 90]

The weak signal limitation from Raman scattering can be overcome using SERS.[91-93] SERS is a surface-sensitive[11, 94-96] technique that was discovered over 35 years ago[97-102] and is suitable for studying small quantities of analytes at low concentrations (pM to single molecules).[61, 103-107] This method enhances the normal Raman signal of molecules in solution by adsorbing the molecules on or near a rough metal surface[108-112] or metal nanoparticles.[113, 114] The resulting enhancement can be up to 9 orders of magnitude (Figure 1.2)[61, 94, 101, 115-118] and is generally attributed to both chemical and electromagnetic effects.[34, 66, 100, 115, 119-127] The chemical enhancement mechanism is a short-range effect[3, 128-130] that arises from the direct interaction between an adsorbed molecule and the metal surface, which contributes up to 2 orders of magnitude to the SERS signal.[94, 128, 129, 131, 132] Electromagnetic enhancement, on the other hand, is a long-range effect that provides a contribution of up to 8 orders of magnitude.[105, 126, 128, 130,

133] This enhancement is attributed to the LSPR of the noble metal substrate.[18, 131, 134-142] Figure 1.2 shows a comparison of a normal Raman scattering spectrum of 3 M pyridine in solution and a SERS spectrum of a monolayer of pyridine adsorbed on a silver nanoparticle array. The target molecule was identified from each method; however, the SERS response intensity of the analyte was 7 orders of magnitude larger than that of the normal Raman signal.

1.3 SERS Substrates

Numerous metal substrates have been used to obtain SERS spectra of target molecules. These enhancing metals include Ag, Au, Pt, Cu, Na, Li, and other transition metals.[97, 143-148] The most common metal substrates used for SERS detection are solution-phase noble Ag and/or Au colloids[149, 150] because the synthesis methods for these nanoparticles are straightforward and provide large, qualitative Raman enhancements.[151] Thanks to the increase in the advances of nanoscience fabrication and synthesis, both Ag and Au nanoparticles can now be synthesized with well-defined structures in diameters ranging from micro to molecular scales.[152-154]

However, the utility of these noble metal nanoparticles as SERS substrates is limited because of poor control over their electromagnetic and/or physical stability.[155, 156] This lack of control is especially true for silver nanoparticles because citrate-stabilized silver nanoparticles: (1) release Ag^+ by oxidative dissolution, which can be re-adsorbed to the particle surface;[157, 158] and (2) often aggregate to minimize their large surface area or energy (i.e., silver nanoparticles ranging from 1-10 nm diameter).[159] These two phenomena will vary the surface

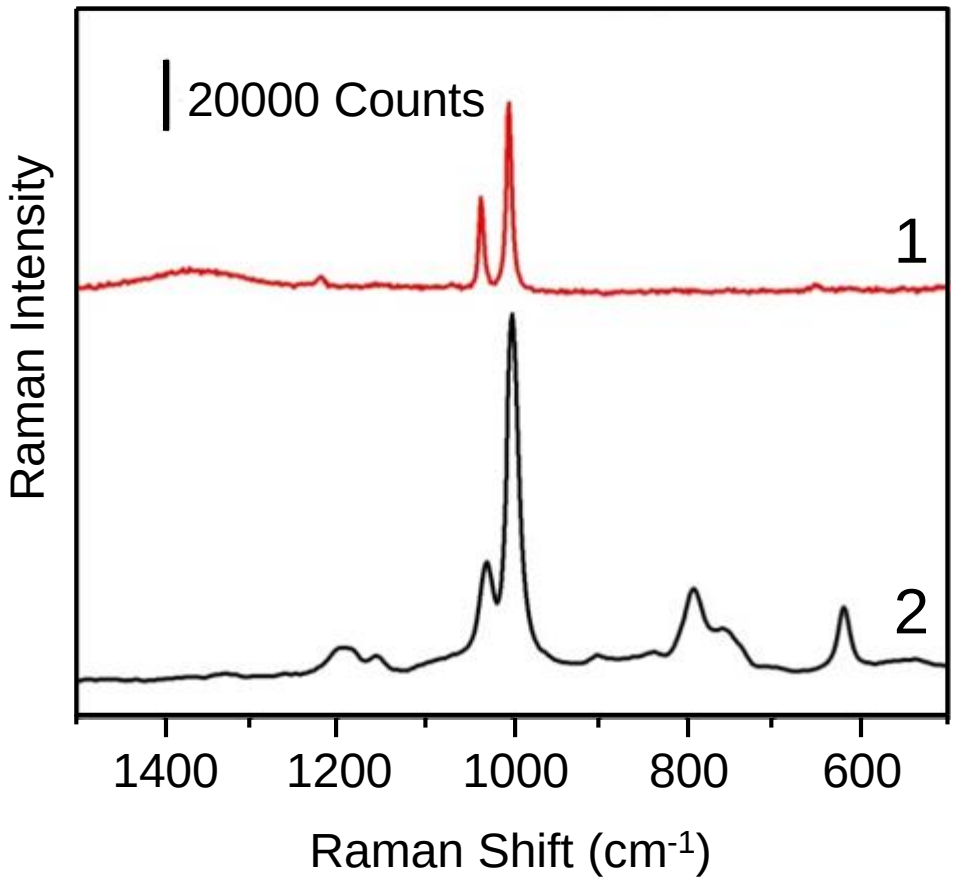

Figure 1.2 Comparison of (1) a normal Raman spectrum of 3 M pyridine in solution and (2) a SERS spectrum of a monolayer pyridine on a silver nanoparticle array (Haes data).

chemistry of these nanoparticles, leading to inconsistent LSPR and SERS measurements. Moreover, modifying the surface of silver nanoparticles can be a challenge because of the above phenomena, and this synthesis is often conducted in the dark. Gold nanoparticles, on the other hand, can remain stable for months with citrate capping.[160] However, upon the addition of target molecules, citrate-stabilized gold nanoparticles can undergo uncontrolled aggregation, which limits the reproducible quantitative analysis of target molecules.[156, 161, 162]

In order to obtain quantifiable and reproducible SERS signals, several approaches have been used. The first approach is to modify the gold surface with ligands[163] to prevent aggregation. During ligand displacement, however, aggregation can still occur and cause changes in the LSPR and SERS signals.[163] The second approach is to encapsulate gold cores in robust shells composed of polymers,[164] dendrimers,[165] or silica.[161, 166, 167] For instance, sol-gel silica is a well-known method to form core@shell structures.[168-170] The silica shell offers several advantages, including electromagnetic stability in various solvents, optical transparency, and biocompatibility.[167, 171-173] It can be synthesized as a thin, microporous silica shell;[174] a thick, microporous silica shell;[161] or as a mesoporous silica shell on metal nanoparticle surfaces.[4] Although small molecules and ions can diffuse through these silica,[175] their utility for SERS study is limited, because certain Raman-active molecules, such 2-naphthalenethiol and 4-aminobenzenethiol, are unable to diffuse through the silica shells toward the metal core, enabling detection.[176-178] Figure 1.3A shows TEM images for these three types of silica shells. As shown in Figure 1.3B1-3, no SERS signal was observed in

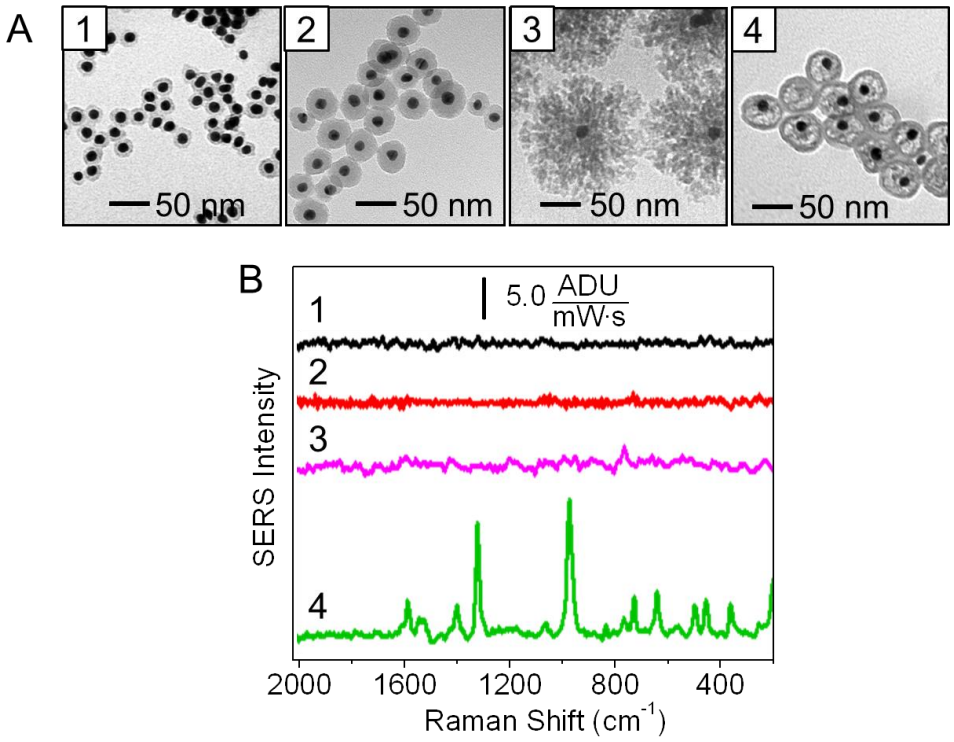

Figure 1.3 (A) TEM micrograph and (B) SERS spectra of 2-naphthalenethiol, using synthesized gold nanospheres with modified surfaces: (1) thin, microporous silica; (2) thick, microporous silica; (3) mesoporous silica; and (4) internally etched silica shells.[4]

their presence.[4] However, if the internal silica matrix is etched away by controlling the silica precursors used during silica condensation, SERS-activity is observed (see Figure 1.3B4).[161]

1.4 Thesis Outline

In this thesis project, the impact of nanoparticle concentration and surface chemistry on the use of gold nanospheres in SERS studies was investigated. The SERS responses of these target molecules are explored as a function of analyte and nanoparticle concentrations, silica shell thicknesses, and extinction wavelength shift. In Chapter 2, molecular surface coverage of the target molecule 2-naphthalenethiol and a known gold nanoparticle concentration are shown to be critical in generating correlated extinction and SERS signals using solution-phase, citrate-stabilized gold nanostructures. In Chapter 3, variation in the direct SERS detection of the target molecule, 2-naphthalenethiol, is eliminated by applying a quality control step (column chromatography) to silica-coated gold nanospheres prior to their use as SERS substrates. In Chapter 4, using the shift in the extinction maximum wavelength during internal silica dissolution for the fabrication of internally etched, silica-coated gold nanoparticles, instead of using etching times, is shown to lead to more uniform internal etching from sample to sample. This more uniform internal etching, in turn, allows for more consistent SERS measurement of target molecules. Finally, in Chapter 5, conclusions and future directions of solution-phase nanomaterial synthesis for the direct SERS detection of target molecules are summarized. In the future, these materials could be integrated into multi-analyte detection for biological and environmental applications. In Appendix A, extinction and SERS spectral responses

are correlated to transmission electron micrographs of internally etched, silica-coated gold (IE $Au@SiO_2$) nanospheres, as a function of etching time. Based on these results, the synthesis of $Au@SiO_2$ nanospheres was troubleshooting to reduce the percentage of observed free silica particles. Preliminary SERS results using internally etched $Au@SiO_2$ nanospheres from various environments, which relate to ionic strength, pH, and polarity are presented in Appendix B.

CHAPTER II

CORRELATING MOLECULAR SURFACE COVERAGE AND SOLUTION-PHASE NANOPARTICLE CONCENTRATION TO SURFACE-ENHANCED RAMAN SCATTERING INTENSITIES

2.1 Introduction

Gold nanoparticles exhibit unique extinction spectra that arise from their localized surface plasmon resonance (LSPR),[179, 180] an optical phenomenon not observed in bulk material.[18, 20, 22, 34] LSPR spectra are dependent on many parameters, including nanoparticle shape, size, local dielectric environment, stability, and surface chemistry.[26-28] Control over these parameters leads to predictable optical properties, allowing for their integration into many applications, such as: optical filters,[181, 182] photon energy transport,[183, 184] biological diagnostics,[185, 186] lasers,[187, 188] and surface-enhanced Raman scattering (SERS) detection.[37-39, 189]

The localized electromagnetic fields accompanying LSPR excitation are a key factor in the intense signals observed in all surface-enhanced spectroscopies, including SERS.[11, 66] With SERS, the intensity of the normal Raman effect is increased up to 9 orders of magnitude,[61, 94, 115-117] which is used to improve molecular detection. SERS is generally attributed to a combination of at least two major contributions. The largest factor of SERS enhancements depends on the LSPR or strong electromagnetic (EM) fields that extend several nanometers away from a nanostructure.[17-24, 115, 116] Although still debated,[190, 191] SERS enhancements can be maximized when the excitation wavelength is tuned to overlap

with the LSPR.[118, 192] The second contribution to SERS enhancements is a short-range chemical (CHEM) effect that arises from the electronic coupling of the charge transfer between a molecule and a nanostructure.[120, 193, 194] Both mechanisms are hypothesized to broaden the molecular orbitals of the adsorbate, which subsequently overlap with the LSPR of the nanostructures.[119, 191, 195]

Because SERS provides sensitive and specific molecular information in aqueous media, detection of biological[196, 197] and environmental[198, 199] species are often targeted. Despite their widespread use, applications that use solution-phase metal nanoparticles[37, 200-202] for reproducible and quantifiable SERS responses remain limited because of unstable and unpredictable short- and long-range interactions between nanoparticles in solution that result upon the addition of the target molecule.[161, 162] Analysis is further complicated when solution-phase nanoparticles are used because large clusters form,[203] leading to uncontrolled nanoparticle aggregation. Furthermore, varied surface charges can result when the pH, ionic strength, or molecular composition of the surrounding solution is modified.[204, 205] Although quantitative SERS detection platforms were previously reported for gold nanoparticles,[206-209] nanoparticle extinction and SERS spectra were not simultaneously reported. As a result, microscopy,[210] microfluidics,[210] and internal standards[207, 211] were previously used to quantify SERS measurements.

This study demonstrates that the molecular surface coverage of the target molecule 2-naphthalenethiol (2-NT) and known gold nanoparticle concentrations are critical in generating correlated extinction and SERS signals using solution-phase

nanostructures. Gold nanoparticle and 2-NT concentrations were varied while nanoparticle extinction and SERS signal intensities of the molecule were monitored. Three-dimensional (3D) contour plots demonstrated that the behavior of extinction and SERS intensities were correlated when molecular surface coverage was less than an estimated[212] monolayer surface coverage. Above this value, large but irreproducible SERS signal intensities were observed. This report was the first study in which molecular surface coverage on solution-phase gold nanoparticles is correlated with simultaneous LSPR and SERS measurements. These results should facilitate the predictable detection of other target molecules when quantitative SERS detection is required.

2.2 Experimental Methods

2.2.1 Reagents

Gold (III) chloride trihydrate ($HAuCl_4 \cdot 3H_2O$), sodium chloride (NaCl), and 2-NT (99%) were purchased from Sigma (St. Louis, MO). All other chemicals were purchased from Fisher Scientific (Pittsburg, PA). Water (18.2 $M\Omega\ cm^{-1}$) was obtained using a nanopure system from Barnstead (Dubuque, IA). For all experiments, glassware was cleaned with *aqua regia* (3:1 $HCl:HNO_3$), rinsed thoroughly with water, and oven-dried overnight before use.

2.2.2 Gold Nanoparticle Synthesis

Gold nanoparticles were synthesized via citrate reduction.[161, 213] Briefly, a 1 mM $HAuCl_4 \cdot 3H_2O$ solution (50 mL) was refluxed and vigorously stirred for 15 minutes. Once a rolling boil was achieved, 5 mL of a 39 mM tri-sodium citrate solution was quickly added. The resulting solution was refluxed for an additional 10

minutes and then allowed to equilibrate to room temperature while stirring. The resulting average gold nanoparticle diameter (d) was 13.2 ± 1.3 nm, as determined from transmission electron microscopy (TEM).

2.2.3 Transmission Electron Microscopy (TEM)

TEM was performed using a JEOL JEM-1230 microscope equipped with a Gatan CCD camera. Samples were prepared on 400 mesh copper grids that were coated with a thin film of Formvar and carbon (Ted Pella). The nanoparticle solution was diluted in a 50% water−ethanol mixture. The solution (~50 μL) was pipetted onto a grid and promptly drained using filter paper. Over 600 nanoparticles (N) were analyzed using Image-Pro Analyzer 6.1 (Media Cybernetics) to estimate the average diameter of the nanoparticle. Propagated error in the nanoparticle surface area was estimated from TEM data.

2.2.4 Sample Preparation

Following this process, 15.0 nM Au nanoparticles and 2.65 mM 2-NT (in ethanol) stock solutions were prepared and then 2-NT was diluted to 50 μM in water. The citrate concentration was maintained at 0.25 mM for all measurements. After adding 2-NT and the nanoparticles into a cuvette, the mixture was briefly vortexed before any measurements. Extinction and SERS spectra were collected every 10 seconds and one minute, respectively, for one hour. Gold nanoparticle concentration was estimated[214] via extinction spectroscopy using an extinction coefficient (ε_{520nm}) = 2 x 10^8 $M^{-1} \cdot cm^{-1}$.

2.2.5 Simultaneous Extinction and SERS Spectroscopy

Extinction and SERS measurements were performed simultaneously using a modified sample holder and 1 cm quartz cuvette. LSPR spectra were collected near the top of the cuvette using an UV-vis spectrometer (HR4000 or USB4000, Ocean Optics). All spectra were baseline-adjusted at ~450 nm to account for white light source variations.

Raman scattering was monitored near the base of the cuvette with excitation occurring perpendicular to the extinction light source using an ExamineR 785 (Delta Nu) and the following parameters: excitation wavelength (λ_{ex}) = 785 nm, integration time (t_{int}) = 10 s, and laser power (P) = 52 mW. All spectra were background-corrected using samples that contained only nanoparticles (no 2-NT). Random XYZ and Renka-Cline matrix conversion methods (Origin 7.5) were used to interpolate and to generate 3D extinction and SERS plots. Only spectral intensities greater than three times the spectral noise were used in analysis. Spectral noise was estimated as the standard deviation of the baseline from 1900 – 1700 cm^{-1}.

2.3 Results and Discussion

2.3.1 Time-Dependent Extinction and SERS Spectral Responses

The SERS phenomenon originates from interactions between Raman-active vibrational modes of a molecule and the chemical and electromagnetic properties of noble metal nanoparticles.[11, 66, 190, 191, 209] SERS signals typically increase as nanoparticle aggregation occurs, which induces heightened electromagnetic fields in gaps between nanostructures.[215] Solution-phase nanostructures are intrinsically unstable in the presence of target molecules, which can be considered either a positive

or a negative effect. The instability of the nanoparticles could be viewed as positive, given increased SERS signals, or as negative, because nanoparticle aggregation is difficult to control, thereby limiting the reproducibility and/or quantitative capabilities of SERS intensities for signal transduction.

Both of these experimental conclusions are related and observed via time-dependent changes in the electromagnetic properties of the nanoparticles. An example of these variations is shown in Figure 2.1. A 4 nM gold nanoparticle (d = 13.2 ± 1.3 nm) solution incubated with 6 μM 2-NT exhibits time-dependent extinction (Figure 2.1B) and SERS (Figure 2.1C) spectral responses. The extinction maximum wavelength (λ_{max}) is centered at 520.4 nm, then red-shifts and decreases in magnitude as a new lower energy extinction band develops with increasing time (Figure 2.1B). This red-shift and decrease in the magnitude of the λ_{max} indicate molecule-induced nanoparticle aggregation. As this occurs, the SERS signal from 2-NT increases with increasing time (Figure 2.1C).

Correlated trends are observed between low-energy extinction and SERS vibrational bands. Both extinction and SERS signals are dynamic and increase steadily over the first ~15 minutes of the nanoparticle-molecule incubation period. For instance, time-dependent changes in extinction at 785 nm and the 2-NT vibrational mode at $\bar{\nu}_{vib}$ = 1064 cm^{-1} increase, then slightly decrease (Figure 2.1D). These plasmonic trends are attributed to nanoparticle aggregation and sedimentation, respectively. 2-NT displaces the stabilizing citrate molecules on the nanoparticle surface, thus destabilizing the nanoparticles via double-layer disruption. This disruption, in turn facilitates: (1) additional 2-NT binding to the nanoparticle surface,

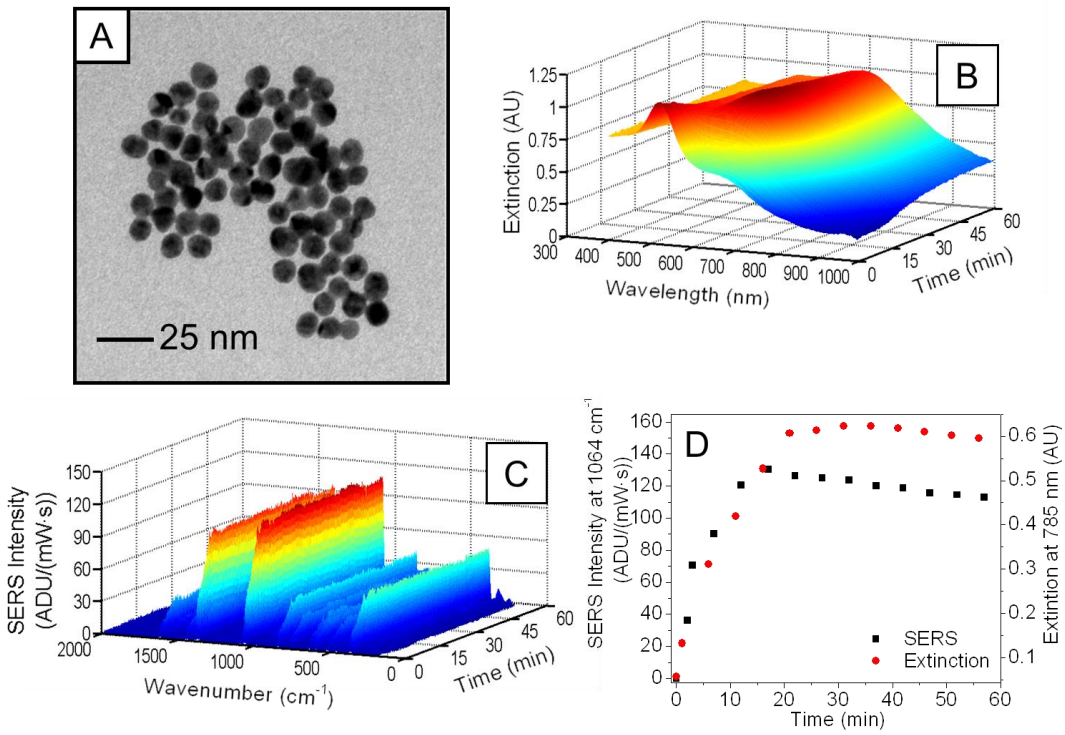

Figure 2.1 Structural and optical characterization of gold nanoparticles. A) TEM image of the gold nanoparticles used (d = 13.2 ± 1.3 nm). B) Extinction and C) corresponding SERS spectra for 4 nM gold nanoparticles incubated with 6 µM 2-NT are shown over a 1 hour period. D) Comparison of the (■) SERS intensity at 1064 cm^{-1} and (●) extinction at 785 nm are plotted *vs.* time. SERS parameters: t_{int} = 10 seconds, λ_{ex} = 785 nm, P = 52 mW.

(2) nanoparticle aggregations, and consequently, (3) an increase in both low-energy extinction and SERS intensities. Finally, after the extinction and SERS signals maximize, both signals decrease with increasing time.

To evaluate how extinction and SERS intensities vary with target molecule concentration, a 4 nM gold nanoparticle solution was mixed with 2-NT concentrations varying from 0.5 – 11 μM. Changes in extinction at the initial LSPR maximum wavelength, the Raman excitation wavelength, and at an energy between the Raman excitation and molecular vibrational energies were tracked at λ = 520 (Figure 2.2), 785 (Figures 2.3A), and 821 nm (Figure 2.4), respectively. Comparisons between these wavelengths and SERS intensities at 1064 cm^{-1} (Figure 2.3B), as a function of both time and 2-NT concentration, were subsequently evaluated. As expected, extinction at 520 nm decreases with increasing time for all 2-NT concentrations. In contrast, extinction at both 785 nm and 821 nm increases with increasing 2-NT concentrations for a fixed incubation time. Since extinction trends are similar at the two lower energy wavelengths, extinction at 785 nm was chosen for evaluation in all subsequent studies. Importantly, extinction at 785 nm and SERS intensities systematically increase and saturate more quickly than similar experiments performed with lower 2-NT concentrations. Notably, these trends are reproducible when 4 nM gold nanoparticle solutions are incubated with less than 6 μM 2-NT concentrations. Similar trends in extinction and SERS intensities are observed above 6 μM 2-NT concentrations, but the magnitude and rate of these changes are inconsistent (data not shown).

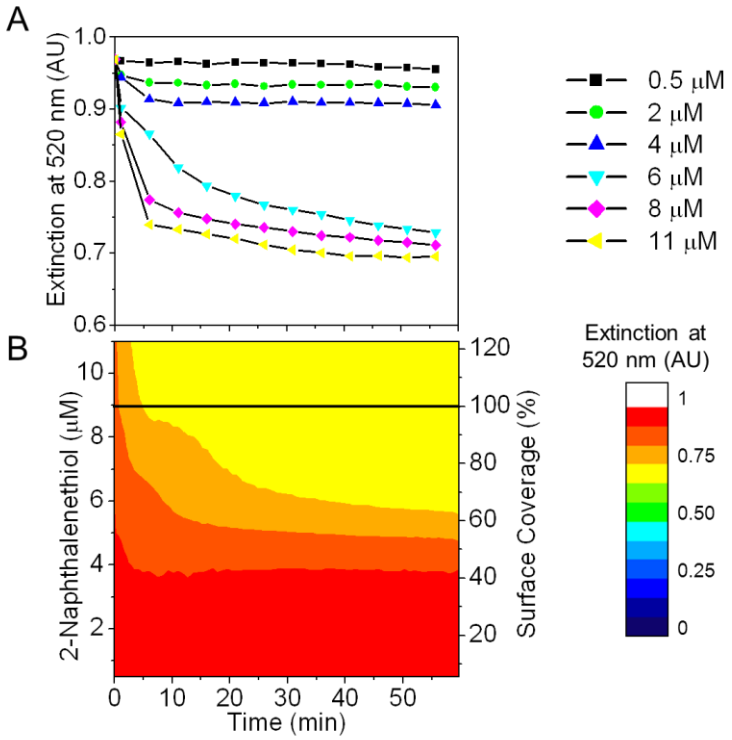

Figure 2.2 Extinction intensity at λ = 520 nm for 4 nM gold nanoparticles. A) 2D time-dependent spectral changes for (-■-) 0.5 , (-●-) 2, (-▲-) 4, (-▼-) 6, (-♦-) 8, and (-◄-)11 μM 2-NT; and B) 3D contour map as a function of time. The black line represents 100% theoretically calculated surface coverage of 2-NT on gold nanoparticles.

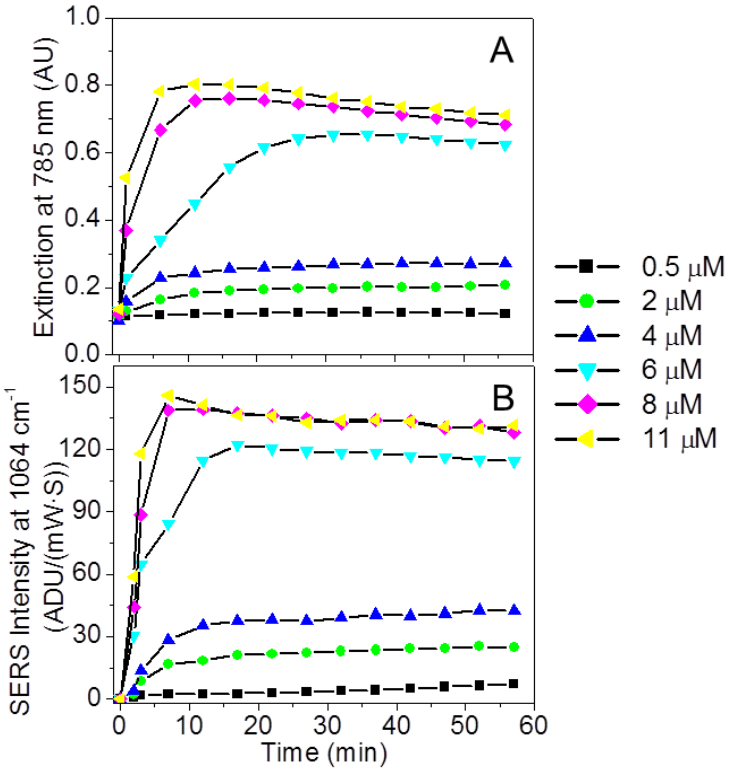

Figure 2.3 2-NT concentration and time-dependent spectral changes for 4 nM gold nanoparticles. A) Extinction at 785 nm and B) SERS intensity at 1064 cm^{-1} for (-■-) 0.5 , (-●-) 2, (-▲-) 4, (-▼-) 6, (-♦-) 8, and (-◀-) 11 µM 2-NT are included.

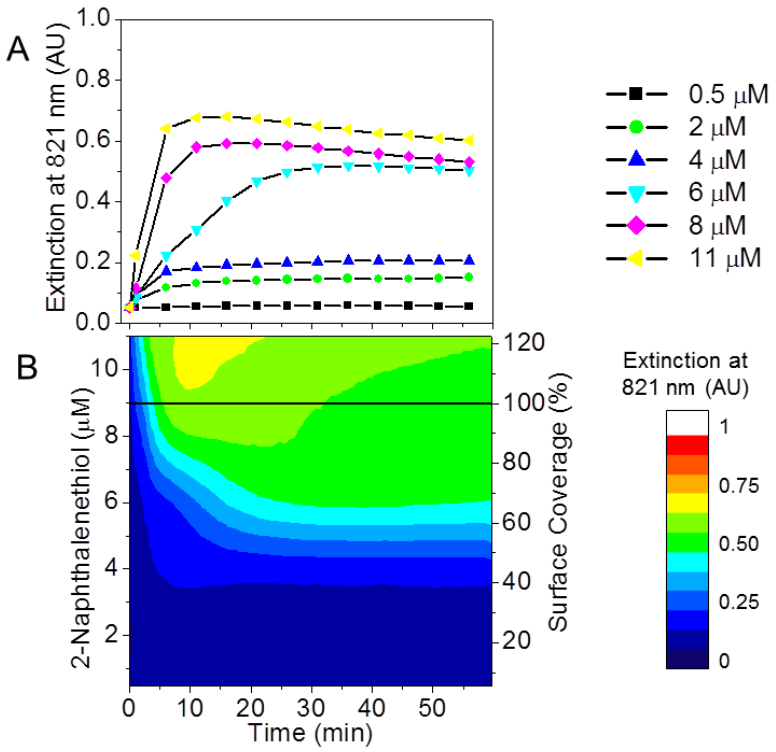

Figure 2.4 Extinction intensity at λ = 821 nm for 4 nM gold nanoparticles. A) 2D time-dependent spectral changes for (-■-) 0.5 , (-●-) 2, (-▲-) 4, (-▼-) 6, (-♦-) 8, and (-◀-) 11 μM 2-NT; and B) 3D contour map as a function of time. The black line represents 100% theoretically calculated surface coverage of 2-NT on gold nanoparticles.

2.3.2 Extinction and SERS Spectral Responses as a Function of Surface Coverage

To evaluate how nanoparticle concentration impacts these measurements, both 2-NT concentration and time-dependent extinction and SERS changes were monitored. Nanoparticle concentration was estimated using the method developed by Haiss.[214] Next, both gold nanoparticle and 2-NT concentrations were varied systematically and monitored as a function of time. For each nanoparticle concentration, 2-NT concentrations were selected to provide varying degrees of citrate displacement from the nanoparticle surface. Molecular surface coverage was estimated using the following equation:

$$\%\ \text{Surface Coverage} = \frac{SA_{2\text{-NT}}}{SA_{NP}} * \frac{C_{2\text{-NT}}}{C_{NP}} * 100\,\% \qquad (2.1)$$

$$SA_{NP} = 4\pi\left(\frac{13.2\ \text{nm}}{2}\right)^2 = 547 \pm 107\ \text{nm}^2/\text{nanoparticle} \qquad (2.2)$$

where $SA_{2\text{-NT}}$ is the surface area occupied by a 2-NT molecule (0.244 nm^2/molecule),[212] SA_{NP} is the available surface area per nanoparticle (equation 2.2), and $C_{2\text{-NT}}$ and C_{NP} are 2-NT and nanoparticle concentrations, respectively. It should be noted that the 2-NT footprint will vary with orientation and packing density, and each nanoparticle exhibits a unique crystal structure and geometry (i.e., distinct surface area). Consequently, this molecular coverage estimation represents only an average molecular surface coverage on all nanoparticles in solution. Therefore, each 2-NT concentration yields an estimated molecular surface coverage only if the nanoparticle concentration is known.

Time-dependent trends in extinction at 785 nm and SERS intensities at 1064 cm^{-1} for each nanoparticle concentration (A = 2 nM, B = 4 nM, C = 6 nM, and D = 8 nM) are shown in Figures 2.5 and 2.6, respectively. To maximize data clarity, 3D contour maps are included, where the x-axis represents time, the y-axes represent molecular concentration (left) and estimated surface coverage (right), and the colors represent either extinction at λ = 785 nm or SERS intensity at $\bar{\nu}_{vib}$ = 1064 cm^{-1}. Each fixed nanoparticle concentration map represents spectral evaluation of at least 7 concentrations of 2-NT collected for 60 minutes. In all contour maps, a solid black line is included, which represents a monolayer coverage of 2-NT, depending on nanoparticle concentration. As a result, the nanoparticle surface area will saturate when 4.5, 9.0, 13.5, and 18.0 µM 2-NT is added to and equilibrated with 2, 4, 6, and 8 nM gold nanoparticle solutions, respectively.

Several trends are observed in both extinction (Figure 2.5) and SERS intensities (Figure 2.6). First, spectral intensities increase more rapidly over the first 5 – 10 minute period as 2-NT concentration increases (for each fixed nanoparticle concentration) *vs.* later times. Spectral intensities increase linearly below the theoretical 2-NT monolayer coverage on the gold nanoparticles, then saturate for 2 nM gold nanoparticle concentration (Figures 2.5A and 2.6A). Additional increases in 2-NT concentration yield similar behaviors; however, the spectral signals decrease with longer duration. For instance, the extinction and SERS intensities from 4 - 8 nM gold nanoparticle concentrations (Figures 2.5B - D and Figures 2.6B - D) saturate in less than 10 minutes and then decrease. Spectral maxima are observed at ~100 % 2-NT surface coverage for both extinction and SERS measurements for all nanoparticle

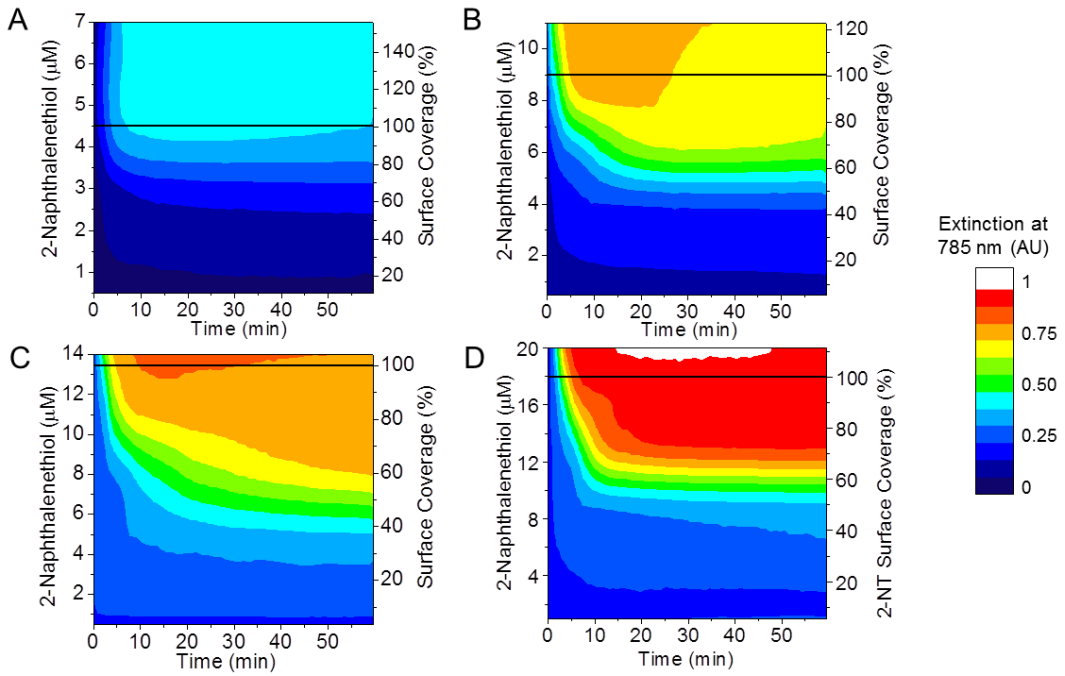

Figure 2.5 3D contour maps of extinction at λ = 785 nm *vs.* time for A) 2, B) 4, C) 6, and D) 8 nM gold nanoparticle concentrations. The black line represents theoretically calculated 100% 2-NT surface coverage on gold nanoparticles.

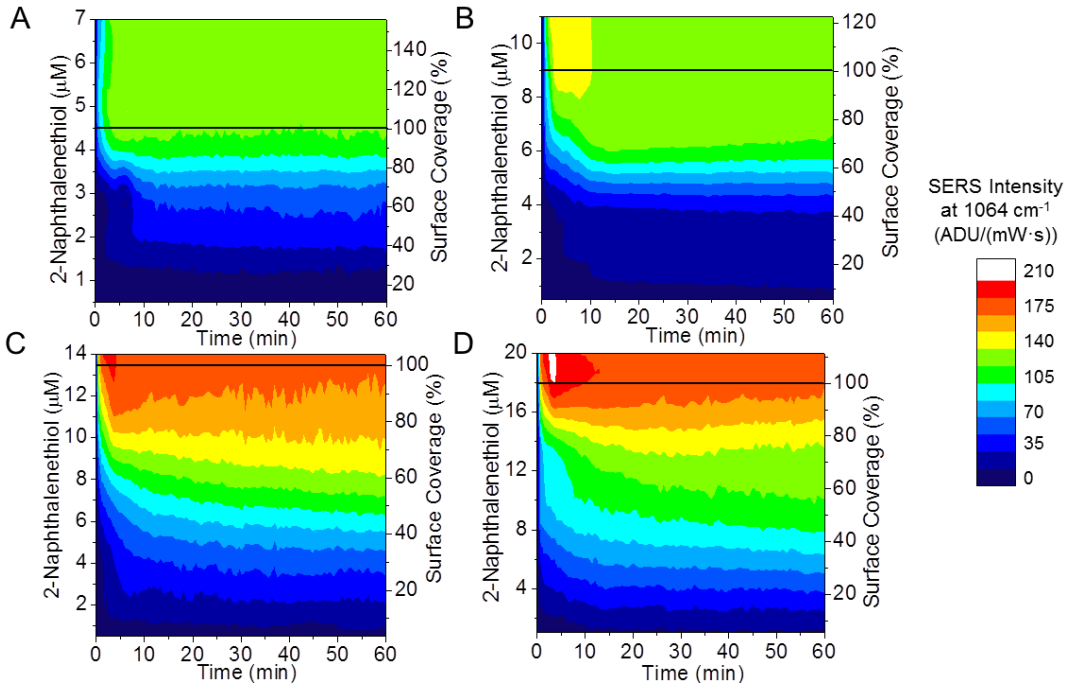

Figure 2.6 3D contour maps of SERS intensities at $\bar{\nu}_{vib}$ = 1064 cm^{-1} *vs.* time for A) 2, B) 4, C) 6, and D) 8 nM gold nanoparticle concentrations. The black line represents theoretically calculated 100% 2-NT surface coverage on gold nanoparticles.

concentrations studied. Of note, extinction signals reach maximum values more slowly and persist for longer time periods than that for the SERS data, thereby indicating that the SERS signals are likely dominated by large nanoparticle aggregates that form quickly then settle out of solution. This would be in contrast to extinction results from the average optical response, which are by all nanoparticles in solution. Nanoparticle collisions, and therefore nanoparticle aggregates, are more likely to form when the nanoparticle concentration increases and the double layer is disrupted by the thiolated molecules.

Clearly, both extinction and SERS intensities increase with time and 2-NT concentration then saturate at ~100 % surface coverage before decreasing. At a fixed 2-NT concentration and varying nanoparticle concentration, extinction and SERS data reveal several distinct trends. First, Figures 2.5 and 2.6 show that when a fixed 2-NT concentration is incubated with varying nanoparticle concentrations, extinction and SERS data (at a fixed time) respond systematically. For instance, 4 μM 2-NT causes the extinction at 785 nm for 2, 4, 6, and 8 nM nanoparticle concentrations to saturate at ~0.40, 0.30, 0.28, and 0.24 AU, respectively. Noticeably, the saturated extinction values are inversely proportional to nanoparticle concentration. Significantly, this response is directly proportional to 2-NT surface coverage, which is ~90, 45, 30 and 22% for the respective nanoparticle concentrations. These trends are clearly dependent on nanoparticle concentration. Extinction, measured at λ = 785 nm, overlaps with the low-energy LSPR band of gold nanoparticle aggregates. As a result, SERS intensities at a fixed 2-NT concentration, but varying nanoparticle concentrations, are also inversely proportional to low 2-NT surface coverages. For

instance, 4 μM 2-NT produces SERS signal intensities of ~80, 55, 45, and 40 $ADU \cdot mW^{-1} \cdot s^{-1}$ for 2 (90 %), 4 (45 %), 6 (30 %) and 8 (22 %) nM nanoparticle concentrations (surface coverages), respectively.

In contrast, the largest SERS signals are observed at 130, 155, 195, and 220 $ADU \cdot mW^{-1} \cdot s^{-1}$ for 2, 4, 6, and 8 nM nanoparticle concentrations, respectively. In each case, this maximum value corresponds to 2-NT concentrations that should form a full 2-NT monolayer because of the strong binding affinity between sulfur and the gold nanoparticle surfaces. When additional 2-NT is incubated with each nanoparticle solution, trends in SERS signal changes are inconsistent. In summary, these trends are consistent with SERS signals which correspond with relatively stable LSPR properties (low-molecular surface coverage) while the large, and subsequently inconsistent, SERS measurements arise from molecule-induced nanoparticle instability and plasmonic changes.

2.3.3 Correlated Three-Dimensional (3D) Spectral Maps

Three-dimensional maps allow for straightforward comparisons and correlations between parameters that affect spectral signals. When sufficient 2-NT is added to saturate the nanoparticle surface (100 % surface coverage), extinction values maximize in ~5, 10, 15, and 20 minutes, while SERS intensities peak after ~7, 5, 4, and 2 minutes for 2, 4, 6, and 8 nM nanoparticle concentrations, respectively. It is hypothesized that trends in extinction data are dictated by molecular (2-NT) concentration, and as a result, by the average distance between and the double-layer thickness surrounding the nanoparticles as well. Conversely, SERS signals are

dominated by quickly forming nanoparticle aggregates that efficiently settle out of solution.

To test this hypothesis, extinction and SERS intensities at a fixed time (5 minutes) were plotted in 3D contour maps for extinction and SERS spectral responses (Figures 2.7A and 2.7B, respectively) to evaluate correlated trends between nanoparticle and molecule concentrations. These plots were generated using at least 7 concentrations of 2-NT (x-axis) vs. 4 nanoparticle concentrations (y-axis) with figure colors representing spectral magnitudes. A 5 minute incubation time was selected, as it correlates with the average time required to observe maximized SERS intensities. The ~100 % surface coverage (solid line) and propagated error in nanoparticle surface area (dashed line) are included in both contour maps. Surface coverage exceeds a monolayer surface coverage to the right and below the solid line.

As shown in Figure 2.7, both extinction at λ = 785 nm and SERS intensities at $\bar{\nu}_{vib}$ = 1064 cm^{-1} increase linearly with increasing 2-NT concentration (fixed nanoparticle concentration) when the theoretical surface coverage is less than a monolayer. This response demonstrates that as 2-NT surface coverage increases, citrate molecules are quickly displaced and signal changes are dominated by 2-NT surface coverage and/or slight plasmonic variations. Above a monolayer surface coverage of 2-NT, both extinction and SERS signals maximize then decrease. This behavior suggests electromagnetic coupling between the solution-phase nanostructures, which are able then to settle out of solution. Trends in nanoparticle concentration are also apparent. For a fixed sub-monolayer 2-NT surface coverage addition, both extinction and SERS data are largely independent of nanoparticle

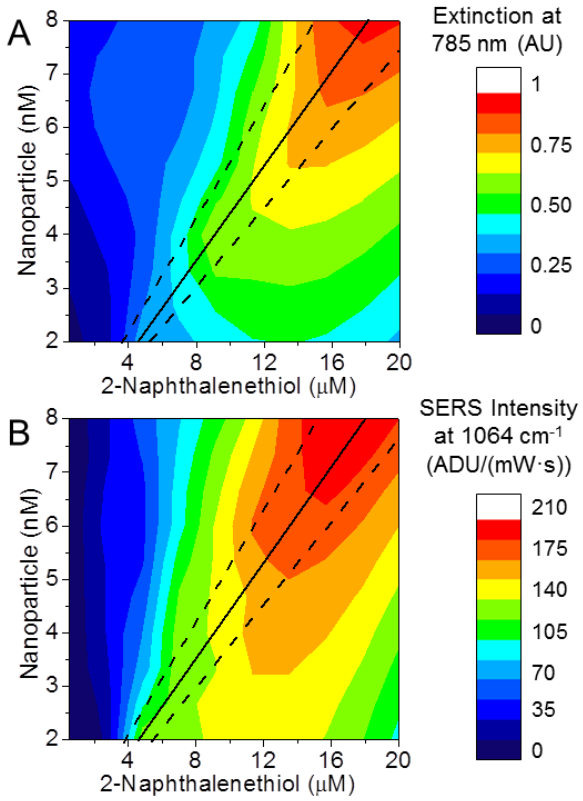

Figure 2.7 3D contour maps correlating A) extinction at 785 nm and B) SERS intensity at 1064 cm^{-1} for 2-NT as a function of both gold nanoparticle and 2-NT concentrations (incubation time = 5 minutes). The solid black lines represent estimated monolayer surface coverage of 2-NT on the surface of gold nanoparticles. The error in nanoparticle diameter was used to propagate the uncertainty of these values (range shown with dashed lines). On average, surface coverage exceeds a monolayer to the right and below the solid line.

concentration. At higher 2-NT concentrations, both extinction and SERS data increase systematically, once again suggesting that nanostructures are undergoing aggregation, which then facilitates electromagnetic coupling between nanoparticles.

2.4 Conclusion

Solution-phase nanoparticles are commonly used as SERS substrates. Despite their extensive use in various applications, the ability to use solution-phase nanoparticles as quantifiable SERS substrates are limited by the inherent instability of the nanoparticles, the homogeneity (or lack thereof) of nanoparticle morphology, and/or unknown/unreported nanoparticle concentrations. Herein, nanoparticle aggregation, and as a result extinction and SERS spectral intensities, have been shown to be impacted by molecular surface coverage, a variable that depends on nanoparticle-molecule interactions, as well as on both nanoparticle surface area and plasmonic changes. By plotting extinction and SERS intensities as a function of both nanoparticle and 2-NT concentrations, correlated extinction and SERS intensities were observed at sub-monolayer surface coverages. Above this value, nanoparticles aggregated rapidly and uncontrollably when the molecule interacted with the nanoparticle surface, which induced electromagnetic coupling between nanostructures – a result that thereby led to relatively larger but unpredictable spectral intensities. These data indicate that relative nanoparticle surface area and molecular surface coverages are key parameters in evaluating both plasmonic and quantitative SERS assays. Further exploitation of these phenomena should lead to more predictable SERS signal for quantifiable molecular detection.

CHAPTER III

PURIFICATION IMPLICATIONS ON SERS-ACTIVITY OF SILICA-COATED GOLD NANOSPHERES

3.1 Introduction

Stabilization and isolation of metal nanoparticle cores are vital for the generation of reproducible solution-phase, surface-enhanced Raman scattering (SERS) substrates and quantitative measurements. Metal nanoparticle stability was previously promoted using core@shell nanostructures where the shell was composed of polymers (metal@polymer),[164] dendrimers (metal@dendrimer),[165] and silica (metal@SiO_2).[4, 161, 167, 216] Silica, for instance, is a structurally versatile, biocompatible, and optically transparent protective material that can be subsequently modified with a variety of different chemical functionalities. Unfortunately, the SERS capabilities of these nanostructures are generally limited to uses that include silica-entrapped SERS reporter molecules rather than direct SERS detection.[161, 177, 217]

Nanoparticle uniformity is important for generating quantitative SERS data, but despite synthetic improvements,[218] most solution-phase nanoparticle preparations yield some degree of heterogeneity. This heterogeneity causes variations in the resulting chemical and physical properties of the nanomaterials. This lack of "quality control" leads to poor application reproducibility. For instance, slight variations in nanoparticle shape, size, and/or cluster distribution results in different SERS activities.[11, 156, 219, 220] In order for solution-phase SERS substrates to become part of a widely used quantitative technique, methods that either improves the

synthesis or substrate purity post-synthesis are needed so that structure–function relationships can be developed and exploited.

Previously, diafiltration,[221] centrifugation,[221-225] or chromatographic techniques[223, 226-232] was used to improve the quality of nanostructures post-synthesis. For instance, analytical ultracentrifugation of silica-coated gold nanoparticles and/or clusters separate these SERS-active nanostructures as a function of size (i.e., sedimentation coefficient).[233] Improvements in nanostructure uniformity in each fraction led to more consistent SERS activity. While this and other techniques offered some degree of purification in nanomaterial shape and size, high concentrations of salt and/or surfactants are often used to improve the purification method. Surfactants, for example, are extremely difficult to remove from surfaces,[234] and as a result, can change nanoparticle surface chemistry and reduce the SERS activity of a nanostructure thereby compromising structure-function evaluation.

Herein, hydrophobic interaction chromatography was used to process and purify silica-coated gold ($Au@SiO_2$) nanoparticles. Silica shell thickness on the gold nanoparticle cores was varied from 1.7 – 14.5 nm. The electromagnetic stability of the metal cores and SERS activity enhanced by the nanostructures were evaluated as a function of both silica shell thickness and method of post-synthesis purification (centrifugation and washing with and without chromatographic purification). Importantly, the electromagnetic stability of the gold cores was improved and variations in SERS activity were eliminated upon implementing the extra chromatographic quality control step. After chromatographic purification, SERS

activity was only observed for gold nanoparticles stabilized in silica shells thinner than 2 nm. These results are expected to depend on the inherent plasmonic properties of the metal cores and SERS excitation wavelengths. In all cases, this post-synthesis step could provide an easily implemented opportunity for improving the quality control and thereby reproducibility of resulting SERS measurements when solution-phase substrates are utilized and quantitative detection is targeted.

3.2 Experimental Methods

3.2.1 Chemicals

Gold (III) chloride trihydrate, sodium citrate dehydrate, amberlite MB-150 mixed bed exchange resin, (3-aminopropyl)trimethoxysilane (APTMS), tetraethyl orthosilicate (TEOS), sodium chloride (NaCl), sodium trisilicate (27%), 2-naphthalenethiol (2-NT), and tetraethyl orthosilicate were purchased from Sigma (St. Louis, MO). Ethanol, ammonium hydroxide (NH_4OH), hydrochloric acid (HCl), and nitric acid (HNO_3) were purchased from Fisher Scientific (Pittsburgh, PA). Ultrapure water (18.2 $M\Omega \cdot Cm^{-1}$) was obtained using a Nanopure System from Barnstead (Dubuque, IA). For all experiments, glassware was cleaned with aqua regia (3:1 HCl/HNO_3), rinsed thoroughly with ultrapure water, and oven (glass) or air (plastic) dried overnight before use.

3.2.2 Microporous Silica-Coated Gold Nanoparticles Synthesis

Silica-coated gold ($Au@SiO_2$) nanoparticles were synthesized via a modified Stöber method.[161, 167, 235-237] First, gold nanoparticles were synthesized using well-established citrate reduction techniques[156, 161, 202, 213] and coated with varying silica shell thicknesses by modifying the sodium silicate concentration.[161,

167, 237] Briefly, 150 mL of the gold nanoparticle stock solution was diluted with 150 mL of water. Amberlite resin was added to the diluted gold nanoparticles to reduce the ionic strength of the solution. The amberlite resin was then removed from the nanoparticle solution by filtration. The pH of the nanoparticle solution was adjusted to 5 using 1 M HCl. Next, the nanoparticle solution was divided into 6 samples of 50 mL each. The nanoparticle surfaces were made vitreophilic via the addition of 1 mM APTMS to obtain 75% surface coverage. After 15 minutes, a 2.7 % sodium silicate solution of different concentrations was added to each sample flask to obtain various silica shell thicknesses, and the mixture was stirred for 24 hours. To induce the precipitation of unreacted silica, the mixture was added to a final ratio of 1:4.4 water/ethanol. After 6 hours, the silica shells were thickened by adding a 1:1 concentration ratio of TEOS/1 mM APTMS at a high pH (~11.0). The pH was adjusted with concentrated ammonium hydroxide. After 16 hours of incubation time, the reaction was stopped and washed 3 times with ethanol to decrease the solution pH to 7. This step was followed by another 3 washes with water to remove ethanol using centrifugation (30 min, 10 000 rpm).

3.2.3 Silica-Coated Gold Nanoparticle Purification

A portion of each composite nanoparticle solution was carefully purified to remove uncoated or partially silica-coated nanoparticles using hydrophobic interaction chromatography. The column was packed with slurry of Sephadex-G50 prepared in a 75:25 ration of water/ethanol. This column matrix is composed of a long chain of hydrophobic dextran molecules and is typically used to separate small molecules based on their hydrophobic interaction with the stationary phase (column

matrix). The column was equilibrated using ultrapure water prior to sample purification to remove ethanol. Next, 2 mL of 15 nM Au@SiO_2 nanospheres were added to the Sephadex-G50 column. Because the bare or partially-coated gold nanoparticles present in the sample are hydrophobic, they interact with the column matrix very tightly or are retained by the column matrix. However, fully coated Au@SiO_2 nanoparticles, which are less hydrophobic in nature, are eluted from the column matrix. These purified nanostructures were redispersed in water. The concentration of the purified Au@SiO_2 nanoparticle solutions was calculated using LSPR spectroscopy and an assumed extinction coefficient (ε_{520nm}) of 2 × 108 M^{-1} ·cm^{-1} for future measurements.[214]

3.2.4 Transmission Electron Microscopy (TEM)

TEM was performed using a JEOL JEM-1230 microscope equipped with a Gatan CCD camera. Samples were prepared on 400 mesh copper grids coated with a thin film of Formvar and carbon (Ted Pella). The solution (~50 μL) was pipetted onto a grid and promptly drained using filter paper. At least 300 nanoparticles (N) were analyzed using Image Pro Analyzer 6.1 (Media Cybernetics) to estimate the mean nanoparticle diameter. Propagated error in the nanoparticle surface area is estimated from TEM data.

3.2.5 Sample Preparation

Four nM of centrifuge-purified and chromatographic-purified Au@SiO_2 nanospheres were incubated in 100 mM NaCl for 0, 1, and 12 hours, respectively. A LSPR spectrum was collected for each sample to make sure that nanostructures were stable after chromatographic purification. For the direct SERS detection of 2-NT, 50

µM 2-NT solutions were prepared in water from a 2.65 mM 2-NT stock in ethanol. After the addition of 10 µM of 2-NT and 4.0 nM 0f $Au@SiO_2$ nanoparticles into a Raman vial, the mixture was vortexed for 3 to 5 seconds, and SERS spectra were collected for 1 hour at one every 60 seconds. Silica-coated gold ($Au@SiO_2$) nanoparticle concentration was estimated[214] via extinction spectroscopy using an extinction coefficient (ε_{520nm}) = 2 x 10^8 $M^{-1} \cdot cm^{-1}$.

3.2.6 Extinction Spectroscopy

Localized surface plasmon resonance (LSPR) spectra were collected using a 1.0 cm path length disposable cuvette sample holder and an ultraviolet-visible (UV-vis) spectrometer (Ocean Optics USB4000). All spectra were smoothed, and the area under the curve from 650 to 850 nm was estimated.

3.2.7 SERS Spectroscopy

SERS spectra were collected near the base of a 0.7 cm path length Raman vial using an Advantage 200A Raman spectrometer (DeltaNu) and the following parameters: excitation wavelength (λ_{ex}) = 632.8 nm, integration time (t_{int}) = 60 s, and laser power (P) = 2 mW. All spectra were background corrected using samples that contained only nanoparticles (no 2-NT) and MatLab R2013a (Math Works). Only spectral intensities greater than 3 times the spectral noise were used in analysis. Spectral noise was estimated as the standard deviation of the baseline from 1900 – 1700 cm^{-1}.

3.3 Results and Discussion

3.3.1 Synthesis and Characterization of Centrifuge Purified Au Nanospheres Encapsulated with Various Silica Shell Thicknesses

The SERS effect exhibits a well-known distance dependence relationship between the nanostructured surface and Raman chromophore, which depends on both chemical and electromagnetic effects.[119, 178, 238-241] Several theoretical models were previously used to describe quantitatively the relationship between Raman intensity and the surface-molecule distance raised to the negative 10 power ($distance^{-10}$) dependence.[119, 242, 243] To control this distance for SERS detection on spherical nanospheres, various silica shell thicknesses are grown on solution-phase gold nanoparticles. Silica-stabilized gold ($Au@SiO_2$) nanoparticles[161, 167] are synthesized in a three-step process. First, the gold nanoparticles ($d = 12.0 \pm 1.3$ nm) are made vitreophilic using (3-aminopropyl) trimethoxysilane. Next, 0.4 – 0.9 mM sodium silicate is added to the nanoparticle solution to promote silica condensation. Finally, Stöber growth is facilitated by adding ethanol and tetraethyl orthosilicate in pH 11. Following preparation, the nanostructures are rinsed at least three times with ethanol and water. The samples are centrifuged at 12,280 xg and redispersed to known concentrations using previously described methods.[161]

A summary of the resulting silica-coated gold ($Au@SiO_2$) nanoparticles is shown in Figure 3.1. TEM images reveal that the silica shell thickness can be systematically increased by varying the moles of silica added during shell growth. Two interesting observations are noted. First, as sodium silicate concentration increases, the average silica shell thickness ($T \pm$ propagated error) increases. For instance, the silica shell

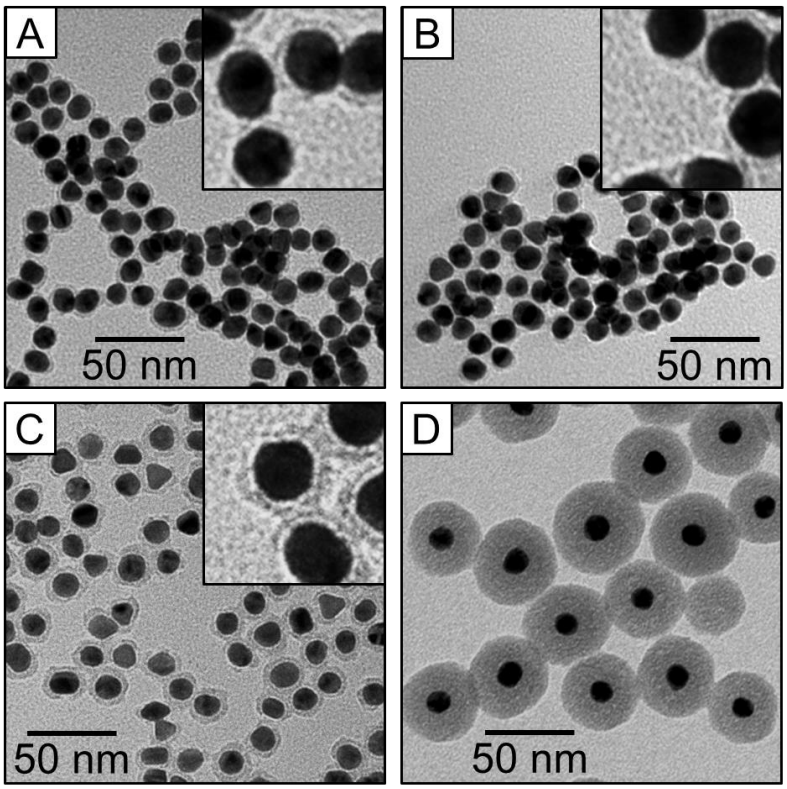

Figure 3.1 Representative TEM images of Au nanoparticles (core diameter (d) = 12.0 ± 1.3 nm) encapsulated in silica shells with thicknesses (T) of (A) 1.7 ± 1.1 nm, (B) 2.3 ± 1.2 nm, (C) 4.2 ± 1.2 nm, and (D) 14.5 ± 2.2 nm. Samples were rinsed and centrifuged prior to analysis. At least 300 nanoparticles were analyzed. The 100 nm × 100 nm insets in panels A−C reveal evidence of silica shell defects (uncoated and/or partially coated gold surfaces).

thickness increases from 1.7 ± 1.1, 2.3 ± 1.2, 4.2 ± 1.2, and 14.5 ± 2.2 nm in Figures 3.1A, 3.1B, 3.1C, and 3.1D, respectively. The changes in silica shell thickness are within 2% of the expected silica shell growth according to the model first developed by Liz-Marzán.[167] Second, each silica-coated nanoparticle sample contains a small population of bare and/or partially silica-coated gold nanoparticles, as well as free silica particles (see Figure 3.1A-C insets and 3.1D). These structural "defects" are consistent with that reported in the literature,[244, 245] but are difficult to control, quantify, and/or reproduce in replicate syntheses.

Evidence of bare and/or partially coated nanostructures is directly observed using LSPR spectroscopy. The LSPR properties of gold nanospheres respond predictably and systematically vary to changes in local dielectric environment[22, 246] and degree of flocculation.[32, 247, 248] To evaluate the electromagnetic stability of the silica-encapsulated gold nanospheres, 4 nM Au@SiO_2 nanoparticle solutions were incubated in 100 mM NaCl solutions. The salt solution should induce either agglomeration for fully coated gold nanoparticle cores or aggregation for partially/uncoated cores, resulting in reversible or non-reversible changes in the optical properties, respectively.

Figure 3.2 contains representative LSPR data for Au@SiO_2 nanoparticles coated in 1.7 nm thick silica shells. In general, similar trends were observed for most Au@SiO_2 nanoparticle samples (data not shown), but were greatest for gold nanoparticles protected in less than 5 nm thick silica shells. As seen in Figure 3.2A, these "washed" Au@SiO_2 nanoparticle samples exhibit an extinction (i.e., sum of absorption and scattering) maximum wavelength (λ_{max}) of 531.1 nm, a value

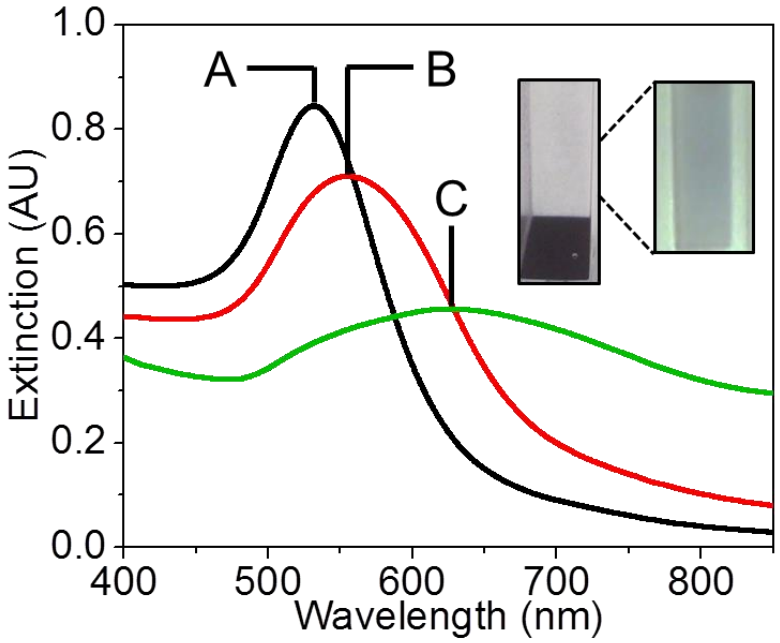

Figure 3.2 LSPR spectra for washed 4 nM Au@SiO_2 nanoparticles (T = 1.7 nm) incubated with 100 mM NaCl for (A) 0 (λ_{max} = 531.1 nm, $A_{650\text{-}850}$ = 1.0), (B) 1 (λ_{max} = 554.1 nm, $A_{650\text{-}850}$ = 2.3), and (C) 12 (λ_{max} = 621.6 nm, $A_{650\text{-}850}$ = 5.4) hours (sample was vortexed). The photographs reveal a blue-colored solution after 12 hours, which indicates nanoparticle aggregation.

consistent with electromagnetically isolated gold nanoparticles coated in a thin silica shell. To quantify spectral changes more sensitive to flocculation, the LSPR spectra were integrated from 650 to 850 nm. These flocculation values were normalized by dividing the raw integrated areas by that for the starting material ($A_{650\text{-}850}$).

Upon the addition of salt to the nanoparticle solution, changes in LSPR wavelengths, extinction magnitudes, line widths, integrated area, and apparent colors are observed. For example, the λ_{max} shifts to 554.1 nm, and the normalized integrated area increased to 2.3 after a 1 hour incubation period (Figure 3.2B). After 12 hours, the sample was vortexed. While a small fraction of the nanoparticles was redispersed into solution, most of the material remained at the bottom of the cuvette. Analysis of LSPR spectra resulted in a λ_{max} of 621.6 nm and an integrated area of 5.35 (Figure 3.2C). Furthermore, the solution turned blue (see in Figure 3.2 inset). These irreversible electromagnetic observations indicate that the gold nanoparticle cores are undergoing electromagnetic coupling at short distances and forming large aggregates.

3.3.2 SERS Spectral Responses as a Function of Silica Shell Thicknesses Using Centrifuge Purified Silica-Coated Gold Nanospheres

The slight structural and surface defects in the Au@SiO_2 nanoparticle shells observed in TEM images shown in Figure 3.1 are important in determining the properties and function of these nanoparticles in a variety of applications, including SERS. Previously, SERS intensities were shown to depend on the distance between the metal surface and adsorbate.[119] These signals arise from charge transfer between Raman-active molecules and the metal surface, as well as nanoparticles' electromagnetic properties. In general, SERS intensities follow ~distance^{-10} but are

difficult to control/predict when using solution-phase nanoparticles because of slight differences in materials syntheses,[249-251] inherent instabilities of the nanostructures upon molecular addition,[156, 162, 251, 252] and surface chemistry defects, including pinholes and edge sites.[238, 242]

To evaluate the impact that structural/surface defects exhibit on the distance dependence of SERS intensities, 4 nM Au@SiO_2 nanoparticle and 10 μM 2-naphthalenethiol solutions were vortexed and allowed to incubate for 1 hour. This molecule was selected because of its thiol group to facilitate binding to bare gold surfaces, if present. Representative SERS spectra are shown for the gold nanoparticles stabilized in various silica shell thicknesses (Figure 3.3A). As expected, SERS intensities for all molecular vibration frequencies decrease as the silica shell thickness increases (i.e., the distance between the gold surface and Raman chromophore). Because the silica shell is microporous (i.e, pore sizes less than 2 nm), molecular diffusion through the silica shells toward the metal cores is prohibited on the basis of size and charge screening.[253] Instead, SERS signal intensities (I) should exhibit trends that approximately follow the equation:

$$I(T) = E\left(\frac{r+T}{r}\right)^{-10} = 80\left(\frac{6+T}{6}\right)^{-10} \qquad (3.1)$$

where E is the maximum theoretical signal enhancement for a gold nanosphere (~80),[254] r is the nanoparticle radius of curvature (6 nm), and T is the distance between the metal surface and Raman chromophore (i.e., silica shell thickness).

Deviations from this model are well-documented in the literature,[119, 140, 238] and is true for these data as well. While the general trend described by equation 3.1 is observed, the theoretical model underestimates the experimental findings, and

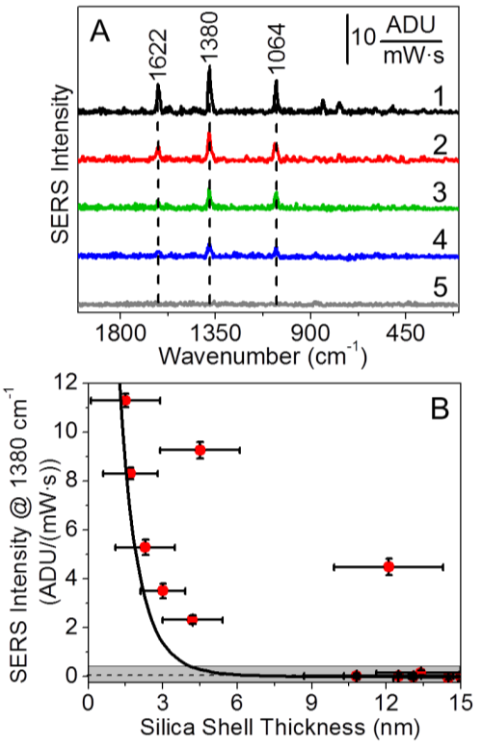

Figure 3.3 SERS analysis. (A) SERS spectra of 4 nM washed Au@SiO_2 nanoparticles encapsulated in T = (1) 1.7, (2) 2.3, (3) 3.0, (4) 4.2, and (5) 14.5 nm and incubated in 10 µM 2-naphthalenethiol in water for 1 hour. (B) SERS intensity for the 1380 cm^{-1} band of 2-naphthalenethiol as a function of silica shell thickness. Error bars represent statistical averages from at least 5 measurements, and average spectral noise is highlighted in gray. The solid line was calculated using equation 1. SERS parameters were: λ_{ex} = 632.8 nm, t_{int} = 60 s, and P = 2 mW.

inconsistencies in nanoparticles with similar silica shell thickness are observed (Figure 3.3B). For instance, two $Au@SiO_2$ nanoparticle samples were prepared with ~4.5 nm silica shell thicknesses. While both samples exhibited SERS activities, their average magnitudes are drastically different (2.1 to 9.1 $ADU \cdot mW^{-1} \cdot s^{-1}$). Surprisingly, these two samples exhibit similar plasmonic properties and morphology. These conflicting results indicate that these two nanoparticle samples exhibit structural differences or "defect" nanoparticle populations. As shown in Figures 3.1 and 3.2, evidence of surface defects on the $Au@SiO_2$ nanoparticles is present. If there were varying numbers of partially or uncoated gold nanoparticle cores in the samples, the inconsistent and somewhat-erratic ensemble-averaged SERS signal intensities could be rationalized.

3.3.3 Implications of Chromatographic Column Purification on $Au@SiO_2$ Nanoparticles Morphology and Stability

Because slight differences in preparation and/or storage methods can impact the resulting nanoparticle product, methods that improve the nanoparticle quality and purity post-synthesis are considered. LSPR spectral properties that depend on nanoparticle composition, size, shape, local dielectric environment, surface chemistry, and material stability[11] can be used to quantify and predict their function. Previously, changes in these parameters led to unexpected optical responses,[244, 245] thereby hindering solution-phase nanoparticle applications. To combat these limitations for solution-phase gold nanoparticles and to improve the uniformity of $Au@SiO_2$ nanoparticle shell, a surface chemistry quality control step is applied post-synthesis.

Hydrophobic interaction chromatography, a standard analytical technique typically used to purify small molecules using a hydrophobic resin, is used to improve the quality of $Au@SiO_2$ nanoparticles, post-synthesis. Bare and partially coated nanostructures should be retained by the chromatographic matrix because of their highly hydrophobic nature, while fully silica-coated gold nanospheres, which are less hydrophobic, should elute. To evaluate this hypothesis, a Sephadex-G50 column was packed (total volume = 2.7 mL, length = 5.0 cm) then rinsed with water to remove ethanol and to equilibrate the matrix (Figure 3.4A). Next, 2 mL of 15 nM $Au@SiO_2$ nanoparticle solution (in water) was added to the column dropwise (Figure 3.4B). Bare and partially coated nanoparticles adhere to the column matrix, allowing these unwanted materials to be successfully removed from the $Au@SiO_2$ nanoparticle solution. Finally, the "purified" and slightly diluted nanoparticle sample elutes from the column and is rinsed prior to analysis (Figure 3.4C).

After purification, the average nanoparticle diameter and silica shell thickness on the gold nanospheres were evaluated using TEM and compared to those before column purification. Representative TEM images of silica coated gold nanospheres after column purification are shown in Figure 3.5A-D. Importantly, the hydrophobic interaction column does not induce nanoparticles aggregation or morphology changes for silica-coated gold nanostructures. In comparison to these same nanoparticle samples before column purification (Figure 3.1), the average silica shell thickness increases slightly by 0 – 0.1 nm. As shown in Figure 3.5, the average silica shell thicknesses after and before (in parentheses) column purification are: 1.8 ± 1.0 (1.7 ± 1.1), 2.4 ± 1.1 (2.3 ± 1.2), 4.3 ± 1.4 (4.2 ± 1.2), and 14.5 ± 2.7 (14.5 ± 2.2) nm. A t-

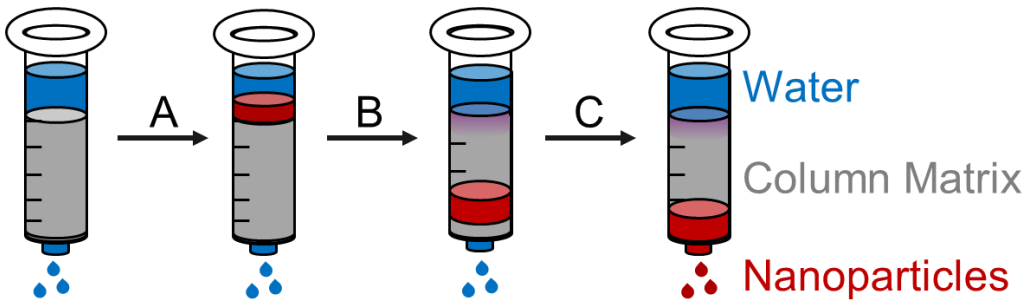

Figure 3.4 Schematic of hydrophobic interaction chromatography purification steps of Au@SiO_2 nanoparticles: (A) column equilibration, (B) Au@SiO_2 nanoparticle loading, and (C) nanoparticle elution and recovery.

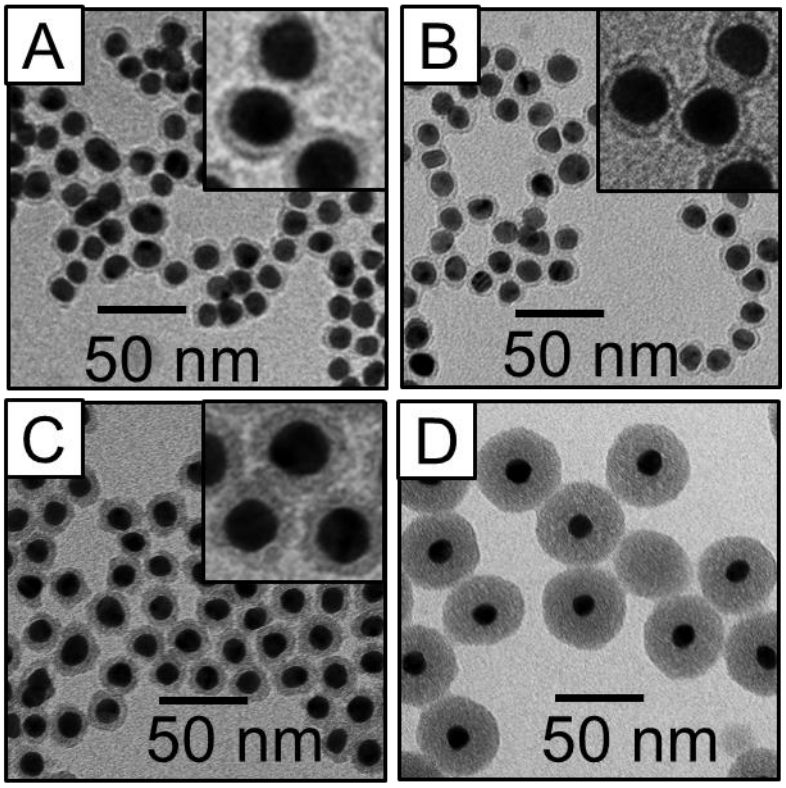

Figure 3.5 Representative TEM images of Au nanoparticles (d = 12.0 ± 1.3 nm) encapsulated in silica shells with thicknesses (T) of (A) 1.8 ± 1.0 nm, (B) 2.4 ± 1.1 nm, (C) 4.3 ± 1.4 nm, and (D) 14.5± 2.7 nm after column purification. The 100 nm x 100 nm insets in panels A-C reveal no evidence of silica shell defects.

test was performed to evaluate statistical differences between silica shell thicknesses before and after column purification. For nanoparticles stabilized in more than a 4.5 nm thick silica shells, no significant difference (to a 95% confidence level) in silica shell thickness is observed. The ~0.1 nm increase in silica shell thickness observed for all other samples likely arises from the removal of a small population of bare and partially coated nanostructures from solution via column purification (i.e., the relatively smaller, defect-containing nanoparticles were removed and the average nanoparticle size distribution increased).

As with the traditionally washed nanoparticles, the optical stability of these solution-phase nanoparticles is evaluated using LSPR spectroscopy. LSPR spectra for $Au@SiO_2$ nanoparticles (T = 1.8 nm) incubated in 100 mM NaCl are summarized in Figure 3.6. Before salt addition, the extinction maximum wavelength is centered at 531.7 nm (Figure 3.6A). This value exhibits a 14.1 nm red-shift after being mixed and incubated in salt for 1 hour (Figure 3.6B). Similar to the centrifuged/washed nanoparticle sample, normalized flocculated area increases (to 2.6). In contrast to the first sample, sample agitation easily facilitates the redispersion of the nanoparticles back into solution. As shown in Figure 3.6C, the LSPR spectral properties of the nanoparticle sample after a 12 hour incubation period and stirring results in optical properties similar to that of the sample prior to salt addition. Importantly, the solution still retains a red color for at least 3 months, thereby further supporting an electromagnetically stable nanoparticle sample (Figure 3.6 inset), in contrast to the traditionally washed nanoparticle sample shown in Figure 3.2 inset.

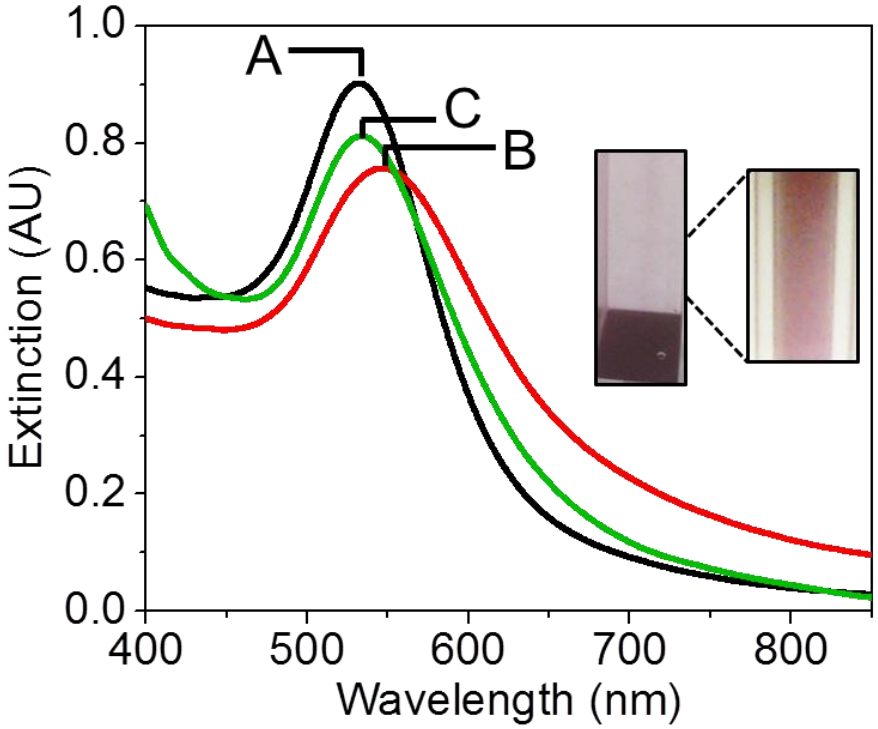

Figure 3.6 LSPR spectra for 4 nM hydrophobic interaction chromatography purified Au@SiO_2 nanoparticles (T = 1.8 nm) incubated with 100 mM NaCl for (A) 0 (λ_{max} = 531.7 nm, $A_{650\text{-}850}$ = 1.0), (B) 1 (λ_{max} = 545.8 nm, $A_{650\text{-}850}$ = 2.6), and (C) 12 (λ_{max} = 533.1 nm, $A_{650\text{-}850}$ = 1.2) hours (sample was vortexed). The photographs reveal a red-colored solution after 12 hours, thereby indicating no significant nanoparticle aggregation. Conditions are identical to those in Figure 3.2.

3.3.4 Chromatographic Purification Effect on the Electromagnetic Distance-Dependent SERS Model

If the LSPR integrity of the nanoparticle sample improves upon column purification using hydrophobic interaction chromatography, then the SERS activity of these nanostructures should differ from that of the initially prepared materials. To evaluate the effect of hydrophobic interaction chromatography on the SERS effect, 10 μM 2-naphthalenethiol was incubated with 4 nM Au@SiO_2 nanoparticles with varying silica shell thicknesses for 1 hour. Representative SERS spectra are shown in Figure 3.7A. Importantly, solution and measurement conditions are identical to those used with nanoparticle samples that were washed using centrifugation techniques.

Surprisingly, no SERS signals are observed for all Au@SiO_2 nanoparticle samples with shell thicknesses greater than 2 nm (Figure 3.7B). The only SERS-activity observed after passing the sample through the hydrophobic column is for the Au@SiO_2 nanoparticle sample stabilized in 1.6 and 1.8 nm thick silica shells. However, the formation of thinner, yet complete, silica shells are difficult to prepare. The SERS activity from Au@SiO_2 nanoparticles (T = 1.8 nm) before and after hydrophobic purification drops from 8.3 to 6.4 $ADU \cdot mW^{-1} \cdot sec^{-1}$ for 2-naphthalenethiol (Figure 3.3A-1 vs. Figure 3.7A-1). This 22% loss in SERS signal is hypothesized to arise from the removal of bare and/or partially coated gold nanoparticles in the column-purified samples, which arose from nanoparticle synthesis or during storage.

The SERS signals observed from chromatographic column purified gold nanospheres are less intense than when using traditionally prepared samples

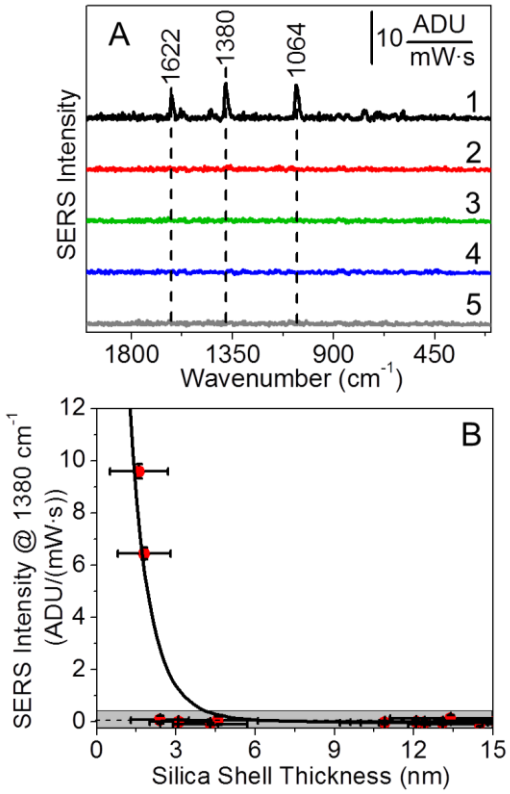

Figure 3.7 SERS analysis. (A) SERS spectra of 4 nM column-purified Au@SiO_2 nanoparticles encapsulated in T = (1) 1.8, (2) 2.4, (3) 3.1, (4) 4.3, and (5) 14.5 nm after incubated in 10 µM 2-naphthalenethiol in water for 1 hour. (B) SERS intensity for the 1380 cm^{-1} band of 2-naphthalenethiol as a function of silica shell thickness. Error bars represent statistical averages from at least 5 measurements, and average spectral noise is highlighted in gray. The solid line was calculated using equation 1. Conditions are identical to those in Figure 3.3.

(centrifugation only). This behavior can be attributed to the following: (1) electromagnetic coupling between metal nanoparticle cores is prohibited by the robust silica shells, which limits SERS enhancement; (2) SERS signals are known to decrease as the distance between the analyte and metal surface increases; and (3) short-range, charge-transfer interactions between the analyte and metal surface are prohibited by the complete silica shells (T > 2 nm). As a result, SERS signals from the Raman chromophore are only observed for 12 nm gold nanoparticles stabilized in less than 2 nm thick silica shells.

3.4 Conclusion

In conclusion, Au@SiO_2 nanospheres were prepared with varying silica shell thicknesses and purified using traditional centrifugation, as well as steps with and without subsequent hydrophobic interaction chromatographic purification. Upon passing the nanoparticles through the column, bare gold and partially silica-coated gold nanostructures were retained on the column, while fully coated nanostructures were eluted and subsequently characterized. As a result of the extra purification step, SERS activity closely followed an electromagnetic distance-dependence model, and inconsistencies from sample-to-sample synthetic variations were eliminated. This simple chromatographic purification step added a surface chemistry quality control measure to nanoparticle preparation, which could be extended to other solution-phase nanoparticles for more predictable function in a variety of future applications such as molecular sensor and/or detection.

CHAPTER IV

DEVELOPMENT OF A MORE ROBUST APPROACH FOR DESCRIBING INTERNAL ETCHING OF SILICA SURROUNDING GOLD NANOSPHERES

4.1 Introduction

Surface-enhanced Raman scattering (SERS) is a valuable technique in biology and chemistry because the detection of small molecules can be performed sensitively and without labels.[11, 94] Both normal Raman spectroscopy and SERS provide unique fingerprints of molecules, which depend on chemical and structural information. Although both methods provide similar information about a molecule, the signal observed from SERS is up to 9 orders of magnitude larger than that in a normal Raman spectrum. This enhancement depends on the direct interaction between the Raman-active chromophore and the metal nanoparticle surface, as well as the plasmonic properties of the metal nanoparticle.[61, 94, 115-117]

As described in Chapter 2, spectral intensities can vary dramatically when solution-phase metal nanoparticles are used as SERS substrates.[156, 161, 162] When an analyte is added to a solution, the nanoparticles can undergo uncontrolled aggregation, which induces changes in their localized surface plasmon resonance (LSPR) properties.[4, 255] LSPR is an optical phenomenon[18, 20, 22, 34, 156] that is observed when a metal nanoparticle smaller than the wavelength of light interacts with electromagnetic radiation.[25, 27, 28, 65, 66] Certain radiation wavelengths can be selectively absorbed and scattered by the nanoparticle, which causes the conduction electrons in the metal nanostructures to oscillate collectively.[25, 37, 65-67] Consequently, a strong extinction (i.e., sum of absorption and scattering)

spectrum arises,[11, 26, 28, 67] which depends on the nanoparticle size, shape, and local dielectric medium.[18, 49, 223, 256-272]

Because the LSPR spectrum of solution-phase nanoparticles depends on the local dielectric medium, and methods that prevent aggregation and undesired dielectric medium changes are necessary. For instance, metal nanostructures have been protected with robust materials, including microporous silica shells (with pore sizes < 2 nm) to form core@shell nanomaterials.[273] The silica shell prevented electromagnetic coupling between the metal cores, but the use of these silica-coated metal nanoparticles in SERS assays is limited. Because, the silica shell dictates the distance between the molecule and the metal surface, and SERS signals decrease rapidly as the silica shell thickness increases (as discussed in Chapter 3).[174, 176]

To facilitate the use of metal@shell nanostructures in SERS applications, several research groups[4, 161] have synthesized internally etched metal@shell nanoparticles to promote molecular diffusion while maintaining the electromagnetic stability of the metal cores.[178, 274-278] For example, the formation of internally etched Au@SiO_2 nanospheres can occur in basic conditions, and etching was reported as a function of etching time. Because the etching reaction depends on many parameters, including solution agitation and temperature, as well as silica cross-linking and thickness, the time required to produce a reproducible degree of silica etching can vary from day to day and sample to sample (*vide infra*).

In this chapter, shifts in the LSPR wavelength of internally etched silica-coated gold nanoparticles are shown to be a more reliable measure of silica etching vs. etching time. Internally etched Au@SiO_2 nanostructures were synthesized using

LSPR wavelength shifts that relate to the local refractive index surrounding the gold cores. The refractive index sensitivity of the gold nanoparticles (m), the refractive index (RI) of the silica shell, and the characteristic electromagnetic field decay length (l_d) of the metal cores were estimated using a previously reported model.[279] Preliminary data indicate that, as the extinction maximum wavelength blue-shifts and LSPR wavelength shifts are observed, SERS intensities for 4-aminobenzenethiol increase. The blue-shifts in the LSPR spectra suggest that the local dielectric environment surrounding the metals is decreasing as the silica near the metal core is replaced by a lower refractive index medium (water, silica, and/or 4-aminobenzenethiol). Future studies will be performed that systematically correlate structural and spectroscopic data to semi-empirical LSPR models. The findings should result in more predictable materials design strategies and quantitative SERS detection platforms for small molecule detection.

4.2 Experimental Methods

4.2.1 Materials

Gold (III) chloride trihydrate, sodium citrate dihydrate, Amberlite MB-150 mixed bed exchange resin, (3-aminopropyl) trimethoxysilane (APTMS), sodium chloride (NaCl), sodium trisilicate (27%), 4-aminobenzenethiol (4-ABT), and tetraethyl orthosilicate (TEOS) were purchased from Sigma (St. Louis, MO). Ethanol, ammonium hydroxide (NH_4OH), hydrochloric acid (HCl), and nitric acid (HNO_3) were purchased from Fisher Scientific (Pittsburgh, PA). Ultrapure water (18.2 $M\Omega \cdot cm^{-1}$) was obtained from a Barnstead Nanopure System (Dubuque, IA) and used for all experiments. For all experiments, glassware was cleaned with aqua regia (3:1

HCl/HNO_3), rinsed thoroughly with water, and oven (glass) or air (plastic) dried overnight before use.

4.2.2 Internally Etched Silica-Coated Gold Nanoparticle Synthesis

Internally etched silica-coated gold (IE $Au@SiO_2$) nanospheres were synthesized in three steps. First, gold (Au) nanospheres were synthesized using the standard citrate reduction method.[4, 156, 161, 213] Second, gold nanoparticles were silica-coated as previously reported.[4, 161, 167, 174, 237] Third, IE $Au@SiO_2$ nanospheres were synthesized by increasing the pH of the aqueous solution via the addition of concentrated NH_4OH.[4, 161] Briefly, the pH of the $Au@SiO_2$ nanoparticle solution was increased to 11.0 by the addition of concentrated NH_4OH to promote dissolution of the internal, low crossed-linked silica near the gold nanoparticle surface. During the etching process, the concentrations of $Au@SiO_2$ nanoparticles and NH_4OH were 4.5 nM and ~1.5 M, respectively. Next, the solution was decreased to a pH of 4.0 using 100 mM HNO_3. This acidification step stops the etching process by reducing the rate of silica dissolution. IE $Au@SiO_2$ nanoparticle solutions were then purified using a packed Sephadex-G50 column (a slurry composed of a hydrophobic dextran gel).[174] The uncoated and/or partially coated gold nanoparticles were retained by the column matrix via hydrophobic interactions, while the less hydrophobic, fully silica-coated IE $Au@SiO_2$ nanoparticles eluted from the column and were collected for subsequent use. The concentration of the Au nanospheres in solution was estimated via extinction spectroscopy (using an extinction coefficient of 13 nm bare gold nanoparticles ($\varepsilon_{520nm} = 2 \times 10^8\ M^{-1} \cdot cm^{-1}$) using the approach reported by Haiss *et al*.[214]

4.2.3 Transmission Electron Microscopy (TEM)

TEM images were collected using a JEOL JEM-1230 microscope equipped with a Gatan CCD camera. Samples were prepared on 400 mesh copper grids coated with a thin film of Formvar and carbon (Ted Pella, Inc.). The nanoparticle solution (~50 μL) was pipetted onto the grid and promptly drained using filter paper. The mean diameter (d) of the nanospheres was determined from these data using Image Pro Analyzer 6.1 (Media-Cybernetics). At least 100 nanoparticles were analyzed for each nanoparticle sample.

4.2.4 Extinction Spectroscopy and LSPR Wavelength Shift Modeling

LSPR spectra were collected using a 1.0 cm path length disposable methacrylate cuvette and an ultraviolet-visible (UV-vis) spectrometer (Ocean Optics USB4000). To monitor the silica dissolution process, the samples were diluted in water to a final concentration of 4.5 nM IE Au@SiO_2 nanoparticles, and the pH was adjusted to 11.0 using concentrated NH_4OH. Upon the addition of base to the nanoparticle solution, the sample was mixed using a pipette, and LSPR spectra were collected every 30 seconds for 1 hour. The following parameters were used during data collections: integration time = 30 msec, average = 25 scans, and boxcar = 10. Spectral smoothing was performed using a 50 point adjacent averaging method, and the extinction maximum wavelengths (λ_{max}) were determined from the zero-point crossing of the first derivative of each spectrum using MatLab R2013a (MathWorks).

In order to track more accurately silica dissolution (rather than etching time), shifts in the extinction maximum wavelength ($\Delta\lambda_{max}$) were used to estimate changes in the local refractive index near the gold nanoparticle cores. To understand these

spectral trends, the refractive index sensitivity (m) of the gold cores was estimated by incubating 3.5 nM citrate stabilized gold nanospheres in 0 – 85 % (w/v) sucrose solutions to change the refractive index of the bulk solution from 1.33_3 to 1.50_4.[280-282] Extinction spectra were collected for each sample after a 50 minute incubation time, and the extinction maximum wavelength was determined for each sample using Mathcad 2001 Professional (Product & Service Advantage). The λ_{max} values were then plotted as a function of known sucrose refractive indices.[256, 266, 283-287]

Next, the refractive index of the silica shells and the characteristic electromagnetic field decay length of the gold cores were estimated using gold nanospheres coated with 3.0, 4.2, and 14.8 nm silica shells. The materials were incubated in the same sucrose concentrations described above, and the λ_{max} obtained from each silica-coated gold nanoparticle sample was plotted as a function of the known sucrose refractive indices.

To estimate these parameters, a fitting function is needed to fit all the data above, where d_{silica} = 0, 3.0, 4.2, 14.8 nm. According to Campbell, the λ_{max} shift to changes in the bulk refractive index can be approximated as a linear function over a narrow range when the metal surface contains no adsorbed, and the equation is as follows:[51, 279]

$$\Delta\lambda_{max} = \lambda_{max,bulk} - \lambda_{max,water} = m(n_{eff} - n_{water}) \qquad (4.1)$$

where $\Delta\lambda_{max}$ is the LSPR wavelength shift response from the nanospheres in 0 to 85 % (w/v) sucrose, m is the refractive index sensitivity of Au nanoparticles, n_{eff} is the effective refractive index of the bilayer structure shown in Figure 4.1 (layer 1 = silica and layer 2 = bulk solution), n_{water} is the refractive index of the bulk solution at 0 %

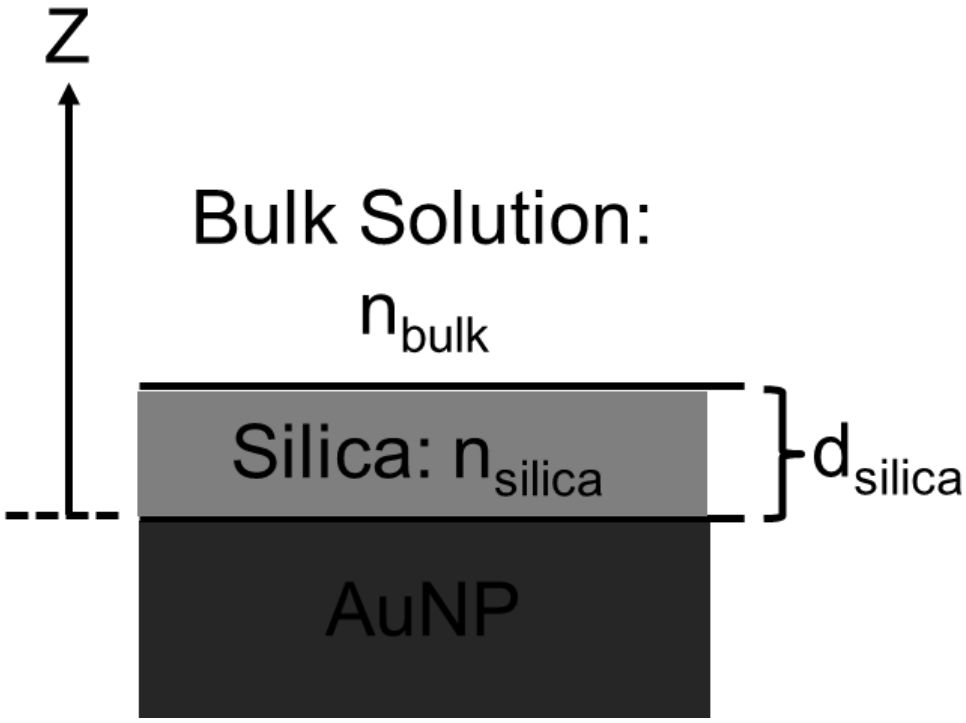

Figure 4.1 Schematic block diagram of a bilayer structure, that contains a silica layer coated directly on the gold metal nanoparticle of refractive index n_{silica} and thickness d_{silica}. Above the silica layer is the bulk solution of refractive index n_{bulk}. The Z-axis label from the surface of the Au nanosphere where z = 0 passes z = d_{silica} at the silica surface, though the bulk solution to infinity z = ∞.

(w/v) sucrose (water 1.33_3). The refractive index sensitivity factor could have been estimated by simple division: $m = \Delta\lambda_{max}/\Delta n$; however, the calibration curve obtained for SPR response *vs.* bulk refractive index was not linear. To account for the curvature observed in the calibration curve, a low-order polynomial equation was formed by adding a second term "$m_2(n_{eff} - n_{water})^2$" to Equation 4.1 above, which becomes:[279]

$$\Delta\lambda_{\max} = \lambda_{\max,bulk} - \lambda_{\max,water} = m_1(n_{eff} - n_{water}) + m_2(n_{eff} - n_{water})^2 \qquad (4.2)$$

The effective refractive index of the bilayer structure in Figure 4.1 is obtained by integrating the distance-dependent local refractive index (n(z)) times the square of the local electromagnetic field (E(z)) from zero to infinity:[51, 279]

$$n_{eff} = \frac{2}{l_d}\int_0^\infty n(z)E^2(z)dz \qquad (4.3)$$

$$where \quad n(z) = \begin{cases} n_{silica}, 0 \le z \le d_{silica} \\ n_{bulk}, d_{silica} \le z \le \infty \end{cases} \quad and \quad E(z) = \exp(-z/l_d)$$

After carrying out the integration in Equation 4.3 using the bilayer structure (Figure 4.1) to determine the effective refractive index, n_{eff} was substituted in Equation 4.2 to form Equation 4.4, which is the function that is used to estimate the refractive index sensitivity, the characteristic decay length, and the refractive index of the silica:

$$\lambda_{max,silica} = \begin{array}{l} m_1[(n_{silica} + (n_{bulk} - n_{silica})\exp(-2d_{silica}/l_d) - n_{water}] + \\ m_2[(n_{silica} + (n_{bulk} - n_{silica})\exp(-2d_{silica}/l_d) - n_{water}]^2 + \lambda_{\max,water} \end{array} \qquad (4.4)$$

4.2.5 SERS Spectroscopy

SERS signals were monitored ~0.1 cm from the base of the sample vial using an Advantage Raman spectrometer (Delta Nu). The following parameters were used:

excitation wavelength (λ_{ex}) = 632.8 nm, integration time (t_{int}) = 60 s, and laser power (P) = 2 mW. Each sample contained 4 nM IE Au@SiO_2 nanoparticles and 10 μM 4-aminobezenethiol (4-ABT) (final concentrations). A stock solution of 4-ABT (50 μM) was prepared in water by diluting the 5 mM stock solution in ethanol. Upon the addition of 4-ABT to the nanoparticles, the mixture was vortexed for 5 seconds, and SERS spectra were collected every 60 seconds for 1 hour. All spectra were background-corrected using a control sample that contained only nanoparticles (no 4-ABT). Noise was estimated using the standard deviation of the baseline from 1900–1700 cm^{-1}. Only spectral intensities greater than 3 times the noise were evaluated.

4.3 Results and Discussion

4.3.1 Experimental Determination of the Refractive Index Sensitivity of the Gold Nanoparticles, Silica Shell Refractive Index, and the Characteristic Electromagnetic Field Decay Length

The LSPR wavelength of gold nanostructures depends on the local refractive index of the surrounding environment.[26-28, 156] Change in the local dielectric medium will shift the LSPR predictably; therefore, shifts in the extinction maximum wavelength ($\Delta\lambda_{max}$) of metal nanoparticles can be used to experimentally determine the refractive index sensitivity of the gold nanoparticles to changes in local dielectric environment and the characteristic electromagnetic field decay length associated with the metal nanoparticles. Furthermore, information regarding the refractive index of surface layers can be estimated if structural information is known.

To do this, a LSPR model that relates the wavelength shifts with the refractive index of the gold core surrounding medium is required. Jung *et al*. first developed a

model for planar surface plasmon resonance experiments in 1998.[279] Haes *et al*. adapted this model for use in LSPR spectroscopy in 2002;[288] such model is reported in Equation 4.4.

To determine these important material characteristics, 3.5 nM Au, Au@SiO_2 coated with a 3.0 nm shell, Au@SiO_2 nanoparticles encapsulated in a 4.2 nm silica shell, and Au@SiO_2 nanoparticles encapsulated in a 14.8 nm silica shell were incubated in sucrose concentrations ranging from 0 – 85 %. Each sample was allowed to equilibrate for 50 minutes before LSPR measurements were collected.

Both qualitative and quantitative differences are observed between LSPR spectra collected at various sucrose concentrations, as well as with different local environments (absence and varying silica shell thicknesses). For instance, Figures 4.2A and 4.2B show the LSPR spectra for Au and Au@SiO_2 nanoparticles encapsulated with the 3.0 nm silica shell after being incubated in (1) 0 %, (2) 20 %, (3) 40 %, (4) 60 %, and (5) 80 % (w/v) sucrose, respectively. The extinction for Au nanospheres in sucrose increases by ~200 mAU from 0 to 80 % (w/v) (1.33_3 - 1.49_1);[289-291] whereas, Au@SiO_2 encapsulated with the 3.0 nm SiO_2 only increases by ~80 mAU. Because extinction increases with increasing dielectric environments, a greater change in extinction is expected for Au nanospheres vs. silica coated Au nanospheres. The overall wavelength shifts ($\lambda_{max,85\%}$ - $\lambda_{max,0\%}$) for both samples increase with increasing sucrose concentration. The λ_{max} for the gold nanospheres shift +8.4 nm vs. only +3.8 nm for the silica-coated gold nanoparticle sample. These results can be attributed to local refractive index changes near the gold core, which increased from 1.33_3 in water to 1.50_4 in 85 % (w/v) sucrose.[289-291]

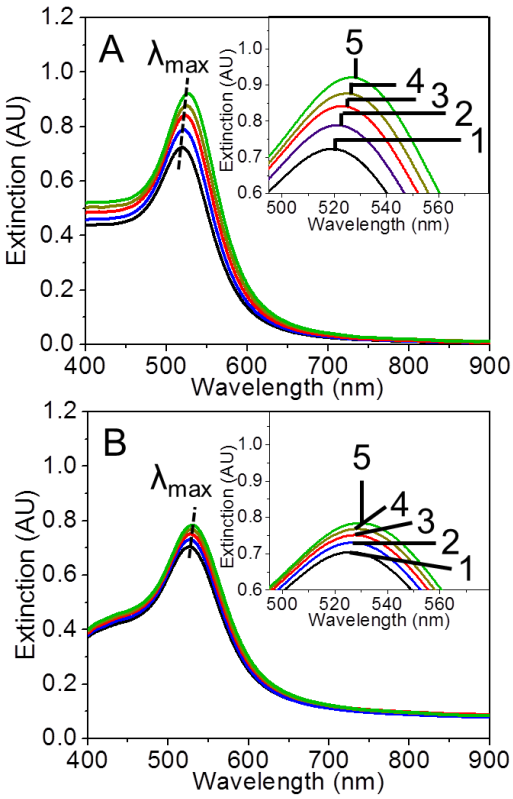

Figure 4.2 LSPR spectra for 3.5 nM (A) citrate stabilized Au and (B) Au@SiO_2 nanoparticles encapsulated by 3 nm silica shells after incubating in 0 – 80 % (w/v) sucrose for 50 minutes. The extinction maximum wavelength (λ_{max}) is marked by a dash line and red-shifts with increasing bulk refractive index. The inset magnifies spectra for Au and Au@SiO_2 nanospheres incubated in (1) 0, (2) 20, (3) 40, (4) 60, and (5) 80 % (w/v) sucrose. The shifts in the λ_{max} ($\lambda_{max80} - \lambda_{max0}$) for Au and Au@$SiO_2$ nanoparticles encapsulated in 3 nm silica shells are +8.4 and +3.8 nm, respectively. The extinction for Au nanospheres in sucrose increases by 0.197 from 0 to 80 % (w/v) while Au@SiO_2 coated with 3.0 nm SiO_2 only increases by 0.080 which is about 40 % extinction increased in comparison to bare gold nanoparticles.

To determine the refractive index sensitivity of the metal cores to local dielectric changes, λ_{max} and $\Delta\lambda_{max}$ obtained from the LSPR spectra are plotted as a function of both known refractive index and concentration of sucrose in Figure 4.3. All data sets are fit using a polynomial parabola function. Both m_1 and m_2 are determined, where m_2 is the refractive index sensitivity (m) for the sample, which is 55.7 (Figure 4.3A), 38.8 (Figure 4.3B), 7.8 (Figure 4.3C), and -11.8 nm (Figure 4.3D). This value decreases as the silica shell thickness increases as more silica occupies the sensing volume near the metal surface.[288] The refractive index sensitivity of bare Au nanospheres (55.7 nm) was used for further analysis.

Next, the refractive index of unetched silica can be directly estimated for all three silica-coated samples from Figure 4.3. The refractive index of the condensed silica shell is reported to the be the intersection at which silica-coated nanoparticles sample line cross the citrate stabilized gold nanospheres line.[288] As shown in Figure 4.3, these refractive index of the silica shell are 1.51_3 (3.0 nm shell), 1.48_6 (4.2 nm shell), and 1.44_1 (14.8 nm shell), respectively. Assuming that the refractive index of (unetched) silica condensed on the gold nanoparticles is constant with increasing silica shell thickness, an average refractive index value is then calculated from Au@SiO_2 nanospheres silica-coated with 3.0 and 4.2 nm shell. The resulting number is 1.500 ± 0.019 which is reasonable in comparison to the range of refractive index reported (1.45–1.55) for amorphous silica.[167, 273, 292-295] Refractive index decreases with increasing silica shell thickness because the bulk solution dielectric constant does not affect the optical properties of the metal core. Au@SiO_2 nanospheres encapsulated in 14.8 nm silica shell data did not include in the estimation

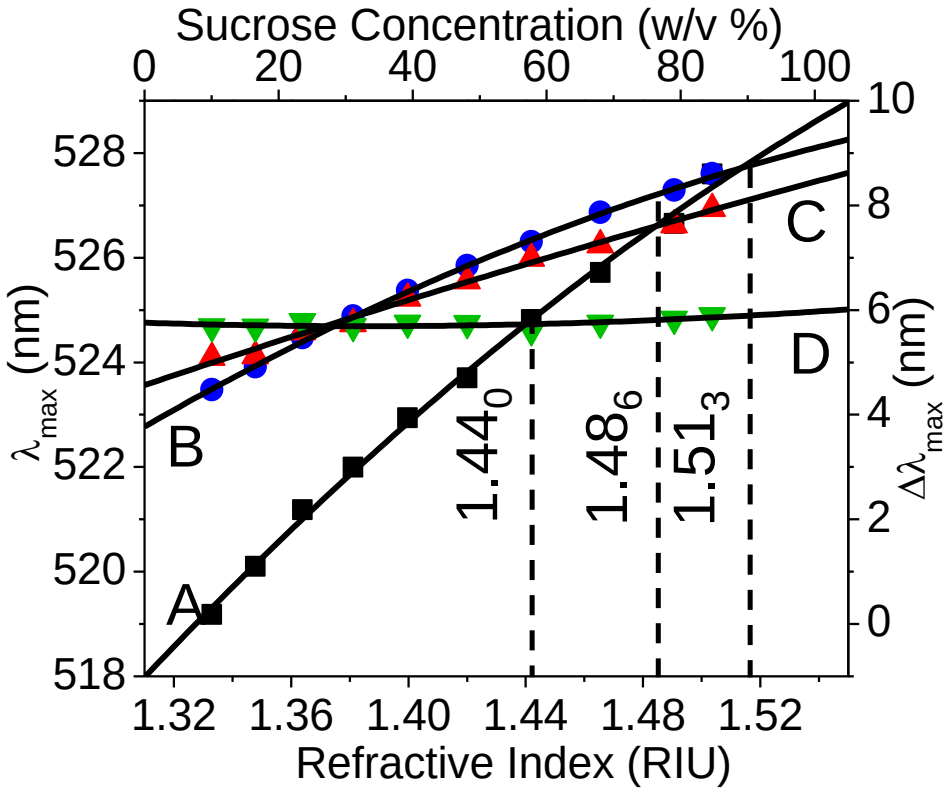

Figure 4.3 Extinction maximum wavelength and LSPR wavelength shift for (A) Au nanoparticles, (B) Au@SiO_2 nanospheres encapsulated with 3.0 nm SiO_2 , (C) 4.2 nm SiO_2, and (D) 14.8 nm SiO_2 as a function of known bulk refractive index. The data are fit using a polynomial curve, and the refractive index sensitivity of the gold core from all nanoparticle samples is $55._7$, $38._8$, $7._7$, and $-11._8$ nm, respectively. The refractive index of the condensed silica can be estimated by averaging the refractive index at the intersection for all silica-coated lines, except Au@SiO_2 nanospheres coated with 14.8 nm SiO_2. The refractive index of the condense silica shell is 1.50_0.

of the silica refractive index because no significant change was observed in the LSPR wavelength as a function of sucrose concentration, indicating that the change in refractive index for this sample is 0. The extinction wavelength did not change for this sample because the silica shell is too thick and occupied the sensing volume near the gold core.

Finally, to calculate the characteristic electromagnetic field decay length (l_d) for the gold nanoparticles, these same data and Equation 4.4 are used. A decay length is estimated for each silica-coated sample, which is 2.3, 7.4, and 7.9 nm for Au@SiO_2 nanospheres encapsulated with 3.0, 4.2, and 14.8 nm silica shells, respectively. Because the extinction maximum wavelength of Au@SiO_2 nanospheres coated with 14.8 nm silica shell remains unchanged in various sucrose concentrations, the characteristic electromagnetic field decay length of the gold nanospheres is 4.9 nm an average number calculated from the two other silica coated samples. Previous theoretical results predicted a characteristic electromagnetic field decay length between 5 to 30 nm.[296-298] As a result, the model provides a reasonable estimation to describe these nanomaterials for etching experiments.

4.3.2 Structural and Optical Analysis of Multiple IE Au@SiO_2 Nanoparticle Samples after a 25 Minutes Etching Period

Two independent syntheses of IE Au@SiO_2 nanospheres were prepared to evaluate both the reproducibility of silica condensation and subsequent dissolution. First, silica condensation on the surface of gold nanospheres occurred via a modified Stöber method.[167, 174] Next, the Au@SiO_2 nanoparticles were diluted to 4.5 nM and the solution pH was increased to 11.0 using concentrated NH_4OH (final

concentration ~1.5 M). This etching reaction took place at room temperature (~70 ˚F) and without stirring. After 25 minutes, the etching reaction was stopped by acidifying the solution to pH 4 using 0.1 M HNO_3.[4, 161] Next, the resulting nanostructures were purified via chromatography column prior to use, in order to remove partially and/or uncoated silica particles.[161, 174]

Representative TEM images for each of the two independently synthesized IE Au@SiO_2 nanoparticle samples are shown in Figure 4.4. Several observations can be made from image analysis. First, the diameter and particle counts of the composite particles are 44.3 ± 3.5 nm from 430 particles (Figure 4.4A) and 42.2 ± 4.9 nm from 115 particles (Figure 4.4B). This result suggests that silica condensed uniformly in both samples. Next, the degree of internal silica dissolution observed is inconsistent in each sample, even though neutralization was constant when the three nanoparticle samples were internally etched. For instance, Figure 4.4A shows a more uniform degree of internal silica etching from nanoparticle to nanoparticle; whereas; Figure 4.4B shows a more heterogeneous sample.

The image contrast within a nanoparticle decreases from the gold core to etched silica (internal) in comparison to the background. The change in the image contrast is observed because each material (silica and gold) has a different electron density. For all materials, including silica, image contrast varies with material density. As internal silica etching increases, the silica matrix becomes less dense, causing the contrast of the etched silica to be more similar to the background; whereas, the silica membrane, which is denser, remains darker. These data suggest that silica dissolution occurred

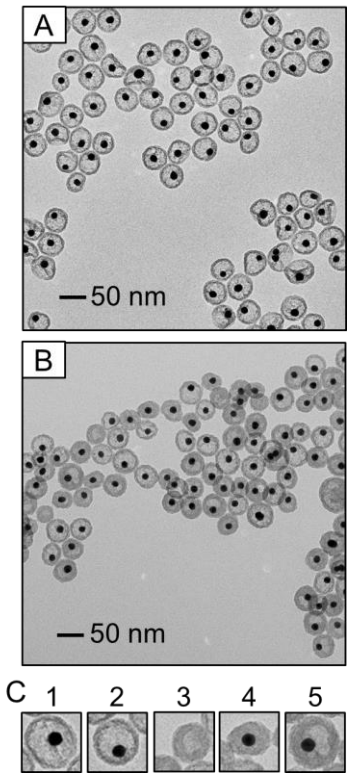

Figure 4.4 (A & B) Representative TEM images of two IE Au@SiO_2 nanoparticle samples neutralized after 25 minutes etching. The total average mean diameters (d = ~44 nm) are similar for both samples. The degree of internal silica dissolution varies from sample to sample. (C) TEM micrograph of 56 nm by 56 nm single nanoparticle illustrates 5 of the extreme variations in the internal silica dissolution: (1) gold is in the center of the nanoparticle; (2) gold core is in the edge inside the silica membrane; (3) no gold core present, but internal silica etching; (4) no significant internal silica dissolution is observed; and (5) a packet of internal silica etching is observed on only one side of the gold core.

primarily in the internal silica layer located at the surface of the gold nanoparticles.[4, 161]

Another example of the heterogeneity observed in the contrast within nanoparticles is shown in Figure 4.4C. Figure 4.4C-1 shows that the gold core is in the center, while the gold core is observed at the edge inside the silica membrane in Figure 4.4C-2. Furthermore, a dense silica line that passes through the nanoparticle is observed in Figure 4.4C-1, which is the reason that the gold core is observed in the center. This result demonstrates that the internal silica is not fully dissolved. Figure 4.4C-3, on the other hand, contains no gold core; yet internal silica dissolution is observed. This observation indicates that internal silica etching does not depend on the presence of the gold core, but rather on the cross-linking of the silica layer on the gold surface when compared to the external silica layer. No sign of internal silica etching is observed in Figure 4.4C-4; whereas, in Figure 4.4C-5, there is a packet of light etching on one side of the gold core. These results illustrate that the rate of etching varies from nanoparticle to nanoparticle within a sample, as well as with incubation time. It also shows that etching does not occur radially. Additionally, the differences in image contrast in the "etched" regions of the nanomaterials indicate changes in the local refractive index surrounding the metal cores. In an effort to evaluate the local dielectric environment surrounding the nanoparticles, 45 parallel etching reactions were carried out using $Au@SiO_2$ nanoparticles, and LSPR spectra were collected every 30 seconds for 1 hour.

An example of the etching profile for one representative etching experiment is shown in Figure 4.5A, where the λ_{max} is plotted as a function of etching time. As

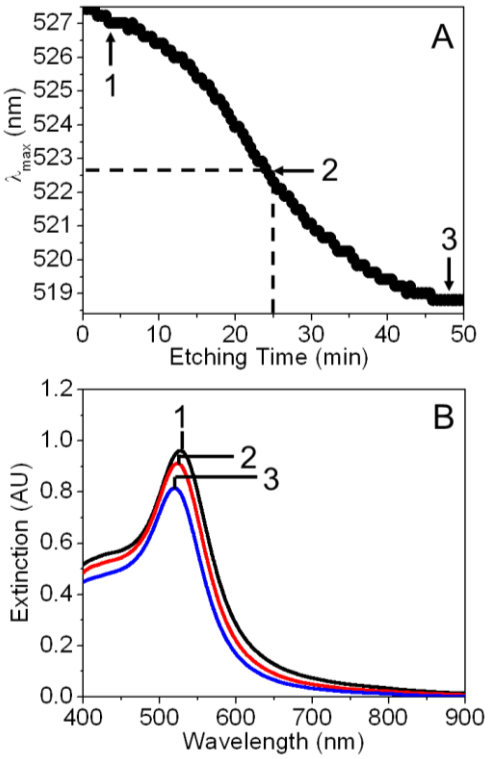

Figure 4.5 Monitoring silica etching during the fabrication of IE Au@SiO_2 nanoparticles: (A) an example of an etching profile as a function of etching time. The λ_{max} values were determined from the LSPR spectra. Etching was performed without stirring at room temperature (70˚F). (B) Extinction spectra for (1) unetched, (2) 25 min internally etched, and (3) silica membrane-etched Au@SiO_2 nanospheres during silica dissolution. The extinction maximum wavelengths (λ_{max}) of these samples centered at 527.4, 522.3, and 519.0 nm, respectively. The λ_{max} blue-shift as etching progresses because the refractive index surrounding the gold core decreases (silica to water).

previously observed,[161] the extinction maximum wavelength of unetched Au@SiO_2 nanoparticles (Figure 4.5A-1 and Figure 4.5B-1, λ_{max} = 527.4 nm) initially blue-shifted with increasing etching time as the local dielectric environment decreased (Figure 4.5A-2 and Figure 4.5B-2, λ_{max} = 522.3 nm). The extinction maximum wavelengths then reached a minimum, at which point silica etching was still occurring, but was not detectable using LSPR spectroscopy (Figure 4.5A-3 and Figure 4.5B-3, λ_{max} = 519.0 nm).

Significantly, the etching profile for all 45 samples followed similar qualitative trends; however, quantitative differences were observed. For instance, nanoparticles that were etched for 25 minutes possess a range of extinction maximum wavelengths (λ_{max}) from 519.6 to 524.4 nm with an average of 522.0 ± 1.5 nm (N = 45). Figure 4.6 shows that the λ_{max} values follow a one-tailed Gaussian model with a center of mass centered at 523.1± 0.7 nm.

Given the previously estimated refractive index sensitivity (55.7 nm) of the gold nanoparticles, a ± 1.5 nm shift in extinction maximum wavelengths would result when the local refractive index near the metal surface changes by ± 0.03. Slight variation in silica density and cross-linking lead to refractive index changes in the third decimal point. According to the CRC,[299] these optical data, combined with structural differences (TEM), indicate that etching time yields heterogeneously and inconsistently etched silica.

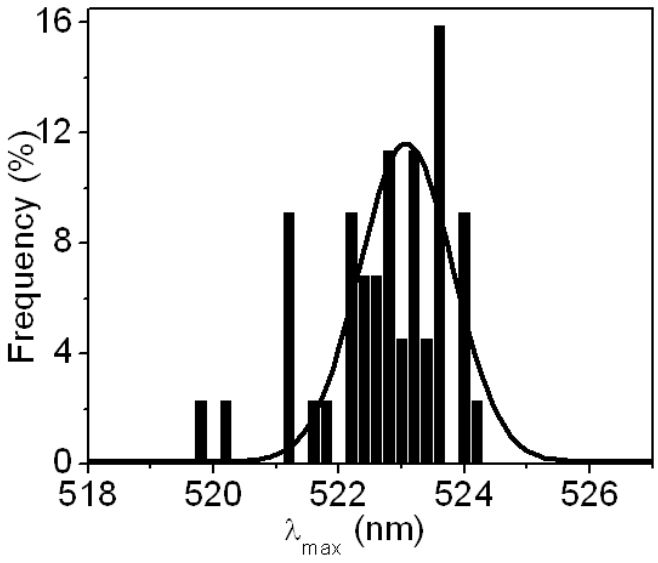

Figure 4.6 Histogram of the λ_{max} for 45 IE Au@SiO_2 nanoparticle samples after being etched for 25 minutes. The average value of the λ_{max} obtained from a Gaussian curve of the data is 523.1 ± 0.7 nm. Experimental conditions: 4.5 nM Au@SiO_2 nanoparticles, 1.5 M NH_4OH solution (etchant), and 100 mM HNO_3 solution (quencher).

4.3.3 Modeling and Using LSPR Wavelength Shifts to Describe the Internal Etching of Silica-Coated Gold Nanospheres

Because etching time yields significant differences in nanoparticle structure and because the refractive index sensitivity of the gold nanoparticles, the refractive index of the (unetched) silica shell encapsulating the gold nanoparticle cores, and the characteristic electromagnetic field decay length of the noble gold nanospheres can be estimated, shifts in LSPR wavelengths are expected to provide a more reliable description of particle morphology. The effective refractive index of the local environment can be estimated using a trilayer form of Equation 4.3 as follows:[51, 279, 300, 301]

$$n_{eff} = n_{etch} + (n_{silica} - n_{etch})\exp(-2d_{etch}/l_d) + (n_{bulk} - n_{silica})\exp(-2(d_{etch} + d_{silica})/l_d) \quad (4.5)$$

Following this equation, n_{eff} is substituted into Equation 4.2 to estimate the refractive index and the thickness of the etched space, which are labeled as n_{etch} and d_{etch} (internal), respectively. This is conducted using the following parameters: $\Delta\lambda_{max}$, the LSPR wavelength shift from before and after etching; m, the refractive index sensitivity (m_1 = 205.2 nm and m_2 = 55.7 nm) from bare gold nanoparticles; n_{silica} = 1.54_5, the refractive index of unetched silica; n_{bulk} = 1.33_3, the refractive index of the bulk medium, water; (d_{etch} + d_{silica}) = 14.8 nm, the total silica shell thickness prior to silica dissolution; and l_d = 5.9 nm, the characteristic decay length. While a small amount of silica is etched from the silica exterior, the dielectric medium is well beyond the electromagnetic field decay length and should not impact this model.

To evaluate this model, LSPR data were collected for 4.5 nM Au@SiO_2 nanoparticle solutions incubated in an etchant solution (1.5 M NH_4OH) for 1 hour.

LSPR wavelengths were monitored for the duration of the experiment using extinction spectroscopy, and shifted wavelengths were calculated using water as the initial dielectric medium. As previously reported, the λ_{max} blue-shifts as etching progresses and larger $\Delta\lambda_{max}$ are observed. Using the trilayer model from Equation 4.5, effective local refractive indexes can be estimated and should yield more uniformly etched silica shells and similar LSPR spectra.

To verify the reproducibility of this new procedure, several etching experiments were carried out using Au@SiO_2 nanoparticles with similar initial λ_{max} and silica shell thicknesses. Silica dissolution was stopped after the λ_{max} blue-shifted by ~6.0 nm. The LSPR wavelength was monitored during the etching via a UV-vis spectroscopy. Representative TEM images and LSPR spectra for 3 samples are shown in Figure 4.7. In contrast to the TEM images shown in Figure 4.1, which etched for the same period of time, the images shown in Figure 4.7A are uniformly etched from sample to sample. This is evident from similar silica contrast at the "inner" and "outer" silica locations. The average diameter and particle counts for each of the samples are 41.1 ± 3.4 nm from 105 particles, 41.6 ± 5.2 nm from 111 nanoparticles, and 41.2 ± 5.2 nm from 119 particles.

LSPR spectra provide more quantitative information regarding the local environment surrounding the metal surface. As shown in Figure 4.7B, extinction maximum wavelengths were centered at 520.1, 520.5, and 520.6 nm with $\Delta\lambda_{max}$ equal to -6.0, -5.6, and -5.5 nm, respectively. The differences in LSPR shifts likely arise from slight inconsistencies in how quickly silica dissolution was stopped. As a result,

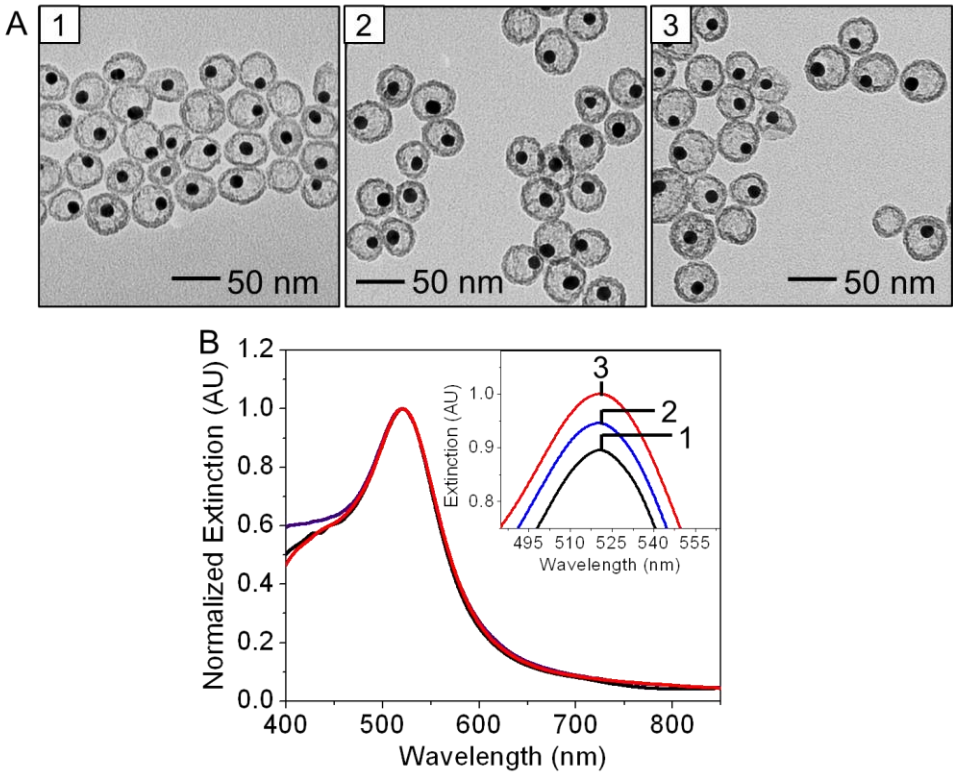

Figure 4.7 (A) Representative TEM images of three IE Au@SiO_2 nanoparticle samples fabricated under the same conditions with similar initial λ_{max} (~526 nm) and mean diameters (~40 nm). The degree of internal silica dissolution appears consistent from sample to sample. (B) Normalized LSPR spectra of 4 nM IE Au@SiO_2 nanospheres. All observed LSPR wavelengths are centered at ~520.4 nm. The variation measured from these samples is less than ± 1.0 nm.

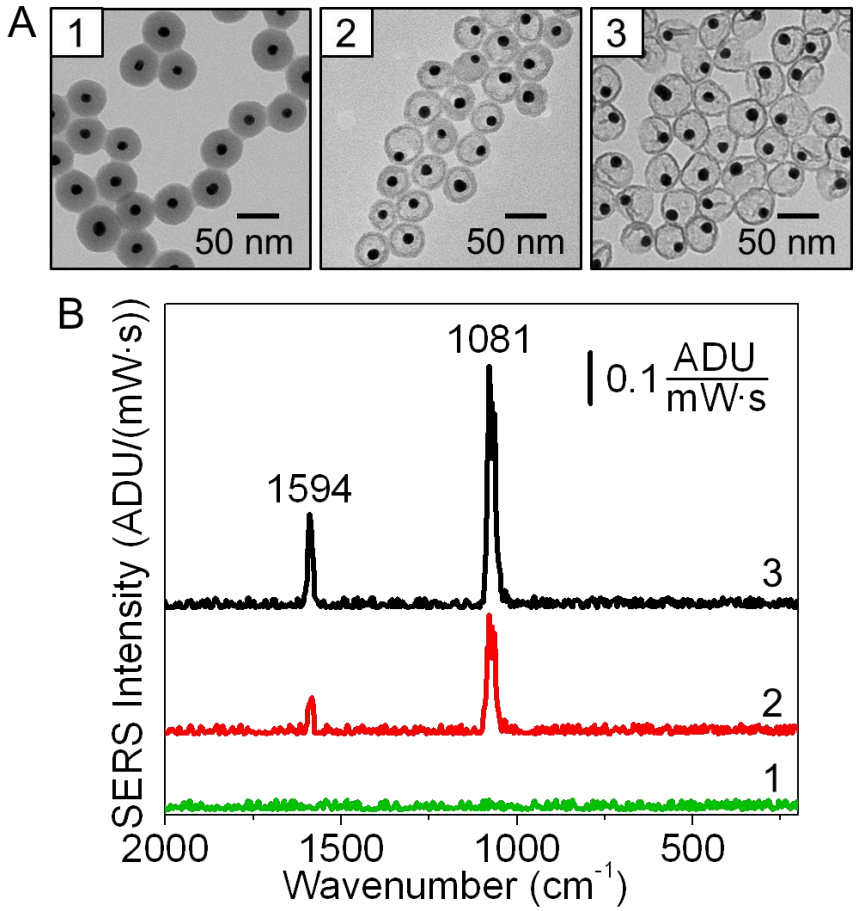

Figure 4.8 (A) Representative TEM images and (B) SERS spectra of IE Au@SiO_2 nanospheres at different $\Delta\lambda_{max}$ (1) 0.0, (2) 4.1, and (3) 6.4 nm. The observed vibrational modes of 4-ABT are labeled: CH bending at 1081 cm^{-1} and ring stretching at 1594 cm^{-1}. Spectral noise was estimated as the standard deviation ranging from 1900 – 1700 cm^{-1} in each spectrum.

these slight differences likely arise from small differences in the effective local refractive index near the metal surface which could contain both water and/or silica.

4.3.4 Implications of Effective Refractive Index Surrounding Au@SiO_2 Nanoparticles on SERS Detection of 4-Aminobenzenethiol

To evaluate how varying the effective refractive index near the gold core impacts the SERS detection of small molecules, 4.5 nM IE Au@SiO_2 nanoparticles were incubated with 10 μM 4-ABT for 1 hour. This molecule was selected because it has high affinity for the gold core and is smaller than the ~2 nm pores in the microporous silica membrane.[273] Three internally etched samples with $\Delta\lambda_{max}$ values of 0.0, - 4.1, and - 6.4 nm were used. SERS signals are hypothesized to increase in samples with larger (blue) wavelength shifts, and as a result, decreasing local effective refractive indexes are used. Figure 4.8 shows the SERS spectra and corresponding TEM images for these three IE Au@SiO_2 nanosphere samples. The trends follow the expectation in a qualitative fashion. Two vibrational modes (ring stretching (1594 cm^{-1}) and C-H bending (1081 cm^{-1}))[302] are observed for 4-ABT for the two internally etched samples. Further experiments are needed to understand the intensity differences, such as SERS intensity response as a function of extinction maximum wavelength shift.

4.4 Conclusions

In summary, the present study demonstrates that shifts in the LSPR wavelengths of silica-coated gold nanoparticles are a better indicator of the degree of silica dissolution vs. the previously reported etching time. The extinction maximum wavelength is varied by 4.8 nm when etching time is used to follow etching; whereas, ~ 0.5 nm variation is observed when spectral changes are used. Preliminary SERS

studies and the use of a dielectric model indicate that shifts in the LSPR spectra provide correlated information regarding the effective local refractive index near the metal surface. Further utilization of this new protocol will lead to greater predictability in the quantitative direct SERS response of small molecules.

CHAPTER V

CONCLUSIONS AND FUTURE DIRECTIONS

5.1 Conclusions

In summary, the findings presented in this thesis include the synthesis and characterization of gold nanospheres, silica-coated gold nanospheres, and internally etched, silica-coated gold nanospheres for the qualitative and quantitative SERS detection of small molecules. The methods used and the results reported from these studies can be applied to future work toward understanding the mechanism of passive molecular transport through silica membranes for SERS detection. Additionally, these findings should facilitate a better understanding of the mechanism of SERS-active substrates in applications such as environmental and biological detection.

Chapter 1 reviewed the mechanisms and importance of LSPS, Raman, and SERS spectroscopies. These methods are important for monitoring the stability of nanoparticles and for identifying target molecules in water or on metal nanoparticle surfaces, respectively. The small/tunable sizes, core-composition variations, and diverse surface chemistries of nanomaterials can be exploited, but they are limited by large surface energies. These large surface energies can destabilize the materials, and can lead to aggregation, which results in irreproducible SERS signals.

In Chapter 2, citrate-stabilized gold nanosphere concentration and stability upon functionalization with 2-naphthalenethiol were monitored using simultaneous LSPR and SERS measurements. Extinction and SERS spectral intensities were plotted for various nanoparticle and analyte concentrations, where the molecular concentration ranged from sub-monolayer to more than a monolayer. At sub-monolayer surface

coverages, the extinction and SERS intensities increased linearly, but above this value, nanoparticles aggregated uncontrollably. This uncontrolled aggregation was attributed to molecules displacing the stabilizing citrate molecules from the gold surface. This, in turn, induced nanoparticle aggregation, which caused electromagnetic coupling between the metal cores and nanoparticle sedimentation. These results suggest that control over nanoparticle concentration and molecular surface coverage is crucial for both plasmonic and SERS studies, which should lead to more reproducible SERS detection.

In Chapter 3, a post-synthesis quality-control step was implemented with respect to silica-coated gold ($Au@SiO_2$) nanospheres in order to reduce the variation in distance-dependent SERS responses. Gold nanospheres were encapsulated in various silica shell thicknesses, and all samples were purified using the traditional centrifugation step. Next, a portion of each sample was further purified by passing through a chromatographic column. The structures, stability, and SERS responses from both unpurified (centrifugation alone) and purified (centrifugation, plus chromatographic column) $Au@SiO_2$ nanosphere samples were evaluated. These results confirmed that uncoated and/or partially coated gold nanospheres were retained by the column matrix, while only fully coated nanoparticles were eluted and recovered. The SERS intensity of 2-naphthalenethiol from column-purified samples followed the well-known SERS distance-dependence model. This chromatographic purification-step improved the homogeneity of the samples and should be applicable to other solution-phase nanoparticles for more predictable functioning in future applications.

Chapter 4 focused on the fabrication and modeling of internally etched silica-coated gold (IE Au@SiO_2) nanospheres for SERS measurements of a small molecule. The formation of IE Au@SiO_2 nanospheres were monitored *in situ* by measuring LSPR wavelength shifts instead of the previously reported etching time. Preliminary SERS studies and the use of a dielectric model suggest that shifts in the extinction spectra can be correlated to effective local refractive index changes near the gold core. Further exploitation of LSPR monitoring will lead to greater predictability in the quantitative direct SERS-response of small molecules in biological and environmental applications.

Appendix 1 demonstrated that internally etched silica-coated gold (IE Au@SiO_2) nanospheres can be synthesized with various degrees of internal silica etching by increasing the time at which silica dissolution was stopped. This study was completed to determine the optimal internal silica-etching of (IE Au@SiO_2) nanospheres for predictable SERS measurements. The second appendix focused on troubleshooting steps for silica condensation on gold nanoparticle surfaces, as well as for the reverse reaction (etching). This troubleshooting guide should be useful for those who are trying to repeat these reactions. The third appendix included preliminary studies for investigating how ionic strength, pH, and polarity of the solution each impact the SERS detection of small molecules using internally etched silica-coated gold nanospheres. These studies could be used as a guide for future investigations, which could assist with understanding how small molecules diffuse through the silica shell and toward the metal core prior to SERS detection.

5.2 Future Directions

It is likely that the use of internally etched silica-coated nanospheres in SERS detection applications will expand in the future as a direct result of the improvements described in this thesis. First, the amount of internal silica-etching should be optimized for the highest SERS signal. This study can be accomplished by designing an experiment to evaluate the SERS response of a single analyte as a function of extinction-maximum wavelength shift. Once the SERS-active substrates that induce the highest SERS intensity of a target molecule are obtained, the solution conditions (ionic strength, pH, and polarity) can be varied using citrate bis-tris propane [CBTP] with a pH ranging from 2.5 to 9.5. It is important that a buffer be used to maintain consistent pH for the duration of each study. Next, passive molecular transport can be modulated using ionic strength variations. This experiment is important, because increasing ionic strength should increase the size of the micropores in the silica membrane for increase molecular transport.

Next, while maintaining the chosen ionic strength, the pH of the solution should be varied in an attempt to change the charge of the target molecule. During this study, the surface charge of the stationary phase (SERS-active substrates) should be maintained, as the pH of the solution will always be above the isoelectric point of the silica (2 – 3). The charge of the target molecules, however, will vary from positive, to neutral, to negative based on the isoelectric point of the molecules and the pKa of the substituents. As a result of this variation in charge, the SERS response should follow a Gaussian curve. As positively charged molecules are expected to interact with the silica surface, which is negatively charged, instead of diffusing through the silica

membrane, no SERS signal should be observed. Neutrally charged molecules, on the other hand, should be passively transported through the silica membrane, allowing for a SERS signal to be observed. This is because only small, negatively charged analytes should be transported through the silica shell and detected using SERS. Preliminary studies in Appendix 2 support this hypothesis.

Finally, while maintaining the optimal ionic strength and pH, the polarity of the sample may be varied (i.e., by increasing the amount of ethanol in an aqueous solution). SERS signal intensities should increase if molecular solubility increases. Preliminary experiments support this expectation. Moreover, the pH can be increased even higher than 8.5 because silica dissolution will not occur in ethanol.

In summary, future studies could be carried out using IE Au@SiO_2 nanospheres for the reproducible and quantitative SERS-detection of small, biologically and chemically important molecules. Each analyte in the mixture should have a unique Raman band for identification. The advances in nanomaterial synthesis and purification that were described in this thesis could then be used to solve important environmental and medical problems where nanomaterial stability and signal enhancement are needed.

APPENDIX A

INTERNALLY ETCHED SILICA-COATED GOLD NANOSPHERES SYNTHESIS AND TROUBLESHOOTING OF SILICA CONDENSATION ON GOLD NANOSPHERES

A.1 Introduction

Here the goal was to determine the optimal internally etched silica-coated gold (IE Au@SiO_2) nanospheres that produce the largest SERS signal intensity of the target analyte, which encapsulates the gold core with a complete silica membrane of thickness around 4 nm. To complete this study, several IE Au@SiO_2 nanospheres were synthesized using previously reported procedure.[161] Each IE Au@SiO_2 nanosphere sample was quenched at a different time with a concentrated HCl solution to obtain nanostructures with various degrees of internal silica etching and a final pH of 4. The composite nanomaterials were washed with nanopure water to increase the pH and purified via column chromatography. The morphology, the stability of IE Au@SiO_2 nanospheres and the SERS-activity of 2-naphthalenethiol (2-NT) using IE Au@SiO_2 nanostructures substrates were compared.

A.2 Synthesis and LSPR Analysis of IE Au@SiO_2 Nanospheres

IE Au@SiO_2 nanoparticles were synthesized by monitoring the etching time, a method that was first reported by Roca *et al*. in 2008.[161] Several degrees of IE Au@SiO_2 nanospheres were fabricated by varying the time at which the solution was neutralized. After purifying each IE Au@SiO_2 nanoparticle sample, a LSPR spectrum was collected and analyzed using 4 nM IE Au@SiO_2 nanospheres in water. The LSPR spectra are shown in Figure A.1. As expected, the extinction maximum

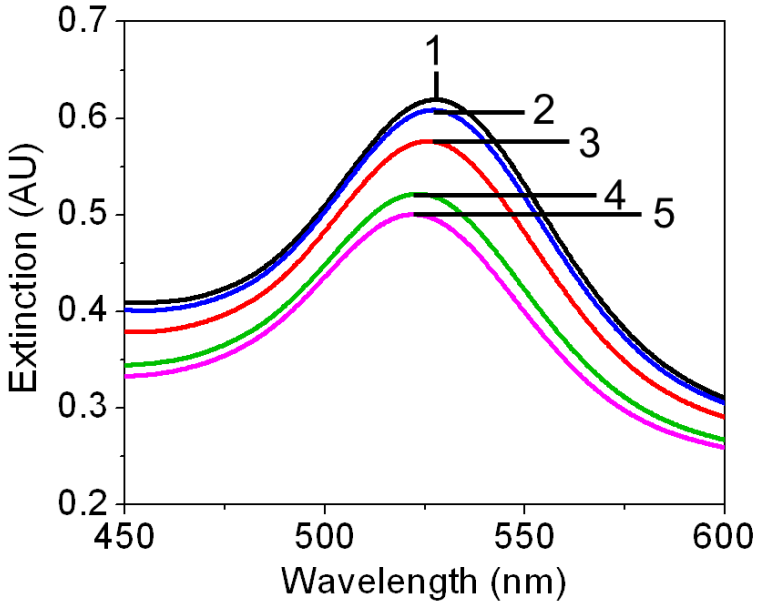

Figure A.1 LSPR spectra and extinction maximum wavelength for IE Au@SiO_2 nanospheres quenched after (1) 0 (527.7 nm), (2) 5 (527.1 nm), (3) 15 (525.7 nm), (4) 25 (523.3 nm), and (5) 35 (522.1 nm) minutes etching. All LSPR spectra were smooth using Matcad (10 points smoothing).

wavelength blue-shifts by 5.6 nm as a function of etching time, which reveals that the dielectric environment near the gold cores is decreasing and reflects silica replacing by water as mention many time previously throughout this dissertation.

A.3 SERS Study of 2-Naphthalenethiol Using IE Au@SiO_2 Nanoparticles

To evaluate how the optical properties of nanoparticles influence resulting SERS signals, 4 nM of all 5 IE Au@SiO_2 nanoparticle samples was incubated with 10 μM of 2-naphthalenethiol for 1 hour. Delta NU advantage with 785 nm excitation wavelength was used, and SERS spectra were collected for the duration of the study by taking 1 every 60 seconds of integration time at ~50 mW power.

The 60 minutes SERS spectrum is plotted in Figure A.2 for each IE nanoparticles sample. Table A.1 reports the spectral noise that is calculated by averaging a range in each spectrum from 1700 – 1900 ADU and the SERS signal intensity for each observed vibrational mode of 2-NT after subtracting the spectral noise. These vibrational modes are: 1064 cm^{-1} (C-H bending) and 1380 and 1622 cm^{-1} (both ring stretching). The data reveal no SERS signal from 0 min IE Au@SiO_2 nanostructures (Figure A.2-1) because the 2-NT molecules are unable the diffuse through the silica layer toward the gold for the direct metal-analyte interaction, which is one of the two main enhancement mechanism possesses by the SERS effect. However, SERS response of 2-NT are observed from 5 - 35 min IE Au@SiO_2 nanostructure, and are shown in Figures A.2-2 to A.2-4. This SERS signal intensity increases as a function of etching time for all three vibrational modes observed. This increase indicates that more molecules are on the metal surface because larger pores on the silica matrix near the gold cores are formed with increasing etching time. The optimal IE Au@SiO_2

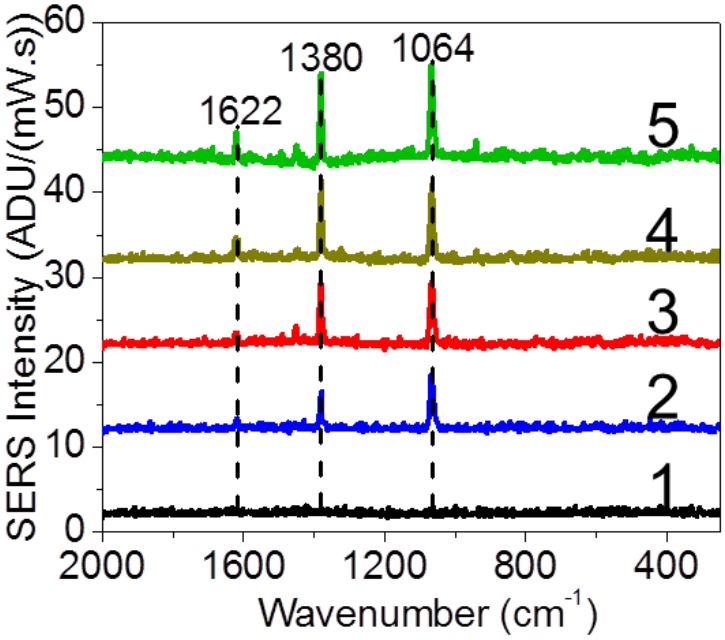

Figure A.2 SERS spectra of 10 μM 2-naphthalenethiol incubated in 4 nM IE Au@SiO_2 nanoparticles for 1 hour after being etched for: (1) 0, (2) 5, (3) 15, (4) 25, and (5) 35 minutes. The observed vibrational modes, labeled with the dashed line, are: 1064 cm^{-1} (CH bending) and 1380 and 1622 cm^{-1} (ring stretching). All spectra are baseline corrected using control spectra (spectra without the analyte). Spectral noise is determined by averaging a range in the spectrum from 1700 to 1900 ADU.

Table A.1 Spectral noise and SERS signal intensity for each vibrational mode of 2-naphthalenethiol (CH bending at 1064 cm^{-1} and ring stretching at 1380 and 1622 cm^{-1}).

Etching Time (min)	**0**	**5**	**15**	**25**	**35**
Noise (ADU)	0.192	0.228	0.254	0.193	0.220
1064 cm^{-1} (ADU)	0.153	5.851	6.687	7.851	9.978
1380 cm^{-1} (ADU)	0.074	3.539	6.763	8.005	8.953
1622 cm^{-1} (ADU)	0.159	0.868	1.113	2.090	2.501

Note: 4 nM of each IE Au@SiO_2 nanoparticles (0, 5, 15, 25, and 35 minutes) is incubated with 10 μM 2-naphthalenethiol for 1 hour prior to data collection. Spectral noise is calculated by averaging a range on each spectrum where no vibrational mode of the target molecule is observed: from 1700 to 1900 ADU.

nanostructures can be obtained between 25 and 35 minute etching of internal silica because the SERS response only changed by 0.900 ADU, which indicates that the entire gold surface is available for molecular binding.

A.4 Structural Analysis of IE Au@SiO_2 Nanoparticles

To further investigate the changes observed in both extinction and SERS responses from IE Au@SiO_2 nanoparticles, TEM images were collected for each sample, and representative images are shown in Figure A.3. After conducting a student t-test, the average mean diameter of all IE Au@SiO_2 nanostructures remained the same (d = ~60 nm) before and after the etching at a 95% confidence limit. This similarity in size indicates that silica dissolution only occurs from the internal silica layer located at the gold surface. As etching time increased, the internal etching space surrounding the gold cores adequately increased, thereby allowing the gold core to move from the center of the nanoparticle to the edge of the silica membrane (see Figures A.3D and A.3E). Further etching of the silica membrane will result in gold core exposure.

Another observation is that ~50% of the nanoparticles are free silica particles (nanoparticles without gold core), which can lead to inconsistent silica shell thickness. Therefore, to obtain a more homogeneous silica-coated gold (Au@SiO_2) nanoparticle sample, a troubleshooting procedure was carried out by exploring each step from the stepwise synthesis depicted in Figure A.4A. During this troubleshooting, all 3 steps from Figure A.4A were completed for each parameter. The chemical structures of all silica precursors used during silica condensation on gold nanospheres are shown in Figure A.4B. To reduce the percent of free silica

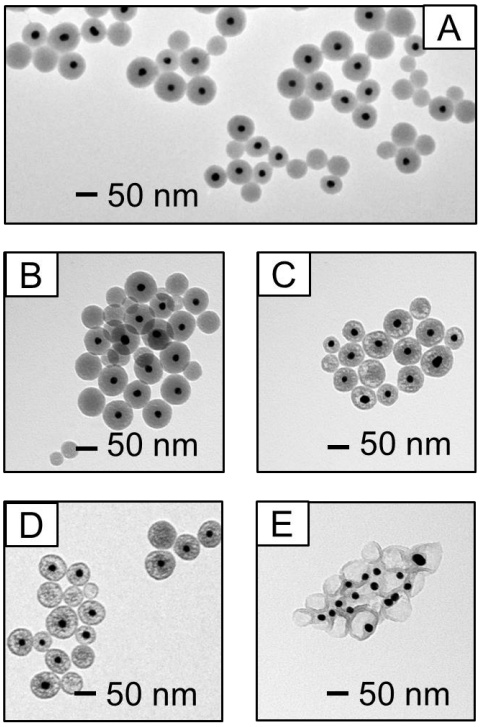

Figure A.3 Representative TEM images and average diameter for IE Au@SiO_2 nanospheres quenched after (A) 0 (d = 60.1 ± 6.8 nm), (B) 5 (d = 60.1 ± 5.9 nm), (C) 15 (d = 59.9 ± 5.5 nm), (D) 25 (d = 59.8 ± 5.9 nm), and (E) 35 (d = 59.8 ± 7.0 nm) minutes etching. Over 100 particles were analyzed to determine the average mean diameter and the standard deviation for each composite nanostructure.

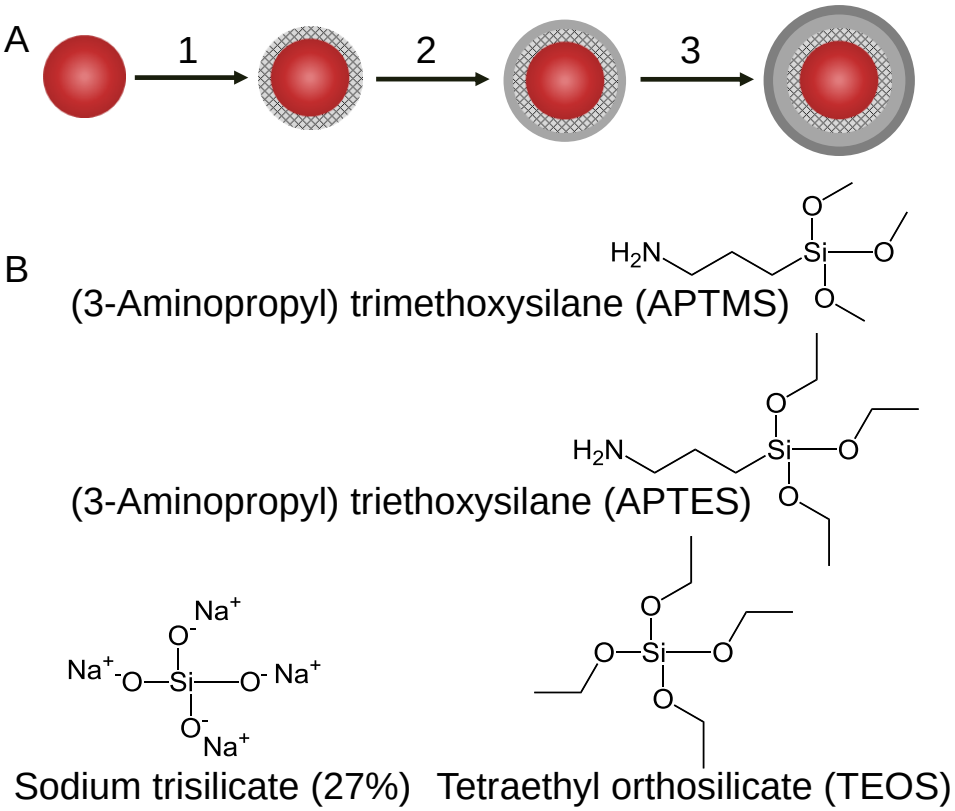

Figure A.4 (A) Synthesis steps of silica-coated gold nanospheres: (1) APTMS or APTES functionalized gold nanospheres to promote silica condensation, (2) addition of sodium silicate to thicken the silica shell to 4 nm to establish the stability of the gold nanoparticles in ethanol, and (3) addition of ethanol and TEOS at pH greater than 8 to thicken the external silica layer. (B) Chemical structures of the silica precursors used during the synthesis.

particles observed during silica condensation on gold nanospheres, a parameter was evaluated in each synthesis step separately, and extinction spectroscopy and transmission electron microscopy (TEM) were used for analysis. A flow chart of the experimental plan is shown in Figure A.5, with all parameters, expectations, and objectives.

A.5 Ethanol Implication on Silica Condensation on Gold Nanospheres

Because ethanol is added in Step 3 (Figure A.4A) to increase the rate of silica condensation on gold nanospheres, it was hypothesized that decreasing the volume of added ethanol will reduce the rate of silica condensation, which should decrease the percent of free silica particles observed in Au@SiO_2 nanosphere samples. To complete this study, the water-to-ethanol volume ratio was increased from 1:4 to 1:2, instead of 1:4.4, by decreasing the volume of ethanol added. Once the synthesis of Au@SiO_2 nanospheres was completed, the samples were purified, and a LSPR spectrum and a TEM image were collected for each sample (Figure A.6). The extinction maximum wavelengths are 534.5, 533.8, and 533.5 nm for Au@SiO_2 nanospheres synthesized with 1:2, 1:3, and 1:4 water-to-ethanol volume ratio, respectively (Figure A.6A). These data indicate that a larger population of free silica particles than for those synthesized with the 1:4.4 ratio of water-to-ethanol volume (Figure A.6B). This result rejects the hypothesis because, as the volume of ethanol decreases, the rate of silica condensation also decreases, which increases silica nucleation and reduces silica growth according to Liz-Marzán.[303] Because silica solubility is drastically low in ethanol, polymerization of silica occurs.

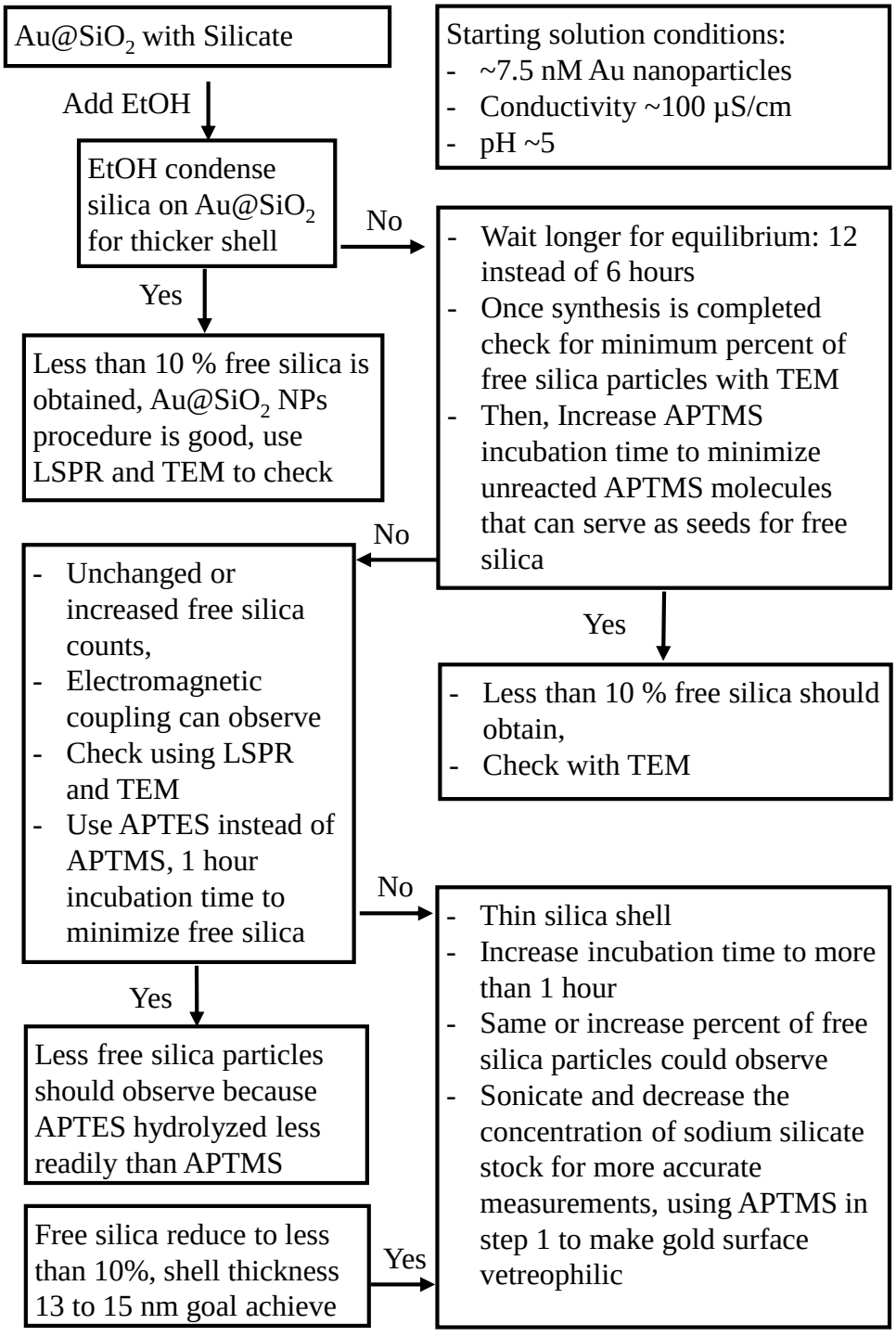

Figure A.5 Experimental procedures for minimizing the percent of free silica particles observed on synthesized $Au@SiO_2$ nanoparticles.

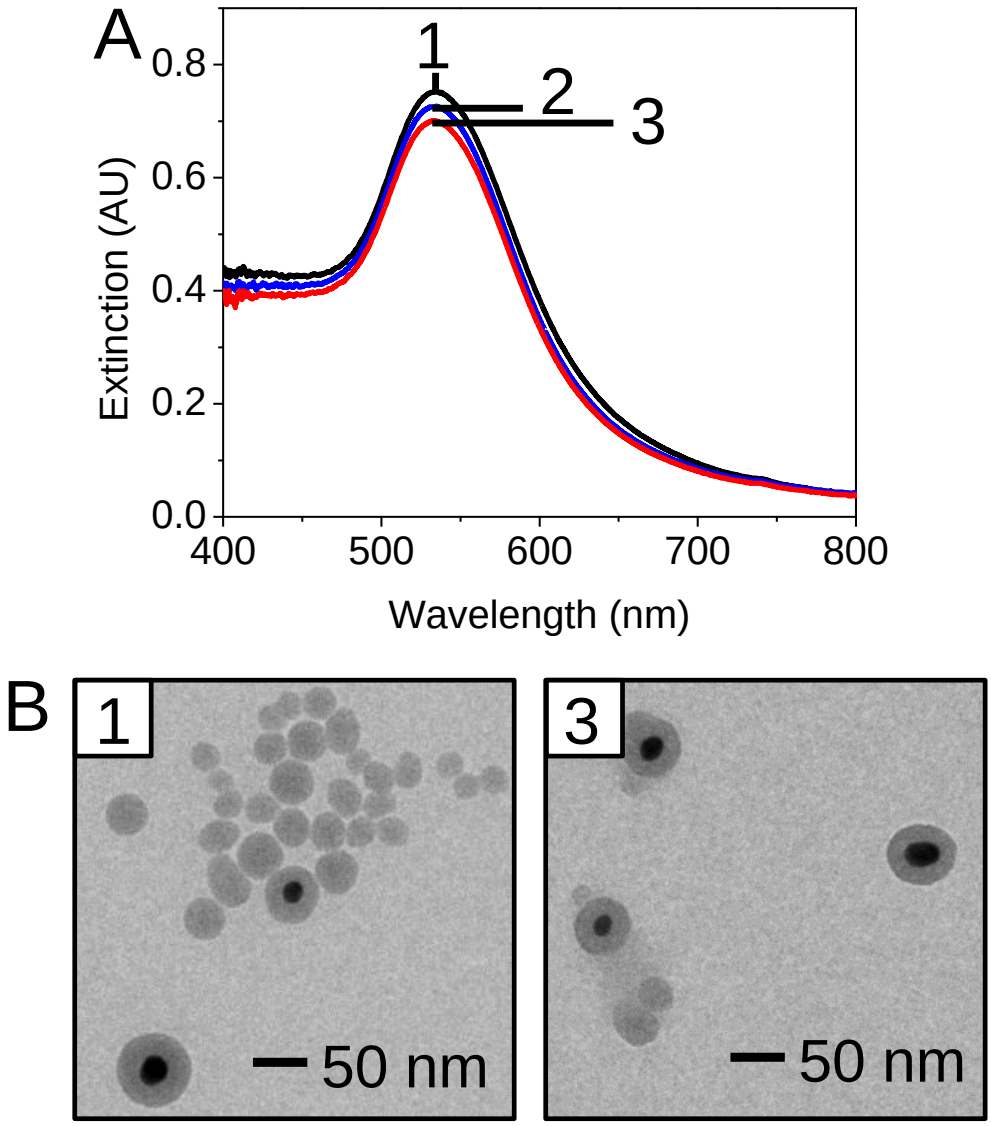

Figure A.6 Extinction and structural analysis of Au@SiO_2 nanospheres synthesized using various water-to-ethanol volume ratios during step 3 in Figure A1.4. (A) LSPR spectra of Au@SiO_2 nanoparticles synthesized using: (1) 1:2, (2) 1:3, and (3) 1:4 water-to-ethanol ratio. The extinction maximum wavelength and full width half max are: 534.5 nm and 0.5379 eV, 533.8 nm and 0.5222 eV, and 533.5 nm and 0.5196 eV, respectively. (B) Representative TEM image for Au@SiO_2 nanospheres fabricated using (1) 1:2 and (2) 1:4 water-to-ethanol ratio.

A.6 APTMS Incubation Time Effect on Silica-Coated Gold Nanospheres

The next step was to determine if the time used to make the gold surfaces vitreophilic is sufficient to allow all the APTMS molecules to bind to the gold nanoparticle. This is because any excess APTMS molecules present in the solution prior to the addition of sodium silicate can serve as nuclei for further silica growth. To investigate the impact of APTMS incubation time on the formation of free silica particles during silica condensation on gold nanospheres, the time was varied from 15, 30, and 60 minutes. Figure A.7 shows the LSPR spectra for all three samples and the TEM images for Samples 1 and 3. The extinction maximum wavelength for all three samples is centered at (1) 531.5 nm, (2) 531.9 nm, and (3) 549.5 nm, respectively (Figure A.7A). These data indicate no significant differences between Samples 1 and 2 other than a ~5 nm red-shift in the LSPR wavelength that is greater than uniform silica-coated sample reported in the literature,[167] which could be associated with the large percent of free silica particles observed. However, Sample 3 shows a greater shift in the LSPR wavelength and a broad spectrum, which suggest metal nanoparticle coupling and/or aggregation.

Representative TEM images are shown in Figure A.7B for Samples 1 and 3 only because Sample 2 possesses similar optical properties as Sample 1 and thereby should have similar structure. Both LSPR and structural data are correlated for all samples. Sample 3 on the other hand, shows very different structure as expected based on their LSPR wavelength. This observation can be explained as APTMS molecules polymerization instead of functionalization. This polymerization allows all silica precursors added to further growth and form a bed of silica. As gold nanospheres are

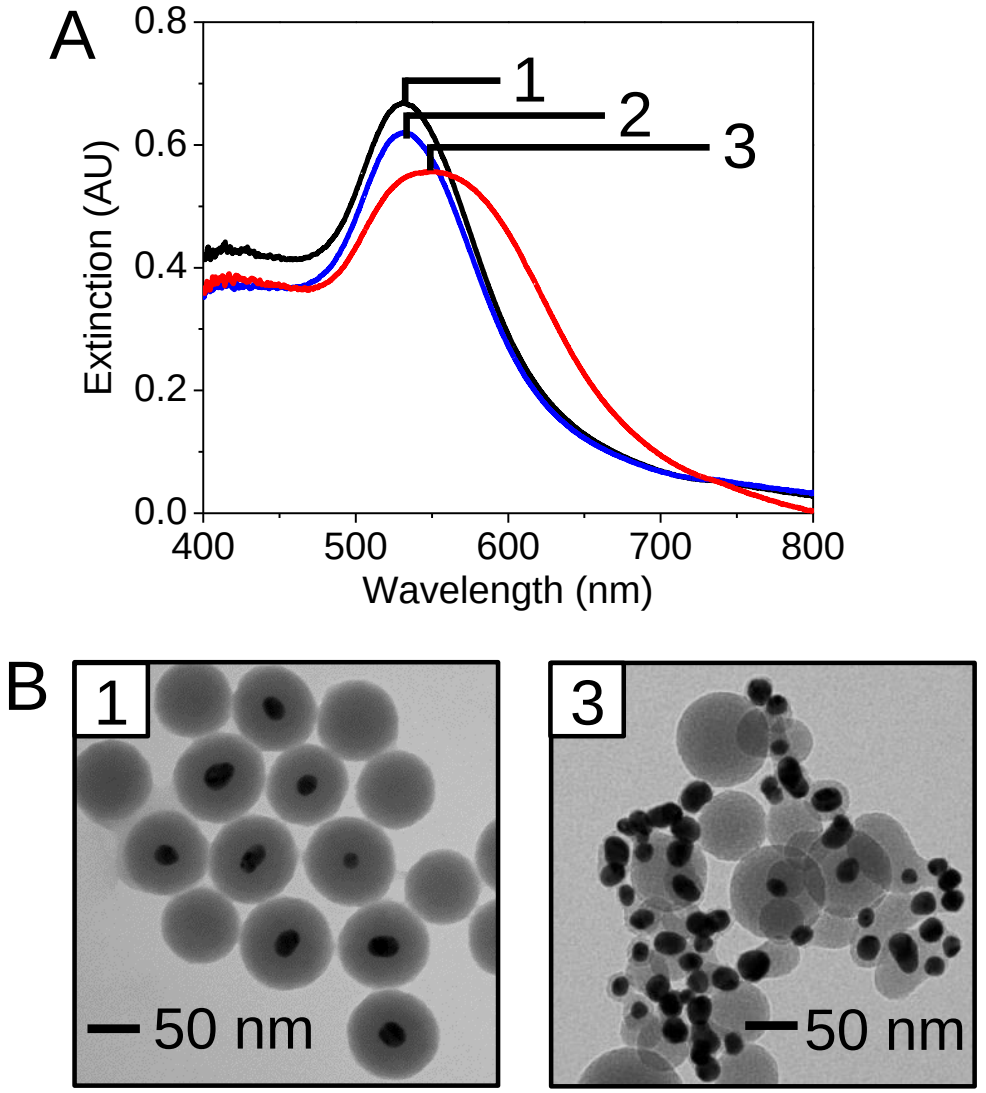

Figure A.7 Extinction and structural analysis of Au@SiO_2 nanospheres synthesized using various incubation times for APTMS in Step 1. (A) LSPR spectra of Au@SiO_2 nanoparticles after incubated for: (1) 15, (2) 30, and (3) 60 minutes. Their extinction maximum wavelength and full width half max are: 531.5 nm and 0.4986 eV, 531.9 nm and 0.5010 eV, and 549.5 nm and 0.6272 eV, respectively. (B) Representative TEM image for Au@SiO_2 nanospheres incubated with APTMS for (1) 15 and (2) 60 minutes.

known to be attracted to such silica layer, therefore, the gold nanoparticles present in the solution attached on the silica bed, which is observed in Figure A.7B-3.

A.7 APTMS *vs.* APTES Effect on Silica Condensation on Gold Nanoparticles

APTES, and APTMS, were used to functionalize the gold nanoparticle surface prior to silica condensation. This study is performed to determine if the connecting agent is the reason for large population of free silica particles, since APTMS hydrolyzes much faster than APTES. The same protocol detailed earlier was used for both samples, where APTMS or APTES is used to make the gold surface vitreophilic for further silica growth. The APTES sample was incubated for 1 hour during functionalization while APTMS sample was incubated for only 15 minutes. Extinction spectra and TEM images are shown in Figure A1.8. As expected, the absorption band (531.1 nm (Figure A.8A-1)) and the structural image (Figure A.8B-1) obtained for APTMS functionalized $Au@SiO_2$ nanospheres (sample 1) are similar to data from Figure A.7A-1 (LSPR) and Figure A.7B-1 (TEM) because the same procedure is used.

Sample 2 ($Au@SiO_2$ nanospheres synthesized with APTES) on the other hand, possess a plasmon wavelength at 524.3 nm (Figure A.8A-2), a number reported by Liz-Mazán in 1996[167] for fully coated nanoparticle with a low percent of free silica particles and silica shell from 4 to 15 nm thick. The TEM image in Figure A.8B-2 shows $Au@SiO_2$ nanospheres with no free silica, but the silica shell thickness is only ~ 4 nm, which is too thin for future applications. These observations suggest that APTES incubation should be greater than 1 hour because APTES is less likely to hydrolyze in air and/or water, as it is less polar than APTMS.

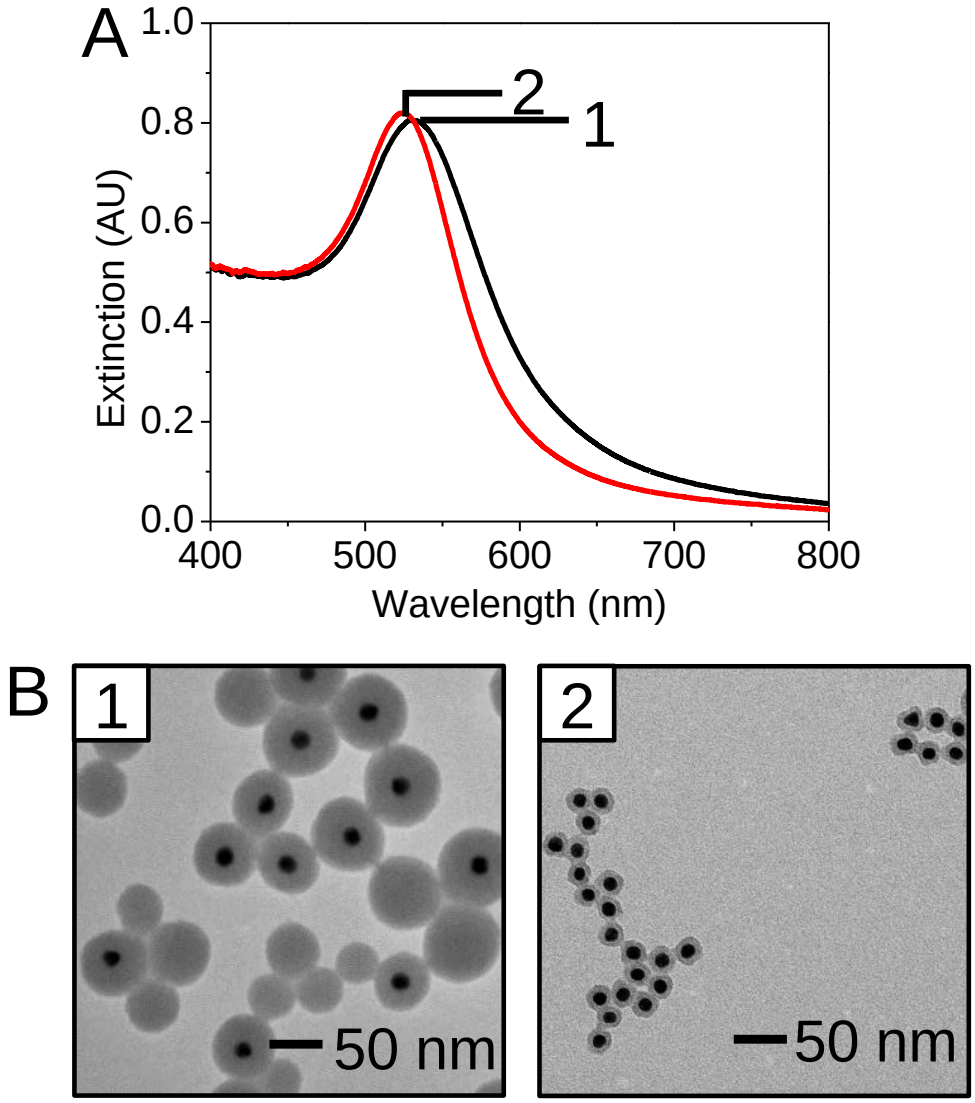

Figure A.8 APTMS *vs.* APTES linking agent to functionalize the gold surface prior to silica condensation. (A) Extinction spectra of Au@SiO_2 nanoparticles synthesis using (1) APTMS and (2) APTES to make the gold surface vitreophilic, with extinction maximum wavelength and full width half max equal to 531.1 nm and 0.4611 eV and 524.3 nm and 0.3696 eV, respectively. (B) Representative TEM images for Au@SiO_2 nanospheres synthesis with (1) APTMS and (2) APTES.

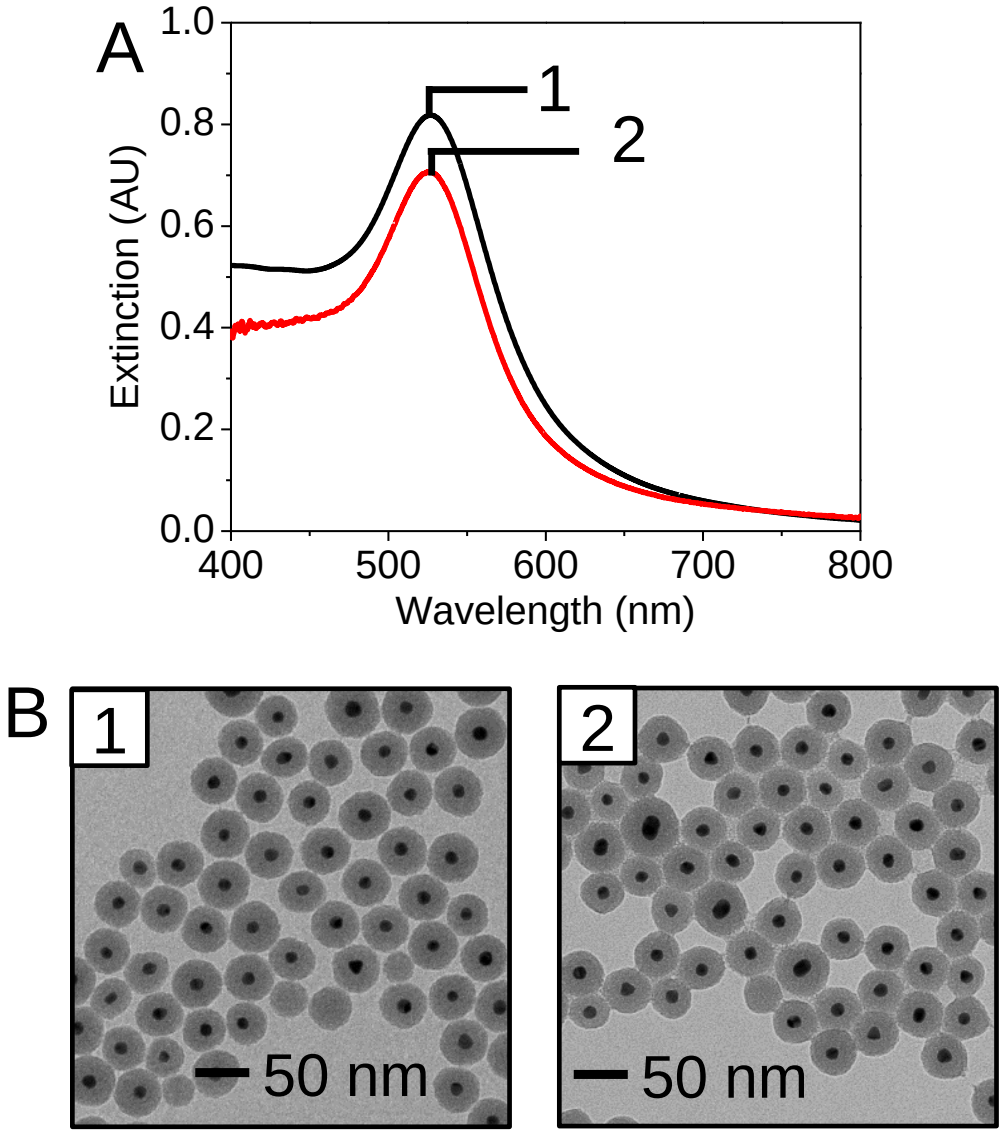

Figure A.9 (A) LSPR spectra of Au@SiO_2 nanoparticles synthesis with (1) 10 and (2) 2.7% sodium silicate (stock). The plasmon wavelength and full width half max are: 526.6 nm and 0.4009 eV and 525.7 nm and 0.3803 eV, respectively. (B) Representative TEM images for Au@SiO_2 nanospheres synthesis using (1) 10 and (2) 2.7 % sodium silicate.

A.8 Sodium Silicate Viscosity and Concentration Effect on Silica Condensation

Finally, the viscosity and the concentration of the stock sodium silicate solution are monitored prior to being used in silica condensation to uniform solution which should minimize silica nucleation while maximizing silica growth. In this study, the 27 % stock sodium silicate is sonicated and diluted with water to 10 % and 2.7% weight. The final concentration of sodium silicate during silica condensation on gold nanospheres remains the same for both samples, as well as does the protocol. After purifying each of the Au@SiO_2 nanospheres, a LSPR spectrum and a TEM micrograph is collected for both samples, which are shown in Figure A.9. The extinction maximum wavelength for both samples is 526.6 nm (Figure A.9A-1) and 525.7 nm (Figure A.9A-2), respectively. According to literature, these samples should contain fully coated Au@SiO_2 nanospheres with very few free silica particles.

The representative TEM images show in Figure A.9B reveals structure with few free silica particles, after analyzed over 100 nanoparticles the percent of free silica particles is ~6 % and ~2 %, respectively. Following this protocol, fewer free silica particles should be observed, the extinction maximum wavelength should be similar to those above, and experimental silica shell thickness should be comparable to calculated.

A.9 Conclusions

In this report we synthesized and characterized stable and SERS-active IE Au@SiO_2 nanoparticles in a stepwise process. We demonstrated that quantitative SERS signals of target molecules can be achieved by using solution-phase gold nanoparticles encapsulating in porous silica membrane. The magnitude of the SERS

intensity for 2-NT between 25 to 35 minutes IE $Au@SiO_2$ nanoparticles were only different by 0.900 ADU. This suggests that the optimal gold nanostructures that are stabilized with a full silica membrane and produce large SERS signal lay between 25 to 35 minutes internal silica etching and the entire gold surface should be available for molecular binding. During the troubleshooting of $Au@SiO_2$ nanospheres, the results reveal that varying water to ethanol volume ratio, varying APTMS incubation times, and used APTES to functionalize the gold nanoparticle surface prior to silica condensation instead of APTMS do not improve the homogeneity of $Au@SiO_2$ nanospheres. However, sonicating and decreasing the concentration of the sodium silicate stock reduces silica nucleation and increases silica growth for more predictable silica shell thicknesses and LSPR wavelength.

APPENDIX B

PRELIMINARY STUDIES OF SOLUTION CONDITIONS IMPLICATIONS ON PASSIVE MOLECULAR TRANSPORT THROUGH SILICA MEMBRANE AND MULTI-ANALYTES DETECTION USING SERS SPECTROSCOPY

B.1 Introduction

In this study, solvent ionic strength, pH, and polarity are varied stepwise to determine the optimal solution conditions that produce passive molecular diffusion through silica membrane toward the gold core for large and reproducible SERS measurements of target analytes. To start, IE Au@SiO_2 nanospheres with a fixed internal silica etching are synthesized using the new silica dissolution protocol described in Chapter 4. The composite nanospheres sample is purified using hydrophobic interaction chromatographic column. Figure B.1 depicts a flow chart of the experimental design in a stepwise manner describing parameters, objectives and expected results or trends. The SERS-activity of 4-aminobenzenethiol (4-ABT) is monitored as a function of all parameters, including KCl concentration, pH, and percent ethanol. 4-Aminobenzenethiol was chosen because it is small, Raman-active, and contains a thiol group that can tightly bind to gold (bond strength = ~47 kcal/mol). A SERS spectrum of 10 µM 4-ABT on 4 nM citrate stabilized gold nanospheres is shown in Figure B.2 where all observed vibrational modes are labeled and assigned in Table B.1.

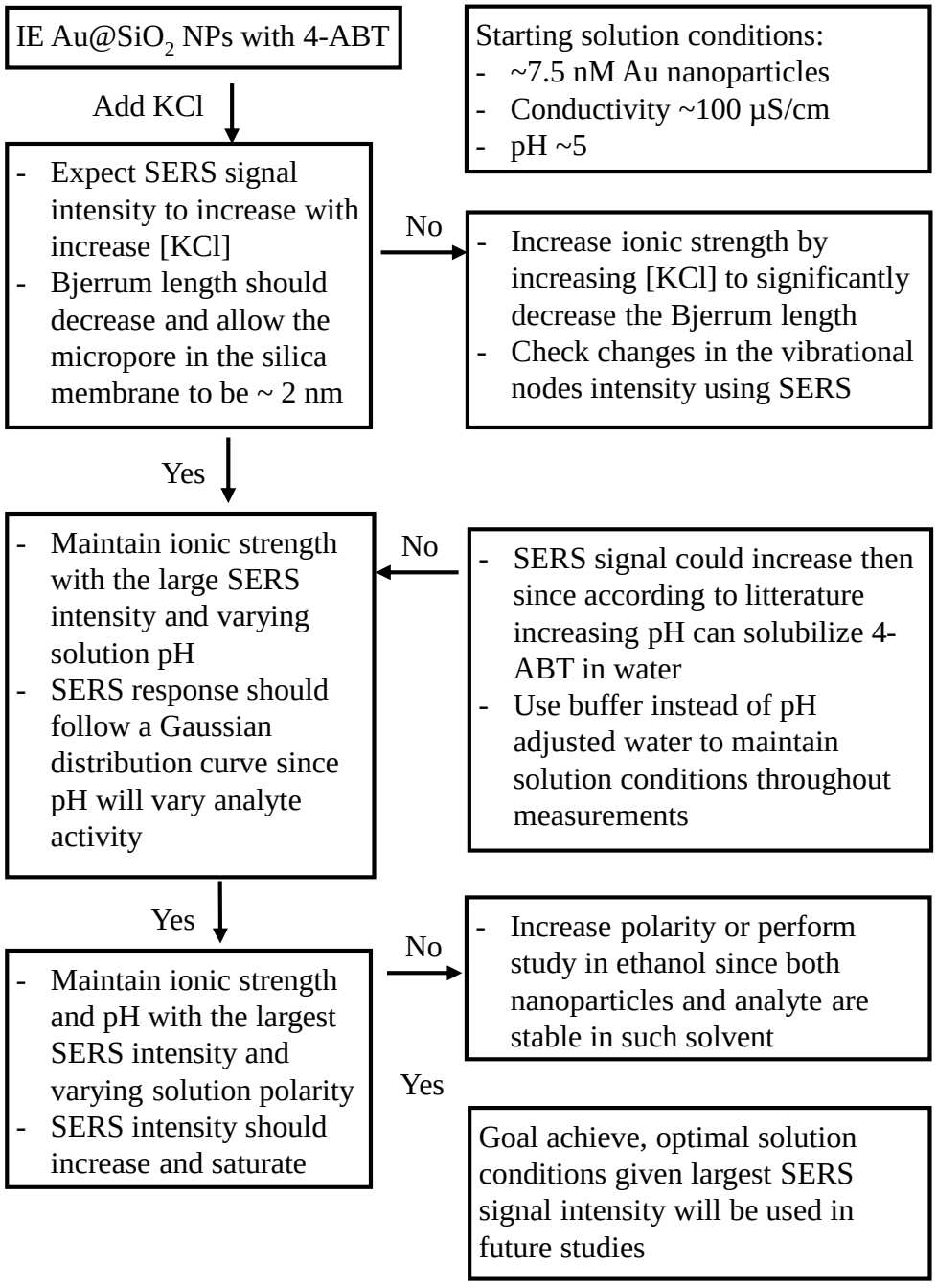

Figure B.1 Experimental plan to determine the optimal solution conditions for passive molecular diffusion through the silica membrane on gold nanospheres for large, but reproducible and quantitative SERS response of small molecules.

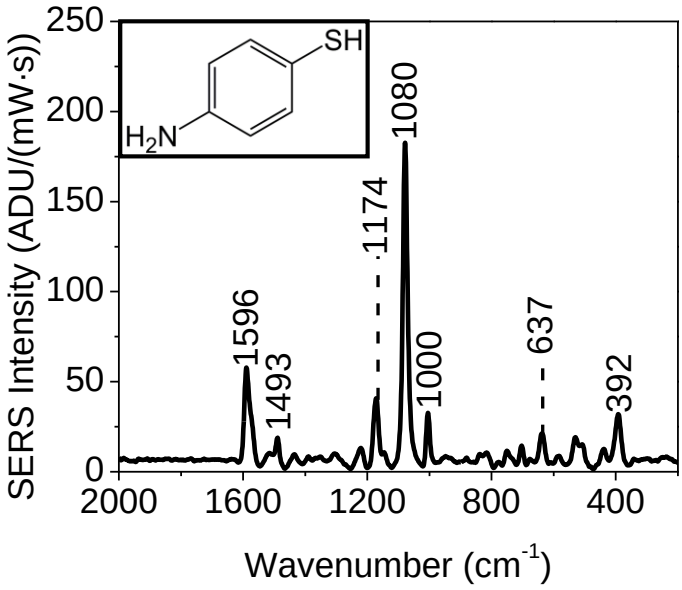

Figure B.2 SERS spectra of 10 μM 4-aminobenzenethiol (4-ABT) adsorbed on the surface 4 nM citrate stabilized gold nanospheres. The observed vibrational bands are labeled. The inset illustrates the chemical structure of the analyte 4-ABT. SERS collection parameters: power laser = 2 mW, λ_{Ex} = 632.8 nm, and t_{int} = 60 seconds.

Table B.1 Raman shift assignments of 4-aminobenzenethiol (4-ABT) on citrate stabilized gold nanospheres.[1-3]

Literature Raman Shift (cm^{-1})	Experiment Raman Shift (cm^{-1})	Assignments
1587	1590	Ring stretching
1485	1491	Ring stretching & CH bending
1425		Ring stretching & CH bending
1389		Ring stretching & CH bending
1177	1173	CH bending
1140		CH bending
1078	1080	CS stretching
1003	1000	CC & CCC bending
819		CH waging
636	637	CCC bending
391	392	CS bending

B.2 Ionic Strength, pH, and Polarity Effect on Molecular Diffusion through IE $Au@SiO_2$ Nanospheres

To evaluate the electrostatic nature of internally etched silica-coated gold (IE $Au@SiO_2$) nanoparticles, passive molecular transport of 4-ABT through the silica membrane is studied as a function of KCl concentration. All experiments are conducted in water using 5 nM IE $Au@SiO_2$ nanospheres, 20 µM 4-ABT, and 0 to 100 mM of KCl. Each sample is incubated for 1 hour prior to SERS measurements. Spectral noise, SERS intensity for both primary vibrational modes of 4-ABT (1078 cm^{-1} C-H bending and 1590 cm^{-1} ring stretching) after subtracting the spectral noise, and peak ratio of 1078 cm^{-1}/1590 cm^{-1} are reported in Table B.2A. The spectral noise is calculated by averaging a range in each spectrum where no target molecule signal is observed and is 1700 to 1900 ADU. One should expect the SERS response to increase then saturate with increasing ionic strength, according to Zharov. [175, 304] This is because, the electrolyte ions can decrease the Bjerrum length between two elementary charges within the micropores on the silica membrane and allow the pores to reach their original size (~1.5 - 2 nm) for increase passive molecular diffusion. This result should be observed because once all the available metal surface is occupied by the target molecule the signal should remain the same. For the preliminary data however, SERS signal intensity of 4-ABT increased with no saturation. To observe the complete reported trend, the ionic strength of the solution should be greater than 100 mM to reduce the Bjerrum length to its reported size of 0.7 nm, or the sample incubation time prior to SERS measurement should be greater than 1 hour to make sure of complete equilibrium. As for the peak ratio, no trend is

observed. This could be because at each KCl concentration, different numbers of 4-ABT are transported through the silica membrane toward the core causing changes in molecular orientation for different polarization of each vibrational mode.

To investigate the effect of pH on passive molecular diffusion through silica membrane encapsulated gold nanospheres, the SERS signal intensity of 4-ABT was used to measure changes the response. All studies are completed in pH adjusted water 4.0, 5.5, 7.0 or 8.5 separately using 5 nM IE Au@SiO_2 nanospheres, 20 µM 4-ABT, and 100 mM KCl. At this pH range the surface of the stationary phase IE Au@SiO_2 nanospheres should remain negatively charged because all the different pHs from this study are greater than the silica pKa ~2.[305-307] Each sample is incubated for 1 hour followed by SERS measurements using 60 minutes integration time. Table B.2B shows the spectral noise, SERS intensity after subtracting spectral noise, and peak ratio of 1078 cm^{-1}/1590 cm^{-1}. The SERS response is expected to follow a Gaussian curve distribution if the molecular charges dominate the transport of the target analyte through the silica membrane. One should observe no SERS signal at pH 4.0. This is because 4-ABT will be positively charged as the amine group is protonated at pH less than its pKa, which is 5.[175] Therefore, it should interact with the silica surface instead of being transported through the silica membrane toward the gold core for SERS detection. At a pH equal to 6.0, 4-ABT should be neutral because the number of positively and negatively charged molecules in the solution should be equal. Therefore, SERS signal should be observed because of passive molecular diffusion, and no interaction with the silica surface. At pH 7.0 or above, the SERS signal should decrease to noise because both the mobile phase (4-

Table B.2 Spectral noise, SERS intensities for both vibrational modes of 4-aminobenzenethiol: 1078 cm^{-1} C-H bending and 1587 cm^{-1} ring stretching, and peak ratio (1078/1590).

A

[KCl] (mM)	**0**	**5**	**20**	**50**	**100**
Noise (ADU)	0.420	0.472	0.398	0.415	0.209
1078 cm^{-1} (ADU)	8.502	8.309	8.727	8.517	10.183
1587 cm^{-1} (ADU)	3.387	2.666	2.348	3.760	5.393
Peak Ratio	2.510	3.117	3.717	2.265	1.888

B

pH	**4.0**	**5.5**	**7.0**	**8.5**
Noise (ADU)	0.260	0.242	0.236	0.289
1078 cm^{-1} (ADU)	10.364	14.090	18.044	20.330
1587 cm^{-1} (ADU)	3.892	7.757	12.816	16.483
Peak Ratio	2.663	1.817	1.408	1.233

Table B.2 Continue here

C

Ethanol (%)	**0**	**0.5**	**5.0**	**10.0**
Noise (ADU)	0.019	0.228	0.368	0.002
1078 cm^{-1} (ADU)	11.052	13.359	21.280	30.239
1587 cm^{-1} (ADU)	5.562	8.452	11.970	15.315
Peak Ratio	1.987	1.581	1.778	1.975

Note: 5 nM IE Au@SiO_2 nanoparticles and 20 μM 4-aminobenzenethiol (4-ABT) are incubated for 1 hour with (A) varying KCl concentrations (0 – 100 mM), (B) pH (4.0 -8.5), or (C) polarity (0 – 10 % EtOH) before collected the data reported above. Spectral noise is calculated as mention in Table A.1note.

ABT) and the stationary phase are negatively charged and should repel each other, due to deprotonation of thiol group, as the pH of the solution is above its pKa, which is 6.9.[308] For the preliminary study, however, a different trend is observed. SERS signal intensity of 4-ABT increases as a function of pH, indicating that the solubility of the analyte increased with increasing pH, which dominates (confirm by scifinder) instead of molecular activity.

Next, the effect of polarity is studied on molecular diffusion of 4-ABT through silica membrane stabilizing gold nanospheres using SERS detection. In this experiment, analyte concentration, nanoparticle concentration, ionic strength, and pH of the solvent are kept constant, while the polarity of the solution is varied using ethanol. These values are as follows: 20 µM 4-ABT, 5 nM IE Au@SiO_2 nanospheres, 100 mM KCl, and 8.5 pH (adjusted water), and the aqueous solution polarity is varied by increasing the amount of ethanol from 0% to 10%. Increasing the percent of ethanol should decrease the polarity of the aqueous solution and allow the analyte to be more soluble, as it is non-polar. One should expect the SERS signal intensity of 4-ABT to increase as a function ethanol. Preliminary results shown in Table B.2C support this expectation. Moreover, decreasing the polarity of the solution will not only increase the solubility of the analyte, but also maintain the nanoparticle structure even at pH higher than 8.5 because unlike water silica dissolution will not occur.

B.3 Multi-Analytes Detection Using SERS-Active IE Au@SiO_2 Nanoparticles

After determining the optimal solution conditions, such as ionic strength, pH, and polarity, IE Au@SiO_2 nanospheres could be used for multi-analyte detection. To date two analytes 2-NT and 4-ABT were detected simultaneously using SERS

spectroscopy. The SERS spectra for 10 μM 2-NT (Figure B.3-1), 4-ABT (Figure B.3-2), and the mixture (Figure B.3-3) incubated in 5 nM IE Au@SiO_2 nanoparticles are shown in Figure B.3. Each vibrational mode is labeled and associated to 2-NT (1065 cm^{-1} C-H bending and 1380 ring stretching) and 4-ABT (1078 cm^{-1} C-H bending and 1590 cm^{-1} ring stretching). The bands centered at 1065 and 1078 cm-1 are not resolved but 1380 (2-NT) and 1590 cm-1 (4-ABT) are resolved and are used to identify each analyte from the mixture sample. Although two analytes were able to be detected using IE Au@SiO_2 nanoparticles, if three to five analytes can be detected simultaneously, this will increase solution-phase nanoparticles integration in biological and environment studies. Figure B.4 shows the chemical structures and SERS spectra of four Raman-active analytes that can be used for simultaneous SERS detection, as each possesses a unique vibrational mode that be identified after a multi-analyte study. These analytes, with their unique vibrational modes, are: 4-thiouracal (4-TU) and 914 cm-1, N-H out-of-plane bending (Figure B.4-1), 1,2-bis(4 pyridyl)ethylene (4-BPE) and 1641 cm-1, C=C stretching (Figure B.4-2), 2-naphthalenethiol (2-NT) and 1380 cm-1, ring stretching (Figure B.4-3), and 2-mercaptopyridine (2-MPy) and 1000 cm-1, ring breathing (Figure B.4-4). The Raman shift assignments for all four molecules are reported in Table B.3.

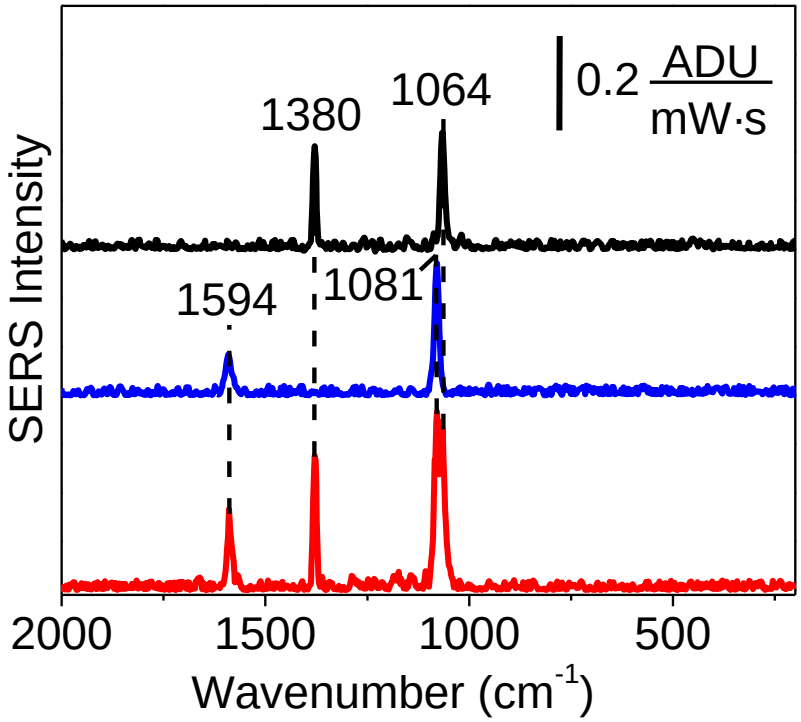

Figure B.3 SERS detection of 10 μM (1) 2-NT, (2) 4-ATP, and (3) 2-NT & 4-ATP incubated in 5 nM IE Au@SiO_2 nanoparticles. The bands centered at 1064 and 1380 cm^{-1} are assigned to 2-NT while 1081 and 1594 cm^{-1} to 4-ATP. SERS collection parameters: power laser = 2 mW, λ_{Ex} = 632.8 nm, and t_{int} = 60 seconds.

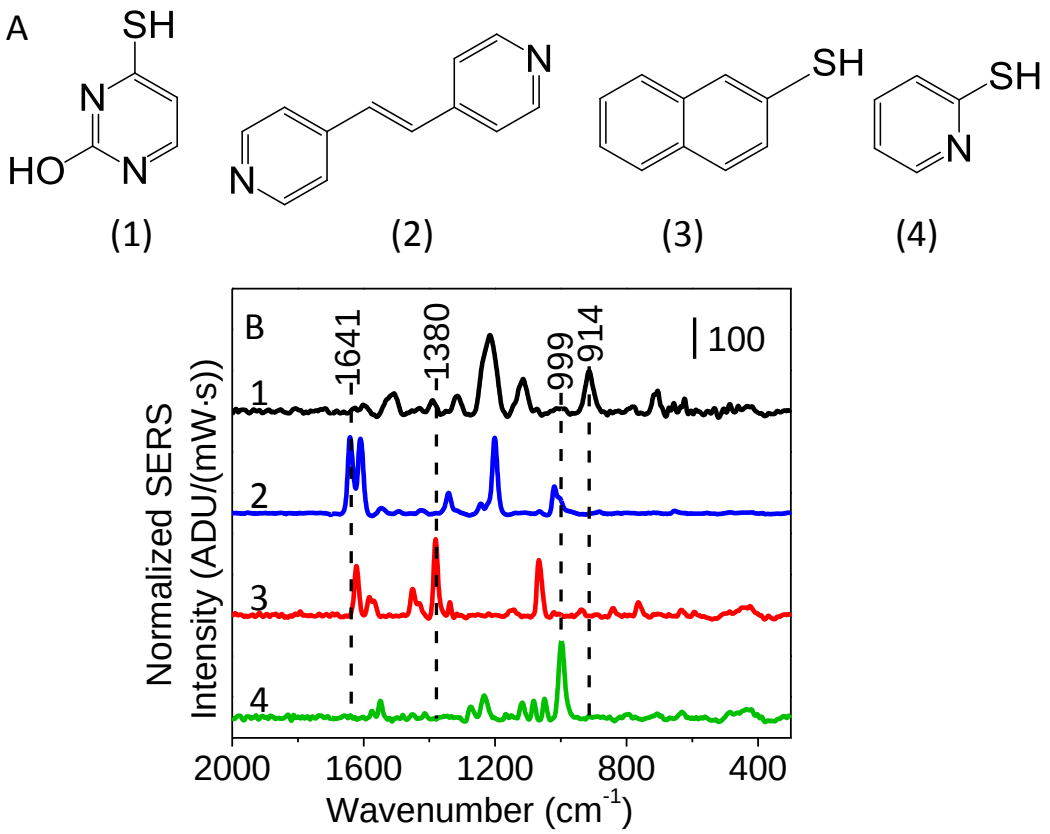

Figure B.4 (A) Molecular structures and (B) SERS spectra of (1) 4-thiourical (4TU), (2) 1,2-bis(4 pyridyl)ethylene (4BPE), (3) 2-naphthalenethiol (2NT), and (4) 2-mercaptopyridine (2MPy). All measurements were collected using 5 nM citrate stabilized gold nanospheres incubated with 10 µM chromophore. Conditions: λ_{ex} = 632.8 nm, t_{int} = 45 s, and P = 2 mW. The unique vibrational modes for 4TU (914 cm^{-1}, N-H out-of-plane bending), 4BPE (1641 cm^{-1}, C=C stretching), 2NT (1380 cm^{-1}, ring stretching), and 2MPy (999 cm^{-1}, ring breathing) are labeled. Each spectrum was normalized to the SERS intensity of the C=C stretching (1641 cm^{-1}) for 4BPE.

Table B.3 Raman shift assignments of 1,2-bis(4 pyridyl)ethylene (4BPE),[309] 2-mercaptopyridine (2MPy),[310] 2-naphthalenethiol (2NT),[311] and 4-thiourical (4TU).[312]

Raman Shift (Δcm^{-1})	Assignments	Molecule
1641 vs	C=C stretch	1,2-bis(4 pyridyl)ethylene
1622 s	Ring stretch	2-naphthalenethiol
1607 vs	C-N bend, C-C stretch	1,2-bis(4 pyridyl)ethylene
1601 w	C-C stretch	4-thiourical
1580 w	Ring stretch	2-naphthalenethiol
1576 vw	C=C stretch	2-mercaptopyridine
1546 vw; w	C-C stretch; C=C stretch	1,2-bis(4 pyridyl)ethylene ; 2-mercaptopyridine
1510 m	C=C & C=N stretch	4-thiourical
1451 m	Ring stretch	2-naphthalenethiol
1390 w	C-H bend	4-thiourical
1380 vs	Ring stretch	2-naphthalenethiol
1340 w	C-H bend, C=C bend	1,2-bis(4 pyridyl)ethylene
1337 vw	Ring stretch	2-naphthalenethiol
1315 w	Ring stretch	4-thiourical
1275 w	C=C & C=N stretch	2-mercaptopyridine
1243 vw	N-H deformation	1,2-bis(4 pyridyl)ethylene
1231 m	C=H bend, N-H ring deformation	2-mercaptopyridine
1216 vs	C-N stretch	4-thiourical

Table B.3 Continue here

1202 vs	C-C stretch, C-N bend	1,2-bis(4 pyridyl)ethylene
1148 vw	C-H bend	2-naphthalenethiol
1117 w; m	C-H wag; Ring breathing, C-S stretch	2-mercaptopyridine; 4-thiourical
1083 w	C-H bend	2-mercaptopyridine
1073 vw	C-N stretch	4-thiourical
1065 s	C-H bend	2-naphthalenethiol
1050 w	C-H bend	2-mercaptopyridine
1019 w	Ring breathing	1,2-bis(4 pyridyl)ethylene
1005 vw	Ring deformation	4-thiourical
999 vs	Ring breathing	2-mercaptopyridine
914 s	N-C stretch	4-thiourical
841 vw	C-H twist	2-naphthalenethiol
782 vw	C-H wag, C=O bend	4-thiourical
764 vw	C-H wag	2-naphthalenethiol
709 w	N-H wag	4-thiourical
660 vw	N-H wag	4-thiourical
633 vw	C-C-C bend; Ring twist	2-mercaptopyridine; 2-naphthalenethiol
625 vw	Ring deformation	4-thiourical

B.4 Conclusions

These preliminary studies demonstrate that knowing the optimal solution conditions during SERS detection is a critical step because increased electrolyte ions will increase the micropores on the silica membrane from their original which should increase molecular diffusion. Whereas, increasing solvent pH and decreasing solution polarity should allow more accurate analyte concentration, the solubility of these molecules should not be affected. Therefore, more accurate conclusions can be made from individual and multi-analytes SERS studies because these will only have to focus on changes associated with molecular size, binding group, and/or orientation.

REFERENCES

1. Kim, K. and H.S. Lee, *Effect of Ag and Au Nanoparticles on the SERS of 4-Aminobenzenethiol Assembled on Powdered Copper.* The Journal of Physical Chemistry B, 2005. **109**(40): p. 18929-18934.

2. Kim, K. and J.K. Yoon, *Raman Scattering of 4-Aminobenzenethiol Sandwiched between Ag/Au Nanoparticle and Macroscopically Smooth Au Substrate.* The Journal of Physical Chemistry B, 2005. **109**(44): p. 20731-20736.

3. Hu, X., et al., *Surface-Enhanced Raman Scattering of 4-Aminothiophenol Self-Assembled Monolayers in Sandwich Structure with Nanoparticle Shape Dependence: Off-Surface Plasmon Resonance Condition.* Journal of Physical Chemistry C, 2007. **111**(19): p. 6962-6969.

4. Roca, M., P.M. Mackie, and A.J. Haes, *Design of a biocompatible and optically-stable solution-phase substrate for SERS detection.* Materials Research Society Symposium Proceedings, 2008. **1133E**(Materials for Optical Sensors in Biomedical Applications): p. 1133/AA09/02-1133/AA09/07.

5. Boo, D.W., et al., *Surface-enhanced raman scattering (SERS) on chemically prepared silver film.* Chemical Physics Letters, 1985. **120**(3): p. 301-306.

6. Zeng, S., et al., *A Review on Functionalized Gold Nanoparticles for Biosensing Applications.* Plasmonics, 2011. **6**(3 DO - 10.1007/s11468-011-9228-1): p. 491-506.

7. Narayan, R., et al., *Nanostructured ceramics in medical devices: Applications and prospects.* JOM-Journal of Metals, 2004. **56**(10 DO - 10.1007/s11837-004-0289-x): p. 38-43.

8. Moriarty, P., *Nanostructured materials.* Reports on Progress in Physics, 2001. **64**(3): p. 297-381.

9. Buzea, C., I. Pacheco, and K. Robbie, *Nanomaterials and nanoparticles: Sources and toxicity.* Biointerphases, 2007. **2**(4 DO - 10.1116/1.2815690): p. MR17-MR71.

10. Klaine, S.J., et al., *Nanomaterials in the environment : Behavior, fate, bioavailability, and effects.* Environmental toxicology and chemistry / SETAC, 2008. **27**(9): p. 1825-1851.

11. Haes, A.J., et al., *Plasmonic materials for surface-enhanced sensing and spectroscopy.* MRS Bulletin, 2005. **30**(5): p. 368-375.

12. Haynes, C.L., et al., *Nanoparticles with tunable localized surface plasmon resonances.* Topics in Fluorescence Spectroscopy, 2005. **8**(Radiative Decay Engineering): p. 47-99.

13. Nehl, C.L., H. Liao, and J.H. Hafner, *Optical Properties of Star-Shaped Gold Nanoparticles.* Nano Letters, 2006. **6**(4): p. 683-688.

14. Doering, W.E., et al., *SERS as a foundation for nanoscale, optically detected biological labels.* Advanced Materials, 2007. **19**(20): p. 3100-3108.

15. Lal, S., et al., *Tailoring plasmonic substrates for surface enhanced spectroscopies.* Chemical Society Reviews, 2008. **37**(5): p. 898-911.

16. Le, F., et al., *Metallic Nanoparticle Arrays: A Common Substrate for Both Surface-Enhanced Raman Scattering and Surface-Enhanced Infrared Absorption.* ACS Nano, 2008. **2**(4): p. 707-718.

17. El-Sayed, M.A., *Some Interesting Properties of Metals Confined in Time and Nanometer Space of Different Shapes.* Accounts of Chemical Research, 2001. **34**(4): p. 257-264.

18. Haynes, C.L. and R.P. Van Duyne, *Nanosphere Lithography: A Versatile Nanofabrication Tool for Studies of Size-Dependent Nanoparticle Optics.* Journal of Physical Chemistry B, 2001. **105**(24): p. 5599-5611.

19. Hulteen, J.C., et al., *Nanosphere Lithography: Size-Tunable Silver Nanoparticle and Surface Cluster Arrays.* Journal of Physical Chemistry B, 1999. **103**(19): p. 3854-3863.

20. Kreibig, U., et al., *Optical investigations of surfaces and interfaces of metal clusters.*, in *Advances in Metal and Semiconductor Clusters*, M.A. Duncan, Editor. 1998, JAI Press Inc.: Stamford. p. 345-393.

21. Kreibig, U., *Optics of nanosized metals*, in *Handbook of Optical Properties*, R.E. Hummel and P. Wissmann, Editors. 1997, CRC Press: Boca Raton. p. 145-190.

22. Link, S. and M.A. El-Sayed, *Spectral Properties and Relaxation Dynamics of Surface Plasmon Electronic Oscillations in Gold and Silver Nano-dots and Nano-rods.* Journal of Physical Chemistry B, 1999. **103**(40): p. 8410-8426.

23. Mulvaney, P., *Not all that's gold does glitter.* MRS Bulletin, 2001. **26**(12): p. 1009-1014.

24. Mulvaney, P., *Surface Plasmon Spectroscopy of Nanosized Metal Particles.* Langmuir, 1996. **12**(3): p. 788-800.

25. Kreibig, U. and M. Vollmer, *Cluster Materials*. Optical Properties of Metal Clusters. Vol. 25. 1995, Heidelberg, Germany: Springer-Verlag. 532.

26. Haes, A.J. and R.P. Van Duyne, *A unified view of propagating and localized surface plasmon resonance biosensors.* Analytical and Bioanalytical Chemistry, 2004. **379**(7-8): p. 920-930.

27. Hutter, E. and J.H. Fendler, *Exploitation of localized surface plasmon resonance.* Advanced Materials, 2004. **16**(19): p. 1685-1706.

28. Ivanov, M.R., H.R. Bednar, and A.J. Haes, *Investigations of the Mechanism of Gold Nanoparticle Stability and Surface Functionalization in Capillary Electrophoresis.* ACS Nano, 2009. **3**(2): p. 386-394.

29. Grass, M., *Colloidally Synthesized Monodisperse Rh Nanoparticles Supported on SBA-15 for Size- and Pretreatment-Dependent Studies of CO Oxidation.* Journal of Physical Chemistry C, 2009. **113**: p. 8616-8623.

30. Nehl, C.L. and J.H. Hafner, *Shape-dependent plasmon resonances of gold nanoparticles.* Journal of Materials Chemistry, 2008. **18**: p. 2415-2419.

31. Srisombat, L.-o., et al., *Preparation, Characterization, and Chemical Stability of Gold Nanoparticles Coated with Mono-, Bis-, and Tris-Chelating Alkanethiols.* Langmuir, 2008. **24**(15): p. 7750-7754.

32. Weisbecker, C.S., M.V. Merritt, and G.M. Whitesides, *Molecular Self-Assembly of Aliphatic Thiols on Gold Colloids.* Langmuir, 1996. **12**(16): p. 3763-3772.

33. Ivanov, M.R. and A.J. Haes, *Nanomaterial Surface Chemistry Design for Advancements in Capillary Electrophoresis Modes.* Analyst, 2011. **136**(1): p. 54-63.

34. Schatz, G.C., M.A. Young, and R.P. Van Duyne, *Electromagnetic mechanism of SERS.* Topics in Applied Physics, 2006. **103**(Surface-Enhanced Raman Scattering): p. 19-46.

35. Campbell, D.J. and Y. Xia, *Plasmons: Why Should We Care?* Journal of Chemical Education, 2007. **84**(1): p. 91-96.

36. Haes, A.J., et al., *Localized Surface Plasmon Resonance Spectroscopy near Molecular Resonances.* Journal of the American Chemical Society, 2006. **128**(33): p. 10905-10914.

37. He, X., et al., *The evidence for synthesis of truncated triangular silver nanoplates in the presence of CTAB.* Journal of Materials Characterization, 2008. **59**(4): p. 380-384.

38. Lu, L., et al., *Fabrication of core-shell Au-Pt nanoparticle film and its potential application as catalysis and SERS substrate.* Journal of materials chemistry, 2004. **14**(6): p. 1005-1009.

39. Sun, L., et al., *Ethanol-Induced Formation of Silver Nanoparticle Aggregates for Highly Active SERS Substrates and Application in DNA Detection.* Journal of Physical Chemistry C, 2008. **112**(5): p. 1415-1422.

40. Dirix, Y., et al., *Oriented Pearl-Necklace Arrays of Metallic Nanoparticles in Polymers: A New Route Toward Polarization-Dependent Color Filters.* Advanced Materials, 1999. **11**: p. 223-227.

41. Maier, S.A., et al., *Local detection of electromagnetic energy transport below the diffraction limit in metal nanoparticle plasmon waveguides.* Nature Materials, 2003. **2**: p. 229-232.

42. Maier, S.A., et al., *Plasmonics-A Route to Nanoscale Optical Devices.* Advanced Materials, 2001. **13**(19): p. 1501-1505.

43. Shelby, R.A., D.R. Smith, and S. Schultz, *Experimental verification of a negative index of refraction.* Science, 2001. **292**(5514): p. 77-78.

44. Andersen, P.C. and K.L. Rowlen, *Brilliant optical properties of nanometric noble metal spheres, rods, and aperture arrays.* Applied Spectroscopy, 2002. **56**(5): p. 124A-135A.

45. Haynes, C.L. and R.P. Van Duyne, *Dichroic Optical Properties of Extended Nanostructures Fabricated Using Angle-Resolved Nanosphere Lithography.* Nano Letters, 2003. **3**(7): p. 939-943.

46. Bauer, G., F. Pittner, and T. Schalkhammer, *Metal nano-cluster biosensors.* Mikrochim. Acta, 1999. **131**(1-2): p. 107-114.

47. Aizpurua, J., et al., *Optical Properties of Gold Nanorings.* Physical Review Letters, 2003. **90**(5): p. 057401/1-057401/4.

48. Bailey, R.C., et al., *Real-time multicolor DNA detection with chemoresponsive diffraction gratings and nanoparticle probes.* Journal of the American Chemical Society, 2003. **125**(44): p. 13541-13547.

49. Elghanian, R., et al., *Selective colorimetric detection of polynucleotides based on the distance-dependent optical properties of gold nanoparticles.* Science, 1997. **227**(5329): p. 1078-1080.

50. Fritzsche, W. and T.A. Taton, *Metal nanoparticles as labels for heterogeneous, chip-based DNA detection.* Nanotechnology, 2003. **14**(12): p. R63-R73.

51. Haes, A.J. and R.P. Van Duyne, *A Nanoscale Optical Biosensor: Sensitivity and Selectivity of an Approach Based on the Localized Surface Plasmon Resonance Spectroscopy of Triangular Silver Nanoparticles.* Journal of the American Chemical Society, 2002. **124**(35): p. 10596 - 10604.

52. Haes, A.J. and R.P. Van Duyne, *Nanosensors Enable Portable Detectors for Environmental and Medical Applications.* Laser Focus World, 2003. **39**: p. 153-156.

53. Hirsch, L.R., et al., *A Whole Blood Immunoassay Using Gold Nanoshells.* Analytical Chemistry, 2003. **75**(10): p. 2377-2381.

54. Kreibig, U., M. Gartz, and A. Hilger, *Mie resonances. Sensors for physical and chemical cluster interface properties.* Berichte der Bunsen-Gesellschaft, 1997. **101**(11): p. 1593-1604.

55. Storhoff, J.J., et al., *One-Pot Colorimetric Differentiation of Polynucleotides with Single Base Imperfections Using Gold Nanoparticle Probes.* Journal of the American Chemical Society, 1998. **120**(9): p. 1959-1964.

56. Freeman, R.G., et al., *Self-Assembled Metal Colloid Monolayers: An Approach to SERS Substrates.* Science, 1995. **267**: p. 1629-1632.

57. Haynes, C.L. and R.P. Van Duyne, *Plasmon-Sampled Surface-Enhanced Raman Excitation Spectroscopy.* Journal of Physical Chemistry B, 2003. **107**: p. 7426-7433.

58. Haynes, C.L., et al., *Nanoparticle Optics: The Importance of Radiative Dipole Coupling in Two-Dimensional Nanoparticle Arrays.* Journal of Physical Chemistry B, 2003. **107**: p. 7337-7342.

59. Jensen, T.R., et al., *Surface-enhanced infrared spectroscopy: a comparison of metal island films with discrete and nondiscrete surface plasmons.* Applied Spectroscopy, 2000. **54**(3): p. 371-377.

60. Kahl, M., et al., *Periodically structured metallic substrates for SERS.* Sensors and Actuators B-Chemical, 1998. **51**(1-3): p. 285-291.

61. Nie, S. and S.R. Emory, *Probing single molecules and single nanoparticles by surface-enhanced Raman scattering.* Science, 1997. **275**(5303): p. 1102-1106.

62. Pipino, A.C.R., R.P. Van Duyne, and G.C. Schatz, *Surface-enhanced second-harmonic diffraction: Experimental investigation of selective enhancement.* Physical Review B: Condensed Matter, 1996. **53**(7): p. 4162-9.

63. Van Duyne, R.P., j.C. Hulteen, and D.A. Treichel, *Atomic force microscopy and surface-enhanced Raman spectroscopy. I. Silver island films and silver film over polymer nanosphere surfaces supported on glass.* Journal of Chemical Physics, 1993. **99**(3): p. 2101-15.

64. Yang, W.-h., et al., *A surface-enhanced hyper-Raman and surface-enhanced Raman scattering study of trans-1,2-bis(4-pyridyl)ethylene adsorbed onto silver film over nanosphere electrodes. Vibrational assignments: experiment and theory.* Journal of Chemical Physics, 1996. **104**(11): p. 4313-4323.

65. Zhao, J., et al., *Interaction of Plasmon and Molecular Resonances for Rhodamine 6G Adsorbed on Silver Nanoparticles.* Journal of the American Chemical Society, 2007. **129**: p. 7647-7656.

66. Schatz, G.C. and R.P. Van Duyne, eds. *Electromagnetic Mechanism of Surface-Enhanced Spectroscopy*. Handbook of Vibrational Spectroscopy, ed. J.M. Chalmers and P.R. Griffiths. Vol. 1. 2002, Wiley: New York. 759-774.

67. Rycenga, M., et al., *Controlling the Synthesis and Assembly of Silver Nanostructures for Plasmonic Applications.* Chemical Reviews, 2011. **111**(6): p. 3669-3712.

68. Daniel, M.-C. and D. Astruc, *Gold Nanoparticles: Assembly, Supramolecular Chemistry, Quantum-Size Related Properties, and Applications toward Biology, Catalysis, and Nanotechnology.* Chemical Reviews, 2004. **104**: p. 293-346.

69. Raman, C.V. and K.S. Krishnan, *Polarisation of Scattered Light-quanta.* Nature, 1928. **122**: p. 169.

70. Zepp, R.G., W.M. Sheldon, and M.A. Moran, *Dissolved Organic Fluorophores in Southeastern US Coastal Waters: Correction Method for*

Eliminating Rayleigh and Raman Scattering Peaks in Excitation-Emission Matrices. Marine Chemistry, 2004. **89**(1-4): p. 15-36.

71. Raman, C.V., *A new radiation.* Indian Journal of Physics, 1928. **2**: p. 387-398.

72. Chance, K.V. and R.J.D. Spurr, *Ring effect studies: Rayleigh scattering, including molecular parameters for rotational Raman scattering, and the Fraunhofer spectrum.* Applied Optics, 1997. **36**(21): p. 5224-5230.

73. Harris, D.C. and M.D. Bertolucci, *Vibratiomal Spectroscopy*, in *Symmetry and Spectroscopy: An Introduction to Vibrational and Electronic Spectroscopy*. 1989, Dover Publications.

74. Tobias, R.S., *Raman spectroscopy in inorganic chemistry. I. Theory.* Journal of Chemical Education, 1967. **44**(1): p. 2.

75. Rusciano, G., et al., *Raman spectroscopy of Xenopus laevis oocytes.* Methods Xenopus Oocytes as an Experimental System, 2010. **51**(1): p. 27-36.

76. Himmel, D., et al., *Raman microspectrometry sulfur detection and characterization in the marine ectosymbiotic nematode Eubostrichus dianae (Desmodoridae, Stilbonematidae).* Biology of the Cell, 2009. **101**(1): p. 43-54.

77. Vankeirsbilck, T., et al., *Applications of Raman spectroscopy in pharmaceutical analysis.* TrAC Trends in Analytical Chemistry, 2002. **21**(12): p. 869-877.

78. Marcelli, A., et al., *Biological applications of synchrotron radiation infrared spectromicroscopy.* Biotechnology Advances, 2012. **30**(6): p. 1390-1404.

79. Carter, E., et al., *Vibrational spectroscopic mapping and imaging of tissues and cells.* Biophysical Reviews, 2009. **1**(2 DO - 10.1007/s12551-009-0012-9): p. 95-103.

80. Frezzotti, M.L., F. Tecce, and A. Casagli, *Raman spectroscopy for fluid inclusion analysis.* Journal of Geochemical Exploration, 2012. **112**(0): p. 1-20.

81. Glatz, Z., S. Nováková, and H. Šterbová, *Analysis of thiocyanate in biological fluids by capillary zone electrophoresis.* Journal of Chromatography A, 2001. **916**(1 - 2): p. 273-277.

82. Pienpinijtham, P., et al., *Highly Sensitive and Selective Determination of Iodide and Thiocyanate Concentrations Using Surface-Enhanced Raman Scattering of Starch-Reduced Gold Nanoparticles.* Analytical Chemistry, 2011. **83**(10): p. 3655-3662.

83. Cui, Y., et al., *Multianalyte immunoassay based on surface-enhanced Raman spectroscopy.* Journal of Raman Spectroscopy, 2007. **38**(7): p. 896-902.

84. Biggs, K.B., et al., *Surface-Enhanced Raman Spectroscopy of Benzenethiol Adsorbed from the Gas Phase onto Silver Film over Nanosphere Surfaces: Determination of the Sticking Probability and Detection Limit Timeâ€* Journal of Physical Chemistry A, 2009. **113**(16): p. 4581-4586.

85. Goldstein, F., *The Colorimetric Determination of Thiocyanate in Whole Blood.* J. Biol. Chem., 1950. **187**: p. 523-527.

86. Prue, D.M., J.E. Martin, and A.S. Hume, *A critical evaluation of thiocyanate as a biochemical index of smoking exposure.* Behavior Therapy, 1980. **11**(3): p. 368-379.

87. Abbaspour, A., et al., *Thiocyanate-selective electrode based on unsymmetrical benzoN4 nickel(II) macrocyclic complexes.* Talanta, 2002. **57**(5): p. 859-867.

88. Torano, J.S. and H.J.M. van Kan, *Simultaneous determination of the tobacco smoke uptake parameters nicotine, cotinine and thiocyanate in urine, saliva and hair, using gas chromatography-mass spectrometry for characterisation of smoking status of recently exposed subjects.* Analyst, 2003. **128**(7): p. 838-843.

89. Kudelski, A., *Characterization of thiolate-based mono- and bilayers by vibrational spectroscopy: A review.* Vibrational Spectroscopy, 2005. **39**(2): p. 200-213.

90. Christesen, S.D., *Raman Cross Sections of Chemical Agents and Simulants.* Applied Spectroscopy, 1988. **42**(2): p. 318-321.

91. Palonpon, A.F., et al., *Raman and SERS microscopy for molecular imaging of live cells.* Nature Protocols, 2013. **8**(4): p. 677-692.

92. Bonora, S., et al., *Raman and SERS study on cimetidine-metal complexes with biomedical interest.* Journal of Raman Spectroscopy, 2011. **42**(4): p. 612-620.

93. Cai, T., et al., *Normal Raman and SERS spectroscopy of the vitamin E.* Journal of Physics: Conference Series, 2011. **277**: p. 012010-1-012010-6.

94. Jeanmaire, D.L. and R.P. Van Duyne, *Surface Raman spectroelectrochemistry. Part I. Heterocyclic, aromatic, and aliphatic amines adsorbed on the anodized silver electrode.* Journal of Electroanalytical Chemistry and Interfacial Electrochemistry, 1977. **84**(1): p. 1-20.

95. Kneipp, K., et al., *Surface-enhanced Raman scattering and biophysics.* Journal of Physics: Condensed Matter, 2002. **14**: p. R597-R624.

96. Moore, B.D., et al., *Rapid and ultra-sensitive determination of enzyme activities using surface-enhanced resonance Raman scattering.* Nature Biotechnology, 2004. **22**: p. 1133-1138.

97. Shin, K.S., et al., *Surface-Enhanced Raman Scattering of Benzenethiol Adsorbed on Silver-Exchanged Copper Powders.* Bulletin of the Korean Chemical Society, 2008. **29**(2): p. 445-449.

98. Fleischmann, M., P.J. Hendra, and A.J. McQuillan, *Raman spectra of pyridine adsorbed at a silver electrode.* Chemical Physics Letters, 1974. **26**(2): p. 163-166.

99. Taton, T.A., G. Lu, and C.A. Mirkin, *Two-Color Labeling of Oligonucleotide Arrays via Size-Selective Scattering of Nanoparticle Probes.* Journal of the American Chemical Society, 2001. **123**(21): p. 5164-5165.

100. Moskovits, M., *Surface-enhanced spectroscopy.* Reviews of Modern Physics, 1985. **57**(3): p. 783-826.

101. Tian, Z.Q., *Surface-enhanced Raman spectroscopy: advancements and applications.* Journal of Raman Spectroscopy, 2005. **36**(6-7): p. 466-470.

102. Otto, A., et al., *Surface-enhanced Raman scattering.* Journal of Physics: Condensed Matter, 1992. **4**(5): p. 1143-1212.

103. Le Ru, E.C., M. Meyer, and P.G. Etchegoin, *Proof of Single-Molecule Sensitivity in Surface Enhanced Raman Scattering (SERS) by Means of a Two-Analyte Technique.* Journal of Physical Chemistry B, 2006. **110**(4): p. 1944-1948.

104. Xu, H., et al., *Spectroscopy of Single Hemoglobin Molecules by Surface Enhanced Raman Scattering.* Physical Review Letters, 1999. **83**(21): p. 4357-4360.

105. Futamata, M., Y. Maruyama, and M. Ishikawa, *Microscopic morphology and SERS activity of Ag colloidal particles.* Vibrational Spectroscopy, 2002. **30**(1): p. 17-23.

106. Dieringer, J.A., et al., *A Frequency Domain Existence Proof of Single-Molecule Surface-Enhanced Raman Spectroscopy.* Journal of the American Chemical Society, 2007. **129**(51): p. 16249-16256.

107. Ghosh, S. and T. Pal, *Interparticle coupling effect on the surface plasmon resonance of gold nanoparticles: From theory to applications.* Chem. Rev., 2007. **107**(11): p. 4797-4862.

108. Vo-Dinh, T., *Surface-enhanced Raman spectroscopy using metallic nanostructures.* TrAC, Trends in Analytical Chemistry, 1998. **17**(8+9): p. 557-582.

109. Volkan, M., D.L. Stokes, and T. Vo-Dinh, *A sol–gel derived AgCl photochromic coating on glass for SERS chemical sensor application.* Sensors and Actuators B: Chemical, 2005. **106**(2): p. 660-667.

110. Li, Y.-S., J. Cheng, and L.B. Coons, *A silver solution for surface-enhanced Raman scattering.* Spectrochimica Acta Part A: Molecular and Biomolecular Spectroscopy, 1999. **55**(6): p. 1197-1207.

111. Zou, S., et al., *New Strategies for Surface-Enhanced Raman Scattering at Transition-Metal Interfaces: Thickness-Dependent Characteristics of Electrodeposited Pt-Group Films on Gold and Carbon.* Journal of Physical Chemistry B, 1999. **103**(21): p. 4218-4222.

112. Cao, Y. and Y.-S. Li, *Constructing Surface Roughness of Silver for Surface-Enhanced Raman Scattering by Self-Assembled Monolayers and Selective Etching Process.* Applied Spectroscopy, 1999. **53**(5): p. 540-546.

113. Bao, F., et al., *Synthesis and Characterization of Au@Co and Au@Ni Core-Shell Nanoparticles and Their Applications in Surface-Enhanced Raman Spectroscopy.* Journal of Physical Chemistry C, 2007. **112**(2): p. 345-350.

114. Kawabata, S., et al., *Fabrication and characterization of a granular film consisting of size-selected silver nanoparticles: application to a SERS substrate.* The European Physical Journal D, 2007. **43**(1-3 DO - 10.1140/epjd/e2007-00064-2): p. 155-158.

115. Xu, H., et al., *Electromagnetic contributions to single-molecule sensitivity in surface-enhanced raman scattering.* Physical Review E, 2000. **62**(3 Pt B): p. 4318-4324.

116. Fang, J.X., et al., *A route to increase the enhancement factor of surface enhanced Raman scattering (SERS) via a high density Ag flower-like pattern.* Applied Physics Letters, 2008. **92**(13): p. 131113.

117. Chaney, S.B., et al., *Aligned silver nanorod arrays produce high sensitivity surface-enhanced Raman spectroscopy substrates.* Applied Physics Letters, 2005. **87**(3): p. 031908-031909.

118. Haynes, C.L. and R.P. Van Duyne, *Plasmon scanned surface-enhanced Raman scattering excitation profiles.* Materials Research Society Symposium Proceedings, 2002. **728**(Functional Nanostructured Materials through Multiscale Assembly and Novel Patterning Techniques): p. 217-222.

119. Campion, A. and P. Kambhampati, *Surface-enhanced Raman scattering.* Chemical Society Reviews, 1998. **27**(4): p. 241-250.

120. Kneipp, K., et al., *Ultrasensitive chemical analysis by Raman spectroscopy.* Chemical Reviews, 1999. **99**(10): p. 2957-2976.

121. Lombardi, J.R. and R.L. Birke, *A Unified View of Surface-Enhanced Raman Scattering.* Accounts of Chemical Research, 2009. **42**(6): p. 734-742.

122. Ji, W., et al., *pH-Dependent SERS by Semiconductor-Controlled Charge-Transfer Contribution.* Journal of Physical Chemistry C, 2012. **116**(46): p. 24829-24836.

123. Tong, L., T. Zhu, and Z. Liu, *Approaching the electromagnetic mechanism of surface-enhanced Raman scattering: from self-assembled arrays to individual gold nanoparticles.* Chemical Society Reviews, 2011. **40**(3): p. 1296-1304.

124. Otto, A., *Surface-Enhanced Raman-Scattering of Adsorbates.* Journal of Raman Spectroscopy, 1991. **22**(12): p. 743-752.

125. Yao, J.L., et al., *A complementary study of surface-enhanced Raman scattering and metal nanorod arrays.* Pure and Applied Chemistry, 2000. **72**(1 - 2): p. 221-228.

126. Jiang, et al., *Single Molecule Raman Spectroscopy at the Junctions of Large Ag Nanocrystals.* Journal of Physical Chemistry B, 2003. **107**(37): p. 9964-9972.

127. Kerker, M., *Founding fathers of light scattering and surface-enhanced Raman scattering.* Applied Optics, 1991. **30**(33): p. 4699-4705.

128. Caldwell, W.B., et al., *Self-Assembled Monolayers of Ferrocenylazobenzenes on Au(111)/Mica Films: Surface-Enhanced Raman Scattering Response vs Surface Morphology.* Langmuir, 1994. **10**(11): p. 4109-15.

129. Dick, L.A., et al., *Metal Film over Nanosphere (MFON) Electrodes for Surface-Enhanced Raman Spectroscopy (SERS): Improvements in Surface Nanostructure Stability and Suppression of Irreversible Loss.* Journal of Physical Chemistry B, 2002. **106**(4): p. 853-860.

130. Harpster, M.H., et al., *SERS detection of indirect viral DNA capture using colloidal gold and methylene blue as a Raman label.* Biosensors and Bioelectronics, 2009. **25**(4): p. 674-681.

131. Wang, D.S. and M. Kerker, *Enhanced Raman scattering by molecules adsorbed at the surface of colloidal spheroids.* Physical Review B, 1981. **24**(4): p. 1777 - 1789.

132. Markel, V.A., et al., *Near-field optical spectroscopy of individual surface-plasmon modes in colloid clusters.* Physical Review B, 1999. **59**(16): p. 10903-10909.

133. McMahon, J., et al., *Gold nanoparticle dimer plasmonics: finite element method calculations of the electromagnetic enhancement to surface-enhanced Raman spectroscopy.* Analytical and Bioanalytical Chemistry, 2009. **394**(7 DO - 10.1007/s00216-009-2738-4): p. 1819-1825.

134. Zeman, E.J. and G.C. Schatz, *An Accurate Electromagnetic Theory Study of Surface Enhancement Factors for Ag, Au, Cu, Li, Na, Al, Ga, In, Zn, and Cd.* Journal of Physical Chemistry, 1987. **91**(3): p. 634-643.

135. Franzen, S., et al., *Optical properties of dye molecules adsorbed on single gold and silver nanoparticles.* Journal of Physical Chemistry A, 2002. **106**(28): p. 6533-6540.

136. Cao, L., et al., *Surface-Enhanced Raman Scattering of p-Aminothiophenol on a Au(core)/Cu(shell) Nanoparticle Assembly.* ChemPhysChem, 2005. **6**(5): p. 913-918.

137. Moskovits, M., D.P. DiLella, and K.J. Maynard, *Surface Raman spectroscopy of a number of cyclic aromatic molecules adsorbed on silver: selection rules and molecular reorientation.* Langmuir, 1988. **4**(1): p. 67-76.

138. Shalaev, V.M. and A.K. Sarychev, *Nonlinear optics of random metal-dielectric films.* Physical Review B, 1998. **57**(20): p. 13265-13288.

139. Kahl, M. and E. Voges, *Analysis of plasmon resonance and surface-enhanced Raman scattering on periodic silver structures.* Physical Review B, 2000. **61**(20): p. 14078-14088.

140. Gersten, J. and A. Nitzan, *Electromagnetic theory of enhanced Raman scattering by molecules adsorbed on rough surfaces.* Journal of Chemical Physics, 1980. **73**(7): p. 3023-37.

141. Schatz, G.C. and R.P. Van Duyne, *Image field theory of enhanced Raman scattering by molecules adsorbed on metal surfaces: detailed comparison with experimental results.* Surface Science, 1980. **101**(1-3): p. 425-38.

142. Bantz, K.C. and C.L. Haynes, *Surface-enhanced Raman scattering detection and discrimination of polychlorinated biphenyls.* Vibrational Spectroscopy, 2009. **50**(1): p. 29-35.

143. Bell, S.E.J. and N.M.S. Sirimuthu, *Surface-Enhanced Raman Spectroscopy as a Probe of Competitive Binding by Anions to Citrate-Reduced Silver Colloids.* Journal of Physical Chemistry A, 2005. **109**(33): p. 7405-7410.

144. Tian, Z.Q., et al., *Extending SERS study to transition metal electrode and nanoparticle surfaces.* Abstracts of Papers of the American Chemical Society, 2003. **225**(1): p. 79.

145. Tian, Z.-Q., et al., *Surface-Enhanced Raman Scattering from Transition Metals with Special Surface Morphology and Nanoparticle Shape.* Faraday Discussions, 2006. **132**: p. 159-170.

146. Tian, Z.-Q., B. Ren, and D.-Y. Wu, *Surface-Enhanced Raman Scattering: From Noble to Transition Metals and from Rough Surfaces to Ordered Nanostructures.* Journal of Physical Chemistry B, 2002. **106**(37): p. 9463-9483.

147. Munro, C.H., et al., *Characterization of the Surface of a Citrate-Reduced Colloid Optimized for Use as a Substrate for Surface-Enhanced Resonance Raman Scattering.* Langmuir, 1995. **11**(10): p. 3712-3720.

148. Zuo, C. and P.W. Jagodzinski, *Surface-Enhanced Raman Scattering of Pyridine Using Different Metals: Differences and Explanation Based on the Selective Formation of Alpha-Pyridyl on Metal Surfaces.* Journal of Physical Chemistry B, 2005. **109**(5): p. 1788-1793.

149. Aroca, R.F., et al., *Surface-enhanced Raman scattering on colloidal nanostructures.* Advances in Colloid and Interface Science, 2005. **116**(1-3): p. 45-61.

150. Brown, R.J.C., et al., *Electromagnetic modelling of Raman enhancement from nanoscale substrates: a route to estimation of the magnitude of the chemical enhancement mechanism in SERS.* Faraday Discussions, 2006. **132**(0): p. 201-213.

151. Brown, R.J.C. and M.J.T. Milton, *Nanostructures and Nanostructured Substrates for Surface-Enhanced Raman Scattering (SERS).* Journal of Raman Spectroscopy, 2008. **39**(10): p. 1313-1326.

152. Murphy, C.J., *Anisotropic Metal Nanoparticles: Synthesis, Assembly, and Optical Applications.* Journal of Physical Chemistry B, 2005. **109**: p. 13857-13870.

153. Xia, Y. and N.J. Halas, *Shape-Controlled Synthesis and Surface Plasmonic Properties of Metallic Nanostructures.* MRS Bulletin, 2005. **30**: p. 338-346.

154. Jensen, L.L. and L. Jensen, *Electrostatic Interaction Model for the Calculation of the Polarizability of Large Noble Metal Nanoclusters.* Journal of Physical Chemistry C, 2008. **112**(40): p. 15697-15703.

155. Tantra, R., R.J.C. Brown, and M.J.T. Milton, *Strategy to improve the reproducibility of colloidal SERS.* Journal of Raman Spectroscopy, 2007. **38**(11): p. 1469-1479.

156. Pierre, M.C.S., et al., *Correlating Molecular Surface Coverage and Solution-Phase Nanoparticle Concentration to Surface-Enhanced Raman Scattering Intensities.* Journal of Physical Chemistry C, 2011. **115**(38): p. 18511-18517.

157. Fabrega, J., et al., *Silver Nanoparticle Impact on Bacterial Growth: Effect of pH, Concentration, and Organic Matter.* Environmental Science & Technology, 2009. **43**(19): p. 7285-7290.

158. Sotiriou, G.A. and S.E. Pratsinis, *Antibacterial Activity of Nanosilver Ions and Particles.* Environmental Science & Technology, 2010. **44**(14): p. 5649-5654.

159. Elechiguerra, J.L., et al., *Interaction of silver nanoparticles with HIV-1.* Journal of Nanobiotechnology, 2005. **3**(6): p. 6-15.

160. Pimpang, P. and S. Choopun, *Monodispersity and Stability of Gold Nanoparticles Stabilized by Using Polyvinyl Alcohol.* Chiang Mai Journal of Science, 2011. **38**(1): p. 31-38.

161. Roca, M. and A.J. Haes, *Silica-Void-Gold Nanoparticles: Temporally Stable Surface-Enhanced Raman Scattering Substrates.* Journal of the American Chemical Society, 2008. **130**(43): p. 14273-14279.

162. Schwartzberg, A.M., et al., *Unique Gold Nanoparticle Aggregates as a Highly Active Surface-Enhanced Raman Scattering Substrate.* Journal of Physical Chemistry B, 2004. **108**(50): p. 19191-19197.

163. Hunter, R.J., *Introduction to Modern Colloid Science*. 1993: Oxford University Press. 344.

164. Kim, M., et al., *Synthesis of Nanorattles Composed of Gold Nanoparticles Encapsulated in Mesoporous Carbon and Polymer Shells.* Nano Letters, 2002. **2**(12): p. 1383-1387.

165. Puniredd, S.R., et al., *Dendrimer-encapsulated Pt nanoparticles in supercritical medium: Synthesis, characterization, and application to device fabrication.* Journal of Colloid and Interface Science, 2009. **332**(2): p. 505-510.

166. Liz-Marzan, L.M. and P. Mulvaney, *The assembly of coated nanocrystal.* Journal of Physical Chemistry B, 2003. **107**(30): p. 7312-7326.

167. Liz-Marzan, L.M., M. Giersig, and P. Mulvaney, *Synthesis of Nanosized Gold-Silica Core-Shell Particles.* Langmuir, 1996. **12**(18): p. 4329-4335.

168. Ohmori, M. and E. Matijevic, *Preparation and properties of uniform coated colloidal particles. VII. Silica on hematite.* Journal of Colloid and Interface Science, 1992. **150**(2): p. 594-598.

169. Philipse, A.P., A.-M. Nechifor, and C. Patmamanoharan, *Isotropic and Birefringent Dispersions of Surface Modified Silica Rods with a Boehmite-Needle Core.* Langmuir, 1994. **10**(12): p. 4451-4458.

170. Zhang, Q., et al., *Permeable Silica Shell through Surface-Protected Etching.* Nano Letters, 2008. **8**(9): p. 2867-2871.

171. Lu, Y., et al., *Modifying the Surface Properties of Superparamagnetic Iron Oxide Nanoparticles through A Sol-Gel Approach.* Nano Letters, 2002. **2**(3): p. 183-186.

172. Oldfield, G., T. Ung, and P. Mulvaney, *Au@SnO2 Core-Shell Nanocapacitors.* Advanced Materials, 2000. **12**(20): p. 1519-1522.

173. Selvan, S.T., et al., *Synthesis of Silica-Coated Semiconductor and Magnetic Quantum Dots and Their Use in the Imaging of Live Cells.* Angewandte Chemie International Edition, 2007. **46**(14): p. 2448-2452.

174. Pierre, M.C.S. and A.J. Haes, *Purification Implications on SERS Activity of Silica Coated Gold Nanospheres.* Analytical Chemistry, 2012. **84**(18): p. 7906-7911.

175. Smith, J.J. and I. Zharov, *Ion Transport in Sulfonated Nanoporous Colloidal Films.* Langmuir, 2008. **24**(6): p. 2650-2654.

176. Mulvaney, S.P., et al., *Glass-coated, analyte-tagged nanoparticles: A new tagging system based on detection with surface-enhanced Raman scattering.* Langmuir, 2003. **19**(11): p. 4784-4790.

177. Doering, W.E. and S. Nie, *Spectroscopic Tags Using Dye-Embedded Nanoparticles and Surface-Enhanced Raman Scattering.* Analytical Chemistry, 2003. **75**(22): p. 6171-6176.

178. Hu, Y., et al., *Control over the permeation of silica nanoshells by surface-protected etching with water.* Physical Chemistry Chemical Physics, 2010. **12**(38): p. 11836-11842.

179. McDonnell, J.M., *Surface plasmon resonance: towards an understanding of the mechanisms of biological molecular recognition.* Curr. Opin. Chem. Biol., 2001. **5**(5): p. 572-577.

180. Lyon, L.A., M.D. Musick, and M.J. Natan, *Colloidal Au-enhanced surface plasmon resonance immunosensing.* Analytical chemistry, 1998. **70**(24): p. 5177-83.

181. Flaugh, P.L., S.E. O'Donnell, and S.A. Asher, *Development of a new optical wavelength rejection filter: demonstration of its utility in Raman spectroscopy.* Applied spectroscopy, 1984. **38**(6): p. 847-50.

182. Spry, R.J. and D.J. Kosan, *Theoretical analysis of the crystalline colloidal array filter.* Applied spectroscopy, 1986. **40**(6): p. 782-4.

183. Merschdorf, M., et al., *Transient electron energy distribution in supported Ag nanoparticles.* New journal of physics, 2002. **4**: p. 1-15, Paper No 95.

184. Liao, C.-Y., et al., *Applications of Cu@C nanoparticles in new dye-sensitized solar cells.* Journal of Nanomaterials, 2009.

185. El-Sayed, I., X. Huang, and M. El-Sayed, *Surface plasmon resonance scattering and absorption of anti-EGFR antibody conjugated gold nanoparticles in cancer diagnostics: Applications in oral cancer.* Nano Letters, 2005. **5**(5): p. 829-834.

186. Huang, X., et al., *Gold nanoparticles: Interesting optical properties and recent applications in cancer diagnostics and therapy.* Nanomedicine, 2007. **2**(5): p. 681-693.

187. Taira, S., et al., *Manganese oxide nanoparticle-assisted laser desorption/ionization mass spectrometry for medical applications.* Science and technology of advanced materials, 2009. **10**(3): p. No pp given.

188. Pustovalov, V.K. and V.A. Babenko, *Optical properties of gold nanoparticles at laser radiation wavelengths for laser applications in nanotechnology and medicine.* Laser physics letters, 2004. **1**(10): p. 516-520.

189. Yan, B., et al., *Engineered SERS Substrates with Multiscale Signal Enhancement: Nanoparticle Cluster Arrays.* ACS Nano, 2009. **3**(5): p. 1190-1202.

190. Michaels, A.M., M. Nirmal, and L.E. Brus, *Surface Enhanced Raman Spectroscopy of Individual Rhodamine 6G Molecules on Large Ag Nanocrystals.* Journal of the American Chemical Society, 1999. **121**(43): p. 9932-9939.

191. Kinnan, M.K. and G. Chumanov, *Surface Enhanced Raman Scattering from Silver Nanoparticle Arrays on Silver Mirror Films: Plasmon-Induced Electronic Coupling as the Enhancement Mechanism.* Journal of Physical Chemistry C, 2007. **111**(49): p. 18010-18017.

192. McFarland, A.D., et al., *Wavelength-Scanned Surface-Enhanced Raman Excitation Spectroscopy.* Journal of Physical Chemistry B, 2005. **109**(22): p. 11279-11285.

193. Liu, Y.C., *Evidence of chemical effect on surface-enhanced Raman scattering of polypyrrole films electrodeposited on roughened gold substrates.* Langmuir, 2002. **18**(1): p. 174-181.

194. Fromm, D.P., et al., *Exploring the chemical enhancement for surface-enhanced Raman scattering with Au bowtie nanoantennas.* Journal of Chemical Physics, 2006. **124**(6): p. 061101.

195. Daniels, J.K. and G. Chumanov, *Nanoparticle-mirror sandwich substrates for surface-enhanced Raman scattering.* Journal of Physical Chemistry B, 2005. **109**(38): p. 17936-17942.

196. Hudson, S.D. and G. Chumanov, *Bioanalytical applications of SERS (surface-enhanced Raman spectroscopy).* Analytical and Bioanalytical Chemistry, 2009. **394**(3): p. 679-686.

197. Porter, M.D., et al., *SERS as a bioassay platform: fundamentals, design, and applications.* Chemical Society Reviews, 2008. **37**(5): p. 1001-1011.

198. Lee, D., et al., *Quantitative analysis of methyl parathion pesticides in a polydimethylsiloxane microfluidic channel using confocal surface-enhanced Raman spectroscopy.* Applied Spectroscopy, 2006. **60**(4): p. 373-377.

199. De Jesus, M.A., K.S. Giesfeldt, and M.J. Sepaniak, *Improving the analytical figures of merit of SERS for the analysis of model environmental pollutants.* Journal of Raman Spectroscopy, 2004. **35**(10): p. 895-904.

200. Zhang, J., et al., *A direct and facile synthetic route for micron-scale gold prisms and fabrication of gold prism thin films on solid substrates.* Materials Chemistry and Physics, 2010. **119**(1-2): p. 188-194.

201. Jin, R., et al., *Controlling anisotropic nanoparticle growth through plasmon excitation.* Nature, 2003. **425**(6957): p. 487-490.

202. Okada, N., et al., *Linear and Nonlinear Optical Response of Silver Nanoprisms: Local Electric Fields of Dipole and Quadrupole Plasmon Resonances.* Journal of Physical Chemistry, 2004. **108**(26): p. 8751-8755.

203. Yoon, J.H., J.S. Park, and S. Yoon, *Time-Dependent and Symmetry-Selective Charge-Transfer Contribution to SERS in Gold Nanoparticle Aggregates.* Langmuir, 2009. **25**(21): p. 12475-12480.

204. Saleh, N., et al., *Ionic strength and composition affect the mobility of surface-modified Fe nanoparticles in water-saturated sand columns.* Environmental Science and Technology, 2008. **42**(9): p. 3349-3355.

205. Jolivet, J.P., et al., *Precipitation of spinel iron oxide: nanoparticle size control.* Materials Research Society Symposium Proceedings, 1997. **432**(Aqueous Chemistry and Geochemistry of Oxides, Oxyhydroxides, and Related Materials): p. 145-150.

206. Stokes, R.J., et al., *Surface-enhanced Raman scattering spectroscopy as a sensitive and selective technique for the detection of folic acid in water and human serum.* Applied Spectroscopy, 2008. **62**(4): p. 371-376.

207. Bell, S.E.J., J.N. Mackle, and N.M.S. Sirimuthu, *Quantitative surface-enhanced Raman spectroscopy of dipicolinic acid - towards rapid anthrax endospore detection.* Analyst, 2005. **130**(4): p. 545-549.

208. Ryu, K., et al., *Use of Peptide for Selective and Sensitive Detection of an Anthrax Biomarker via Peptide Recognition and Surface Enhanced Raman Scattering.* Journal of Raman Spectroscopy, 2010. **41**(2): p. 121-124.

209. Creighton, J.A., C.G. Blatchford, and M.G. Albrecht, *Plasma resonance enhancement of Raman scattering by pyridine adsorbed on silver or gold sol particles of size comparable to the excitation wavelength.* Journal of the Chemical Society, Faraday Transactions 2, 1979. **75**(5): p. 790-8.

210. Chan, J., et al., *Raman spectroscopy and microscopy of individual cells and cellular components.* Laser and Photonics Reviews, 2008. **2**(5): p. 325-349.

211. Bell, S.E.J. and N.M.S. Sirimuthu, *Quantitative surface-enhanced Raman spectroscopy.* Chemical Society Reviews, 2008. **37**(5): p. 1012-1024.

212. Kolega, R.R. and J.B. Schlenoff, *Self-assembled monolayers of an aryl thiol: formation, stability, and exchange of adsorbed 2-naphthalenethiol and bis(2-naphthyl) disulfide on Au.* Langmuir, 1998. **14**(19): p. 5469-5478.

213. Grabar, K.C., et al., *Preparation and Characterization of Au Colloid Monolayers.* Analytical Chemistry, 1995. **67**(4): p. 735-43.

214. Haiss, W., et al., *Determination of Size and Concentration of Gold Nanoparticles from UV-Vis Spectra.* Analytical Chemistry, 2007. **79**(11): p. 4215-4221.

215. McMahon, J.M., et al., *Gold nanoparticle dimer plasmonics: finite element method calculations of the electromagnetic enhancement to surface-enhanced Raman spectroscopy.* Analytical and Bioanalytical Chemistry, 2009. **394**(7): p. 1819-1825.

216. Li, J.F., et al., *Shell-isolated nanoparticle-enhanced Raman spectroscopy.* Nature Letters, 2010. **464**(7287): p. 392-395.

217. Mulvaney, P. and L.M. Liz-Marzan, *Rational material design using Au core-shell nanocrystals*, in *Colloid Chemistry 1*. 2003. p. 225-246.

218. Grzelczak, M., et al., *Shape control in gold nanoparticle synthesis.* Chemical Society Reviews, 2008. **37**(9): p. 1783-1791.

219. Nikoobakht, B. and M.A. El-Sayed, *Surface-Enhanced Raman Scattering Studies on Aggregated Gold Nanorods.* Journal of Physical Chemistry A, 2003. **107**(18): p. 3372-3378.

220. Pande, S., et al., *Synthesis of normal and inverted gold-silver core-shell architectures in beta-cyclodextrin and their applications in SERS.* Journal of Physical Chemistry C, 2007. **111**(29): p. 10806-10813.

221. Sweeney, S.F., G.H. Woehrle, and J.E. Hutchison, *Rapid Purification and Size Separation of Gold Nanoparticles via Diafiltration.* Journal of the American Chemical Society, 2006. **128**(10): p. 3190-3197.

222. Green, A.A. and M.C. Hersam, *Processing and properties of highly enriched double-wall carbon nanotubes.* Nature Nanotechnology, 2009. **4**(1): p. 64-70.

223. Novak, J.P., et al., *Purification of Molecularly Bridged Metal Nanoparticle Arrays by Centrifugation and Size Exclusion Chromatography.* Analytical Chemistry, 2001. **73**(23): p. 5758-5761.

224. Chen, G., et al., *High-Purity Separation of Gold Nanoparticle Dimers and Trimers.* Journal of the American Chemical Society, 2009. **131**(12): p. 4218-4219.

225. Jana, N.R., *Nanorod shape separation using surfactant assisted self-assembly.* Chemical Communications, 2003(15): p. 1950-1951.

226. Liu, F.-K., *Monitoring the synthesis of Au nanoparticles using SEC.* Chromatographia, 2008. **68**(1/2): p. 81-87.

227. Krueger, K.M., et al., *Characterization of nanocrystalline CdSe by size exclusion chromatography.* Analytical Chemistry, 2005. **77**(11): p. 3511-3515.

228. Sharma, V., K. Park, and M. Srinivasarao, *Shape separation of gold nanorods using centrifugation.* Proceedings of the National Academy of Sciences of the United States of America, 2009. **106**(13): p. 4981-4985.

229. Liu, F.-K., *SEC characterization of Au nanoparticles prepared through seed-assisted synthesis.* Chromatographia, 2007. **66**(9/10): p. 791-796.

230. Otto, D.P., H.C.M. Vosloo, and M.M. de Villiers, *Application of Size Exclusion Chromatography in the Development and Characterization of Nanoparticulate Drug Delivery Systems.* Journal of Liquid Chromatography & Related Technologies, 2007. **30**(17): p. 2489-2514.

231. Choi, W.C., T.G. Kim, and J.-S. Kim, *Correlation between photoluminescence and Fourier transform infrared spectra in tetra-ethyl-ortho-silicate thin ?lms.* Nanotechnology, 2006. **17**(4): p. 1150 - 1153.

232. Claridge, S.A., et al., *Isolation of Discrete Nanoparticle-DNA Conjugates for Plasmonic Applications.* Nano Letters, 2008. **8**(4): p. 1202-1206.

233. Tyler, T.P., et al., *Improved Monodispersity of Plasmonic Nanoantennas via Centrifugal Processing.* J. Phys. Chem. Lett., 2011. **2**(3): p. 218-222.

234. Gole, A. and C.J. Murphy, *Biotin-streptavidin-induced aggregation of gold nanorods: Tuning rod-rod orientation.* Langmuir, 2005. **21**(23): p. 10756-10762.

235. Stober, W., A. Fink, and E. Bohn, *Controlled growth of monodisperse silica spheres in the micron size range.* Journal of Colloid and Interface Science, 1968. **26**(1): p. 62-69.

236. Liz-Marzán, L.M., M. Giersig, and P. Mulvaney, *Homogeneous silica coating of vitreophobic colloids.* Chemical communications, 1996(6): p. 731-732.

237. Grzelczak, M., M.A. Correa-Duarte, and L.M. Liz-Marzan, *Carbon nanotubes encapsulated in wormlike hollow silica shells.* Small, 2006. **2**(10): p. 1174-1177.

238. Lal, S., et al., *Profiling the Near Field of a Plasmonic Nanoparticle with Raman-Based Molecular Rulers.* Nano Letters, 2006. **6**(10): p. 2338-2343.

239. Ye, Q., J.X. Fang, and L. Sun, *Surface-enhanced Raman scattering from functionalized self-assembled monolayers 2. Distance dependence of enhanced Raman scattering from an azobenzene terminal group.* Journal of Physical Chemistry B, 1997. **101**(41): p. 8221-8224.

240. Nardou, E., et al., *Distance dependence of the Surface Enhanced Raman Scattering effect observed in amorphous TiO2 on nanostructured gold.* Optical Materials, 2011. **33**(12): p. 1907-1910.

241. Rowe, J.E., et al., *Ultrahigh-Vacuum Studies of Enhanced Raman Scattering from Pyridineon Ag Surfaces.* PHYSICAL REVIEW LETTERS, 1980. **44**(26): p. 1770 - 1773.

242. Kennedy, B.J., et al., *Determination of the Distance Dependence and Experimental Effects for Modified SERS Substrates Based on Self-Assembled Monolayers Formed Using Alkanethiols.* Journal of Physical Chemistry B, 1999. **103**: p. 3640-3646.

243. Sharma, B., et al., *SERS: Materials, applications, and the future.* Materialstoday, 2012. **15**(1 – 2): p. 16-25.

244. Vanderkooy, A., et al., *Silica Shell/Gold Core Nanoparticles: correlating Shell Thichness with the Plasmonic Red Shift upon Aggregation.* ACS Applied Materials and Interfaces, 2011. **3**(10): p. 3942-3947.

245. Walter, E.C., et al., *Metal nanowire arrays by electrodeposition.* Chemphyschem, 2003. **4**(2): p. 131-138.

246. Cobley, C.M., et al., *Shape-Controlled Synthesis of Silver Nanoparticles for Plasmonic and Sensing Applications.* Plasmonics, 2009. **4**(2): p. 171-179.

247. Rouhana, L.L., J.A. Jaber, and J.B. Schlenoff, *Aggregation-Resistant Water-Soluble Gold Nanoparticles.* Langmuir, 2007. **23**(26): p. 12799-12801.

248. Mayya, K.S., V. Patil, and M. Sastry, *On the stability of carboxylic acid derivatized gold colloidal particles: the role of colloidal solution pH studied by optical absorption spectroscopy.* Langmuir, 1997. **13**(15): p. 3944-3947.

249. Kannan, N., K.S. Mukunthan, and S. Balaji, *A comparative study of morphology, reactivity and stability of synthesized silver nanoparticles using Bacillus subtilis and Catharanthus roseus (L.) G. Don.* Colloids and Surfaces B: Biointerfaces, 2011. **86**(2): p. 378-383.

250. Balabin, R.M. and S.V. Smirnov, *Variable selection in near-infrared spectroscopy: Benchmarking of feature selection methods on biodiesel data.* Analytica Chimica Acta, 2011. **692**(1-2): p. 63-72.

251. Ansar, S.M., et al., *Determination of the Binding Affinity, Packing, and Conformation of Thiolate and Thione Ligands on Gold Nanoparticles.* The Journal of Physical Chemistry C, 2011. **115**(3): p. 653-660.

252. Joseph, V., et al., *SERS enhancement of gold nanospheres of defined size.* Journal of Raman Spectroscopy, 2011. **42**(9): p. 1736-1742.

253. Brehm, J.M., et al., *Serum vitamin D levels and severe asthma exacerbations in the Childhood Asthma Management Program study.* Journal of Allergy and Clinical Immunology, 2010. **126**(1): p. 52-58, e52/1-e52/5.

254. Martin, C.R. and D.T. Mitchell, *Template-synthesized nanomaterials in electrochemistry*, in *Electroanalytical Chemistry, Vol 21*. 1999, MARCEL DEKKER: New York. p. 1-74.

255. Haes, A.J., et al., *Using Solution-Phase Nanoparticles, Surface-Confined Nanoparticle Arrays and Single Nanoparticles as Biological Sensing Platforms.* Journal of Fluorescence, 2004. **14**(4): p. 355-367.

256. Sun, Y. and Y. Xia, *Increased Sensitivity of Surface Plasmon Resonance of Gold Nanoshells Compared to That of Gold Solid Colloids in Response to Environmental Changes.* Analytical Chemistry, 2002. **74**(20): p. 5297-5305.

257. Kreibig, U. and L. Genzel, *Optical absorption of small metallic particles.* Surface Science, 1985. **156, Part 2**(0): p. 678-700.

258. Sarkar, D. and N.J. Halas, *General vector basis function solution of Maxwellâ€™s equations.* Physical Review E, 1997. **56**(1): p. 1102-1112.

259. Murphy, C.J. and N.R. Jana, *Controlling the aspect ratio of inorganic nanorods and nanowires.* Advanced Materials, 2002. **14**(1): p. 80-82.

260. Jin, R., et al., *Photoinduced conversion of silver nanospheres to nanoprisms.* Science, 2001. **294**(5548): p. 1901-1903.

261. Oldenburg, S.J., et al., *Nanoengineering of optical resonances.* Chemical Physics Letters, 1998. **288**(2-4): p. 243-247.

262. Novak, J.P. and D.L. Feldheim, *Assembly of Phenylacetylene-Bridged Silver and Gold Nanoparticle Arrays.* Journal of the American Chemical Society, 2000. **122**(16): p. 3979-3980.

263. Brousseau, L.C., III, et al., *Assembly of phenylacetylene-bridged gold nanocluster dimers and trimers.* Advanced Materials, 1999. **11**(6): p. 447-449.

264. Caruso, R.A. and M. Antonietti, *Sol-Gel Nanocoating: An Approach to the Preparation of Structured Materials.* Chemistry of Materials, 2001. **13**(10): p. 3272-3282.

265. Marinakos, S.M., et al., *Gold Particles as Templates for the Synthesis of Hollow Polymer Capsules. Control of Capsule Dimensions and Guest Encapsulation.* Journal of the American Chemical Society, 1999. **121**(37): p. 8518-8522.

266. Malinsky, M.D., et al., *Chain Length Dependence and Sensing Capabilities of the Localized Surface Plasmon Resonance of Silver Nanoparticles Chemically Modified with Alkanethiol Self-Assembled Monolayers.* Journal of the American Chemical Society, 2001. **123**(7): p. 1471-1482.

267. Cocchini, F., F. Bassani, and M. Bourg, *Model calculation of the optical properties of metallic particles in a dielectric medium.* Surface Science, 1985. **156, Part 2**(0): p. 851-858.

268. Mulvaney, P., et al., *Silica encapsulation of quantum dots and metal clusters.* Journal of Materials Chemistry, 2000. **10**(6): p. 1259-1270.

269. Underwood, S. and P. Mulvaney, *Effect of the Solution Refractive Index on the Color of Gold Colloids.* Langmuir, 1994. **10**(10): p. 3427-3430.

270. Huang, T. and X.-H.N. Xu, *Synthesis and characterization of tunable rainbow colored colloidal silver nanoparticles using single-nanoparticle plasmonic microscopy and spectroscopy.* Journal of Materials Chemistry, 2010. **20**(44): p. 9867-9876.

271. Kelly, K.L., et al., *The Optical Properties of Metal Nanoparticles: The Influence of Size, Shape, and Dielectric Environment.* Journal of Physical Chemistry B, 2003. **107**(3): p. 668-677.

272. Mie, G., *Contributions to the Optics of Turbid Media, Especially Colloidal Metal Solutions.* Annalen der Physik, 1908. **25**: p. 377-445.

273. Van Blaaderen, A. and A. Vrij, *Synthesis and characterization of monodisperse colloidal organo-silica spheres.* Journal of Colloid and Interface Science, 1993. **156**(1): p. 1-18.

274. Zhang, T., et al., *Formation of Hollow Silica Colloids through a Spontaneous Dissolution-Regrowth Process.* Angewandte Chemie International Edition, 2008. **47**(31): p. 5806-5811.

275. Liu, B. and H.C. Zeng, *Symmetric and Asymmetric Ostwald Ripening in the Fabrication of Homogeneous Core-Shell Semiconductors.* Small, 2005. **1**(5): p. 566-571.

276. Wu, X.-J. and D. Xu, *Soft Template Synthesis of Yolk/Silica Shell particles.* Advanced Materials, 2010. **22**(13): p. 1516-1520.

277. Zhang, W.-M., et al., *Tin-Nanoparticles Encapsulated in Elastic Hollow Carbon Spheres for High-Performance Anode Material in Lithium-Ion Batteries.* Advanced Materials, 2008. **20**(6): p. 1160-1165.

278. Kamata, K., Y. Lu, and Y. Xia, *Synthesis and Characterization of Monodispersed Core-Shell Spherical Colloids with Movable Cores.* Journal of the American Chemical Society, 2003. **125**(9): p. 2384-2385.

279. Jung, L.S., et al., *Quantitative Interpretation of the Response of Surface Plasmon Resonance Sensors to Adsorbed Films.* Langmuir, 1998. **14**(19): p. 5636-5648.

280. Yunus, W.M.b.M. and A.b.A. Rahman, *Refractive index of solutions at high concentrations.* Applied Optics, 1988. **27**(16): p. 3341-3343.

281. Subedi, D.P., et al., *Study of Temperature and Concentration Dependence of Refractive Index of Liquids Using a Novel Technique.* Kathmandu University Journal of Science, Engineering and Technology, 2006. **2**(1): p. 1-7.

282. Charles, D.F., *Refractive Indices of Sucrose-Water Solutions in the Range from 24 to 53% Sucrose.* Analytical Chemistry, 1965. **37**(3): p. 405-406.

283. Kleinman, S.L., et al., *Structural and optical characterization of single nanoparticles and single molecule SERS.* Proceedings of SPIE-the international society for optical engineering, 2010. **7757**: p. 77570J-1-77570J-10.

284. Chen, H., et al., *Shape-Dependent Refractive Index Sensitivities of Gold Nanocrystals with the Same Plasmon Resonance Wavelength.* Journal of Physical Chemistry C, 2009. **113**(41): p. 17691-17697.

285. Chen, H., et al., *Shape- and Size-Dependent Refractive Index Sensitivity of Gold Nanoparticles.* Langmuir, 2008. **24**(10): p. 5233-5237.

286. Hicks, E.M., et al., *Plasmonic Properties of Film over Nanowell Surfaces Fabricated by Nanosphere Lithography.* Journal of Physical Chemistry B, 2005. **109**(47): p. 22351-22358.

287. Tang, J.-L. and J.-N. Wang, *Chemical Sensing Sensitivity of Long-Period Grating Sensor Enhanced by Colloidal Gold Nanoparticles.* Sensors, 2008. **8**(1): p. 171-184.

288. Haes, A.J., et al., *Nanoscale Optical Biosensor: Short Range Distance Dependence of the Localized Surface Plasmon Resonance of Noble Metal Nanoparticles.* Journal of Physical Chemistry B, 2004. **108**(22): p. 6961-6968.

289. Yunus, W.M. and A.B. Rahman, *Refractive index of solutions at high concentrations.* Applied Optics, 1988. **27**(16): p. 3341-3343.

290. Macon, R.A., *USDA Technical Procedures Manual*, in *Brix Table (Sucrose Conversion Table).* 2011. p. 32 - 56.

291. Chichester, C.O., E.E.M. Mark, and G.F. Stewart, *Advances In Food Research*. Moisture Content, ed. A.J.P. White. Vol. 24. 1978, New York: Academic Press, Inc. 298.

292. Harris, W.J., *Method for Size-Distribution Determinations of Non-Volatile Droplets by Electron Microscopy.* British Journal of Applied Physics, 1959. **10**(3): p. 139-140.

293. Malitson, H., *Interspecimen Comparison of the Refractive Index of Fused Silica.* Journal of the Optical Society of American, 1965. **55**(10): p. 1205-1208.

294. Song, M.K., et al., *Influence of Deposition Method on Refractive Index of SiO2 and TiO2 Thin Films for Anti-reflective Multilayers.* Journal of the Korean Ceramic Society, 2008. **45**(9): p. 524-530.

295. Liu, S., Z. Zhang, and M.Y. Han, *Nanometer-Sized Gold-Loaded Gelatin/Silica Nanocapsules.* Advanced Materials, 2005. **17**(15): p. 1862-1866.

296. Tanaka, A. and B. Nakamura, *Optical Imaging: Technology, Methods and Applications*. Imaging, Spectroscopy and Sensing with Single and Coupled Metallic Nanoparticles, ed. T. Sannomiya, J. Junesch, and P. Rajendran. 2012: Nova Science Publishers. 133 - 151.

297. Sannomiya, T., et al., *Biosensing by Densely Packed and Optically Coupled Plasmonic Particle Arrays.* Small, 2009. **5**(16): p. 1889-1896.

298. Okamoto, T., I. Yamaguchi, and T. Kobayashi, *Local plasmon sensor with gold colloid monolayers deposited upon glass substrates.* Optical Letters, 2000. **25**(6): p. 372-374.

299. Haynes, W.M., *CRC Handbook of Chemistry and Physics*. 94th ed, ed. W.M. Haynes and N.I.o.S.a. Technology. 2013, Boulder, Colorado: CRC press. 2668.

300. Haes, A.J. and R.P. Van Duyne, *Nanoscale optical biosensors based on localized surface plasmon resonance spectroscopy.* Proceedings of SPIE-The International Society for Optical Engineering, 2003. **5221**: p. 47-58.

301. Riboh, J.C., et al., *A Nanoscale Optical Biosensor: Real-Time Immunoassay in Physiological Buffer Enabled by Improved Nanoparticle Adhesion.* Journal of Physical Chemistry B, 2003. **107**: p. 1772-1780.

302. Tiwari, N., et al., *Study of adsorption behavior of aminothiophenols on gold nanorods using surface-enhanced Raman spectroscopy.* Journal of Nanophotonics, 2011. **5**(1): p. 053513.

303. Ung, T., L.M. Liz-Marzan, and P. Mulvaney, *Controlled Method for Silica Coating of Silver Colloids. Influence of Coating on the Rate of Chemical Reactions.* Langmuir, 1998. **14**: p. 3740-3748.

304. Newton, M.R., et al., *pH- and Ionic Strength-Controlled Cation Permselectivity in Amine-Modified Nanoporous Opal Films.* Langmuir, 2006. **22**(9): p. 4429-4432.

305. Córdova, E., J. Gao, and G.M. Whitesides, *Noncovalent Polycationic Coatings for Capillaries in Capillary Electrophoresis of Proteins.* Analytical Chemistry, 1997. **69**(7): p. 1370-1379.

306. Parks, G.A., *The Isoelectric Points of Solid Oxides, Solid Hydroxides, and Aqueous Hydroxo Complex Systems.* Chemical Reviews, 1965. **65**(2): p. 177-198.

307. Shyue, J.-J., et al., *Acid-Base Properties and Zeta Potentials of Self-Assembled Monolayers Obtained via in Situ Transformations.* Langmuir, 2004. **20**(20): p. 8693-8698.

308. Raulin, F.o. and J.-P. Lussiana, *Prebiotic formation of iminothioesters. II: Addition of thiophenols to malonic nitriles.* Origins of life, 1984. **14**(1-4 DO - 10.1007/BF00933653): p. 157-162 LA - English.

309. Zhuanga, Z., et al., *Surface-enhanced Raman scattering of trans-1,2-bis (4-pyridyl)-ethylene on silver by theory calculations.* Spectrochimica Acta Part A: Molecular and Biomolecular Spectroscopy, 2011. **79**: p. 1593-1599.

310. Baldwin, J.A., et al., *Surface-Enhanced Raman Scattering of Mercaptopyridines and Pyrazinamide Incorporated in Silver Colloid-Adsorbate Films.* Langmuir, 1997. **13**(14): p. 3744-3751.

311. Alvarez-Puebla, R.A., D.S. Dos Santos Jr, and R.F. Aroca, *Surface-enhanced Raman scattering for ultrasensitive chemical analysis of 1 and 2-naphthalenethiols.* Analyst, 2004. **129**: p. 1251-1256.

312. Burova, T.G., G.N. Ten, and A.A. Anashkin, *Quantum-Mechanical Calculation of the Intensity Distribution in Resonance Raman Spectra of Thiosubstituted Derivatives of Uracil.* Optics and Spectroscopy, 2005. **99**(5): p. 690-694.